Title

Multi-spatial-scale observational studies of the Sierra Nevada snowpack using wireless-sensor networks and multi-platform remote-sensing data

Author

Zheng, Zeshi

Publication Date

2018

Peer reviewed|Thesis/dissertation

Multi-spatial-scale observational studies of the Sierra Nevada snowpack using wireless-sensor networks and multi-platform remote-sensing data

by

Zeshi Zheng

A dissertation submitted in partial satisfaction of the

requirements for the degree of

Doctor of Philosophy

in

Engineering - Civil and Environmental Engineering

in the

Graduate Division

of the

University of California, Berkeley

Committee in charge:

Professor Roger C. Bales, Co-chair
Professor Steven D. Glaser, Co-chair
Professor Alexandre M. Bayen
Professor David R. Brillinger

Summer 2018

Multi-spatial-scale observational studies of the Sierra Nevada snowpack using wireless-sensor networks and multi-platform remote-sensing data

Abstract

Multi-spatial-scale observational studies of the Sierra Nevada snowpack using wireless-sensor networks and multi-platform remote-sensing data

by

Zeshi Zheng

Doctor of Philosophy in Engineering - Civil and Environmental Engineering

University of California, Berkeley

Professor Roger C. Bales, Co-chair

Professor Steven D. Glaser, Co-chair

The Sierra Nevada winter snowpack is the major water resource for the state of California. To better quantify the input of the water system, we deployed wireless-sensor networks across several basins in the Sierra Nevada. Together with operational and scientific research agencies, we also collected numerous scans of snow-on and snow-off lidar data over several basins in the high Sierra. We mined the lidar data and found how spatial patterns of snow depth are affected by topography and vegetation while elevation is the primary variable, other lidar-derived attributes slope, aspect, northness, canopy penetration fraction explained much of the remaining variance. By segmenting the vegetation into individual trees using lidar point clouds, we were able to extract tree wells from the high resolution snow-depth maps and we found the spatial snow distribution to be affected by the interactions of terrain and canopies. The snowpack is deeper at the downslope direction from the tree bole, however the snowpack at upslope direction being deeper. On sub-meter to meter scales, non-parametric machine-learning models, such as the extra-gradient boosting and the random-forest model, were found to be effective in predicting snow depth in both open and under-canopy areas. At spatial scales that are larger than 100×100 m^2, we developed a novel approach of using the k-NN algorithm to combine the real-time wireless-sensor-network data with historical spatial products to estimate snow water equivalent spatially. The results suggest only a few historical snow-water-equivalent maps are needed if the historical maps can accurately represent the spatial distribution of snow water equivalent. The residual from the k-NN estimates can be distributed spatially using a Gaussian-process regression model. The entire estimation process can explain 90% of the variability of the spatial SWE.

To Baoxin and Ping

Contents

List of Figures

List of Tables

Acknowledgments

Firstly, I would like to express my sincere gratitude to my advisor Prof. Roger Bales for the continuous support of my Ph.D study and research. His patient guidance helped me well design my research, understand the topic, implement the research work, and write this thesis. He instructed me both in words and examples with his great passion in science, research, and teaching.

I would also like to thank my co-advisor Prof. Steven Glaser for his support of my study in the civil systems program, and his advising and guidance on the my research in systems engineering. The advice from Prof. Bales and Prof. Glaser are complementary for finishing this thesis, which also allows me experience researching in both science and engineering, and learn problem-solving from different perspectives.

Besides my advisors, my sincere gratitude to Prof. Alexandre Bayen for having me being the graduate student instructor in his optimization course, allowing me to experience teaching rather than just research through out my Ph.D study.

Also great thanks to Prof. David Brillinger, Prof. Scott Moura, and Prof. Alexey Pozdnukhov for your suggestions on my research during my preliminary and qualifying exams.

My sincere gratitude to my lab mates: Francesco Avanzi for all the lessons about hydrology that I learned from him; Qin Ma for her tips in remote-sensing technologies; Sami Malek for his advice in coding; Tessa Maurer for her advice in writing; Carlos Oroza for our great collaborations on papers; Joseph Rungee for our deep discussions about our research; and Ziran Zhang for his advice in graduate study, research, and the fun we had in life.

Also great thanks to my collaborators: Martha Conklin, Noah Molotch, Peter Kirchner, and Yanjun Su for their hard work and great contributions to my publications.

Last but not the least, my family. They are always my strongest supports behind me when I was working on my Ph.D during the past five years. I really want to thank my parents for being supportive and respecting all the decisions I have made. I could not have the current achievement without their cultivation. Also, I would like thank my wife Bingyao. She is the one staying by my side so I don't feel alone when working hard on the Ph.D.

Chapter 1

Introduction

1.1 Background and Motivation

In the western United States, mountain snowpack is the primary source of late spring and early summer streamflow generation and associated agricultural and municipal water supplies (Bales et al., 2006). Knowledge of spring snowpack conditions within a watershed is essential if water availability and flood peaks following the onset of melt are to be predicted (Hopkinson et al., 2001). Both topographical and vegetation factors are extremely important in influencing snowpack conditions, as they interact with meteorological conditions to affect the distribution of precipitation and snow accumulation in the mountains. However, the distribution of mountain precipitation is poorly understood at multiple spatial scales because it is governed by processes that are neither well measured nor accurately predicted (Kirchner et al., 2014).

Snow accumulation across the mountains is primarily influenced by orographic processes, involving feedbacks between atmospheric circulation, terrain and the geomorphic processes of mountain uplift, erosion and glaciation on the earths surface (Roe, 2005). In forested regions snow accumulation is highly sensitive to vegetation structure (Musselman et al., 2008), as canopy snow interception, sublimation and unloading results in smaller accumulations of snow beneath the forest canopies in comparison with open areas (Mahat and Tarboton, 2013). During spring and summer, snow melt is primarily driven by the surface energy balance. Process models that are used for estimating snowmelt and the corresponding runoff have used numerous land-surface attributes. Process models can be calibrated using historical records, but the calibrated models are mostly specific to the studied area and can be erroneous when extreme conditions occur (Essery and Etchevers, 2004).

The Sierra Nevada, as a barrier to inland from the Pacific, provides an ideal mountainous region for producing orographic precipitation and exerts a strong influence on the upslope amplification of precipitation. Subalpine forest and alpine zone cover most of the high elevation area. The geographic, topographic, and vegetation conditions make the Sierra Nevada a natural laboratory in western United States for studying mountain snow distri-

bution, snow accumulation, and snow melt processes. In addition, the Sierra Nevada also serves as natural water storage infrastructure for California. To have a timely estimate of the spatial snow and water storage, it is crucial to have an information system serving real-time information that is both spatially and temporally continuous. This can be done using observations from sensor networks and remote-sensing platforms, with the computation resources for estimating the snowpack storage and streamflow in near real-time.

1.1.1 Snow observation systems

In order to have better knowledge of precipitation, snow accumulation and snow melt in the Sierra Nevada, manual snow surveys, synoptic surveys, and remote-sensing products are used and analyzed. Current decision making for water management in California during the snowmelt season relies on ground measurements, i.e. continuous snow-pillow and snow-depth sensor measurements, and monthly manual snow surveys (Molotch and Bales, 2005). Manual snow surveys are conducted monthly by surveyors from cooperating agencies and current synoptic weather systems employ snow-sensor observations from snow-telemetry (SNOTEL) networks (Rosenberg et al., 2011). Both manual snow surveys and snow-sensor installations are labor intensive and costly in remote areas, which makes measurements sparsely spread in the mountains. As the number of measurements is really limited in catchment scale studies, the measurements could be less representative in such heterogeneous terrain, and the topographic variability of snow accumulation cannot be fully captured. Satellite-based remote-sensing technology, such as MODIS and Landsat, have been used to map snow coverage in basin to global areas, in which each grid has a value from 0 to 1, representing the fraction of area covered by snow (Painter et al., 2009; Rosenthal and Dozier, 1996). But they do not capture snow cover under canopy or snow-depth information. They also have low spatial resolution for catchment-scale studies, or for evaluating heterogeneous canopy effects on snow accumulation and melt.

In recent years, airborne lidar, which overcomes the difficulties described above at catchment to basin scales, has been more frequently employed for doing high spatial resolution distance measurements (Hopkinson et al., 2001), and has become an important technique to acquire topographic data at sub-meter resolution and accuracy (Marks and Bates, 2000). Therefore, lidar provides a solution to understanding snow precipitation distribution in mountainous regions. With multiple returns collection from single laser beam, lidar has also been used to construct vegetation structures as well as observe conditions under the canopy, which helps produce fine resolution DEMs, vegetation structures, and snow-depth information both in open and vegetated areas. Building on high-resolution mapping of snowpack, lidar has also started to be used to supplement water- resource information for near-real-time decision making (Painter et al., 2016).

Complementing high-resolution remote-sensing techniques, measurements on the ground have also been evolved in the past years. Wireless-sensor networks, as a sub domain of the Internet of Things, has enabled high-frequency, spatially distributed, and multivariate measurements. Wireless-sensor networks have been applied in mountain hydrology, and experi-

mental networks have been installed in the Feather River (Malek et al., 2017), the American River (Zhang et al., 2017b), and the Kings River basins. By using historical data, we have developed algorithms for selecting representative sensor locations across basins at various spatial scales (Oroza et al., 2016). With a warming climate around the globe, the data from the spatially distributed wireless-sensor networks installed in the American River basin offer the potential to estimate rain versus snow transition across elevation gradients (Zhang et al., 2017a).

1.1.2 Snow modeling

Other than direct snow-depth and snow-water-equivalent measurements, researchers have developed process models that estimate snow water equivalent either *in situ* or at various spatial resolutions. The essential information for estimating snow water equivalent are the surface energy balance and the mass balance of water. Two different approaches are commonly used by researchers for estimation. One is the degree-day approach, in which the snowmelt is estimated for each modeling time interval by multiplying the total temperature degrees that are above 0°C by pre-calibrated melt factors and the fractional snow covered area (Ohmura, 2001; He et al., 2014). The other approach is the full energy-balance and mass-balance model, which takes all energy and mass inputs, such as long-wave and short-wave radiations, latent heat flux, sensible heat flux, and precipitation (Marks et al., 1992, 1999).

By using the surface-energy-balance approach, snow-coverage information and modeled spatial land-surface meteorological data, several methods have been developed, which back-integrate SWE from the snow melt-out date to the date of maximum SWE at the beginning of the snowmelt season. This technique has been applied across several mountain ranges and is referred to as the SWE-reconstruction technique (Bair et al., 2016; Guan et al., 2013; Margulis et al., 2016; Rittger, 2012). Although SWE reconstruction captures both temporal variability and spatial variability, it can only be done at the end of the season when the daily energy inputs and snow covered area are known (Cline et al., 1998). Although it is difficult to enable real-time estimation of SWE using the reconstruction and reanalysis techniques, these datasets provide us valuable spatio-temporal information on mountain SWE.

In terms of near real-time estimation, a data-assimilation snow-data product that is commonly used in the Continental United States is the Snow Data Assimilation System (SNODAS), which integrates snow information from both satellite and ground stations, providing daily snow depth and snow water equivalent information at 1-km^2 resolution (Barrett, 2003). However, recent work validating the SNODAS spatial product with lidar suggested that the performance of SNODAS in the Tuolumne River basin is less accurate than 3-D $(x, y, \text{elevation})$ bilinear interpolation of ground stations (Bair et al., 2016).

Other than the process-model-based estimation, statistical approaches are also commonly used for spatially interpolating the snow-water-equivalent observations. Binary regression trees have been used by researchers for scaling point snow-depth measurements to 1-km resolution grid (Molotch and Bales, 2005). Kriging approaches have been applied for

blending the reconstructed SWE maps with ground measurements for bias-correcting the SWE reconstructions (Guan et al., 2013). In addition, linear-regression models are more commonly used for estimating the snow water equivalent based on the ground observations and topographic information (Schneider and Molotch, 2016; Fassnacht et al., 2003).

1.2 Research Objectives

With advances in measurement technologies, remote sensing, and the evolving concept of big data, especially with the emerging machine-learning and state-estimation techniques, we are able to fill in knowledge gaps in understanding how the spatial distribution of snowpack is related to terrain and canopy attributes. We are also able to improve the current methods in mountain snowpack measurements, modeling, and near-real-time spatial estimation so that the current water resources management and decision making can have a more timely response to extreme events under a warming climate and increasing water demands.

In detail, we answer several scientific questions through this dissertation, focusing on the spatial distributions of snow water equivalent in the mountainous areas. More specifically we explore topographic and canopy effects on spatial snow distribution and temporal evolution of the snowpack during accumulation and melt. In addition, another objective is to develop a practical method that can accurately estimate the snow water equivalent spatially, in near real-time, at moderate resolution (100 m to 1 km) over basin scales, by blending wireless-sensor-network observations and remote-sensing data.

1.3 Dissertation Overview

For the following chapters in this dissertation, we used multi-platform data sources, including high-resolution lidar data, snow-covered-area images, SWE reconstructions, and wireless-sensor-network data.

In Chapter 2, we examine how lidar can be used to explore the spatial distribution of snow depth, especially in finding informative covariates for modeling the spatial distribution statistically. We analyzed the ground point density distribution of lidar in open areas versus under canopy, which assisted in exploring the spatial distribution of snow depth in forested mountainous areas. Other than using elevation as the single variable for predicting snow depth, we found how snow depth distribute under terrain conditions with different slopes and aspects, and also under various canopy-cover conditions. The content in this chapter was also published in the journal The Cryosphere (Zheng et al., 2016).

In Chapter 3, we strengthened our understanding of snow-depth distribution at fine resolution (sub-meter) in forested areas. By using point-cloud and gridded data-processing techniques, we came up with canopy metrics at a pixel scale, as well as for each individual tree extracted using a canopy-segmentation algorithm. The canopy metrics are found to be informative in exploiting the spatial variability of the snow depth. We also applied machine-

learning techniques to model the spatial snow depth at 0.5-m resolution using the topography and vegetation attributes. We used the trained model together with the simulated canopy-height models for studying the forest thinning effect on snow accumulation prior to the peak season.

In Chapter 4, we extended the analysis using the canopy metrics from Chapter 2 and Chapter 3. Rather than analyzing the snow depth versus covariates spatially, we used multi-year snow-depth data from three sites in the central and southern Sierra. We developed an algorithm that can accurately locate the snow accumulation events. The cumulative snow accumulation at the three sites and the lidar-derived canopy metrics were used such that canopy effects on snow accumulation can be quantified.

Other than quantifying the spatial distribution of the snowpack at sub-meter scales, lidar data were also found being useful for spatial SWE estimation at basin to global scales. In Chapter 5, we described a novel approach that uses a k-nearest-neighbor search to efficiently integrate the spatially distributed snow measurements from the wireless-sensor networks and historical spatial SWE products, such as SWE reconstructions, reanalysis, or lidar, for estimating spatial SWE in near real time. We used lidar-derived SWE products as a ground-truth data set to evaluate the developed method. The new approach can explain approximately 85% of the spatial variability of the snow distribution. The content in this chapter was also published in the journal Remote Sensing of Environment (Zheng et al., 2018).

Chapter 2

Topographic and vegetation effects on snow accumulation in the southern Sierra Nevada: a statistical summary from lidar data

2.1 Introduction

With new advances in remote sensing technologies, finer resolution and more accurate observations on peak season snow cover and snow depth have been enabled. These new information can provide us better knowledge of spatial distribution for snow depth or even snow water equivalent. Under-canopy snowpack is shallower than that in the open area in general. But the differences can be affected by the topography.

In situ, operational measurements of snow water equivalent (SWE) in the Sierra Nevada come from monthly manual snow surveys and daily snow-pillow observations (Rosenberg et al., 2011). Meteorological stations and remote-sensing products also provide estimates of precipitation and snow accumulation (Guan et al., 2013). Cost, data coverage, accuracy (Julander et al., 1998) and basin-scale representativeness are issues for in situ monitoring of SWE in mountainous terrain (Rice and Bales, 2010). Satellite-based remote sensing, such as MODIS, has been used to map snow coverage in large or even global areas. However, it only provides snow-coverage information in open areas, and no direct information on snow depths (Molotch and Margulis, 2008). The SNOw Data Assimilation System (SNODAS) integrates data from satellite and in situ measurements with weatherforecast and physically based snow models, providing gridded SWE and snow-depth estimates (Barrett, 2003). However, since SNODAS has not been broadly assessed (Clow et al., 2012), its potential for evaluating snow distribution in mountain areas remains uncertain. Also, owing to its 1 km spatial resolution, the snow depth that SNODAS provides is a mixed representation of both open and canopy-covered areas.

An orographic-lift effect is observable in most of the above data (Howat and Tulaczyk, 2005; Rice et al., 2011), and a binary-regression-tree model using topographic variables as predictors has also been used for estimating the snow depth in unmeasured areas (Erickson et al., 2005; Erxleben et al., 2002; Molotch et al., 2005). However, regression coefficients could not be estimated accurately for most of the explanatory variables, except for elevation, and the consistency of the orographic trend as well as the relative importance of these variables is still unknown owing to the lack of representative measurements across different slopes, aspects and canopy conditions. Also, the stability of the variance explained by the model needs to be tested with denser measurements.

In recent years, airborne lidar has been used for high-spatial-resolution distance measurements (Hopkinson et al., 2001), and has become an important technique to acquire topographic data with sub-meter resolution and accuracy (Marks and Bates, 2000). Therefore, lidar provides a potential tool to help understand spatially distributed snow depth across mountain regions. With multiple returns from a single laser pulse, lidar has also been used to construct vegetation structures as well as observe conditions under the canopy, which helps produce fine-resolution digital elevation models (DEMs), vegetation structures, and snow-depth information. However, the snow depth under canopy can not always be measured because of the signal-intensity attenuation caused by canopy interception (Deems et al., 2013, 2006). A recent report applied a univariate-regression model to the snow depth measured in open areas using lidar; with a high-resolution DEM used to accurately quantify the orographic-lift effect on the snow accumulation just prior to melt (Kirchner et al., 2014). From this analysis it could be expected that lidar data might also help explain additional sources of snow distribution variability in complex, forested terrain.

The objective of the work reported here is to improve our understanding of how topographic and vegetation attributes affect snow accumulation in mixed-conifer forests. Using lidar data from four headwater areas in the southern Sierra Nevada, we addressed the following three questions. First, in forested mountain terrain what percentage of pixels have ground returns and thus provide snow-depth measurements at 1m and coarser sampling resolutions, and what potential error is introduced by undersampling of snow under dense canopies? Second, what new information about orographic effects on precipitation versus accumulation is provided by these lidar data? Third, what is the effect of slope, aspect and canopy penetration fraction on snow accumulation, relative to elevation, and are effects consistent across sites?

2.2 Methods

Basic lidar data manipulation and processing are involved in this work and a novel attribute, penetration fraction has been developed from lidar point cloud to represent forest density. Statistical analysis has been conducted for quantifying orographic and vegetation effects on snow accumulations.

2.2.1 Study Areas

Our study areas are located in the southern Sierra Nevada, approximately 80 km east of Fresno, California (Figure 2.1). The four headwater-catchment research areas, Bull Creek, Shorthair Creek, Providence Creek, and Wolverton Basin were previously instrumented, including meteorological measurements, in order to have a better knowledge of the hydrologic processes in this region (Bales et al., 2011; Hunsaker et al., 2012; Kirchner et al., 2014). The sites were chosen as part of multi-disciplinary investigations at the Southern Sierra Critical Zone Observatory, and are also the main instrumented sites in the observatory. Wolverton is approximately 64 km southeast of the other three sites (Figure 2.1) and is located in Sequoia National Park. Both snow-on and snow-off airborne lidar were flown in 2010 (Table 2.1) over these sites. The elevation of the survey areas is from 1600-m to 3500-m elevation. Vegetation density generally decreases in high-elevation subalpine forest, with Wolverton also having a large area above treeline (Goulden et al., 2012). The precipitation has historically been mostly snow in the cold and wet winters for elevations above 2000 m, and a rain-snow mix below 2000 m, where most of Providence is located. The comparison between Providence and the other sites can help in assessing if observed trends are consistent above and below the rain-snow transition.

Table 2.1: Lidar data collection information

	Bull	Shorthair	Providence	Wolverton
Snow-off flight date	Aug. 15, 2010	Aug. 13, 2010	Aug 5., 2010	Aug. 13-15, 2010
Snow-on flight date	Mar. 24, 2010	Mar. 23, 2010	Mar. 23, 2010	Mar. 21-22, 2010
Area, km^2	22.3	6.8	18.4	58.9
Mean elevation, m	2264	2651	1850	2840
Elevation range, m	1925-2490	2436-2754	1373-2207	1786-3532
Canopy cover, %	51	43	62	30

2.2.2 Data Collection

All airborne lidar surveys were performed by the National Center for Airborne Laser Mapping (NCALM) using Optech GEMINI Airborne Laser Terrain Mapper. The scan angle and scan frequency were adjusted to ensure a uniform along-track and across-track point spacing (Table 2.2), with six GPS ground stations used for determining aircraft trajectory. The snow-on survey date was close to April 1st, which is used by operational agencies as the date of peak snow accumulation for the Sierra. Since the snow-on survey required four days to cover the four study areas, time-series *in situ* snow-depth data measured continuously from Judd Communications ultrasonic depth sensors at Providence, Bull and Wolverton were used to estimate changes in snow depth during the survey period. While no snow accumulation was observed, snowpack densification and melting observed from the time-series data were

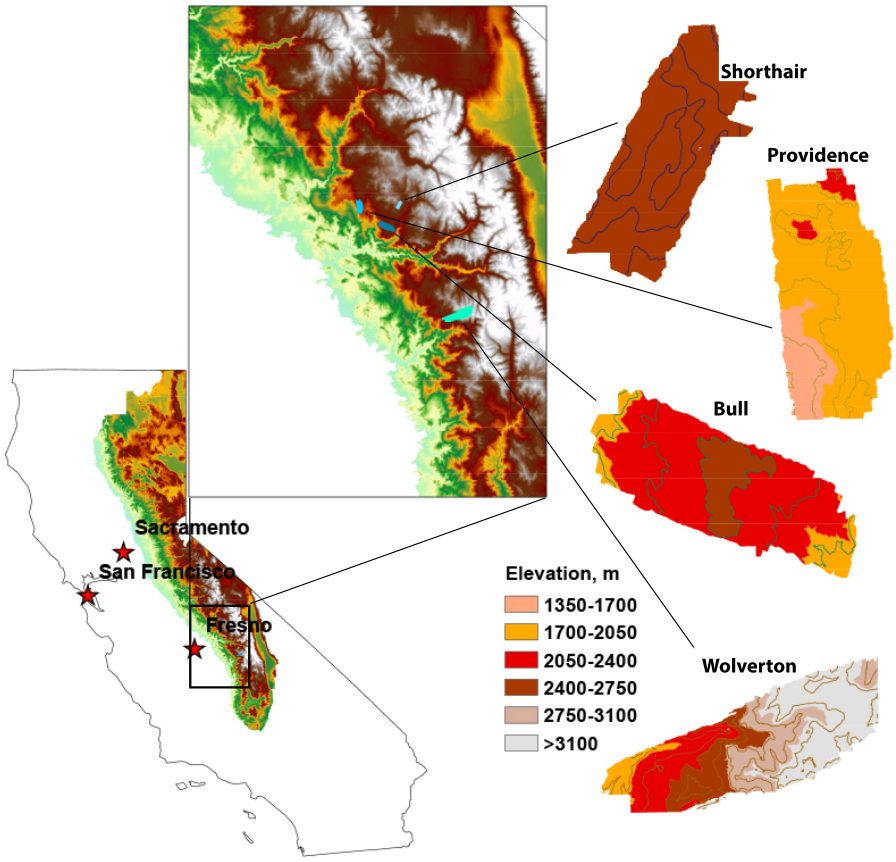

Figure 2.1: Study area and lidar footprints. (Left) California with Sierra Nevada. (Center) Zoomed view to show the locations of lidar footprints. (Right) Elevation and 200-m contour map (100-m for Bull) of lidar footprints

taken into considerations (Hunsaker et al., 2012; Kirchner et al., 2014). The snow-off survey was performed in August after snow had completely melted out in the study areas.

2.2.3 Data Processing

Raw lidar datasets were pre-processed by NCALM and are available from the NSF OpenTopography website (http://opentopography.org) in LAS format. The LAS point cloud, including both canopy and ground-surface points, are stored and classified as ground return and vegetation return. The 1-m resolution digital-elevation models, generated from the lidar point-cloud datasets, were downloaded from the OpenTopography database and further processed in ArcMap 10.2 to generate 1-m resolution slope, aspect, and northness raster products. Northness is an index for the potential amount of solar radiation reaching a slope

Table 2.2: Flight parameters and sensor settings

Flight parameters		Equipment settings	
Flight altitude	600 m	Wavelength	1047nm
Flight speed	65 m s^{-1}	Beam divergence	0.25 mrad
Swath width	233.26 m	Laser PRF	100 kHz
Swath overlap	50%	Scan Frequency	55 Hz
Point density	10.27 m^{-2}	Scan angle	±14°
Cross-track resolution	0.233 m	Scan cutoff	3°
Down-track resolution	0.418 m	Scan offset	0°

on a scale of -1 to 1, calculated from:

$$N = \sin(S) \times \cos(A) \tag{2.1}$$

where N is the northness value; S is the slope angle and A is the aspect angle, both in degrees. For aspect angle A, north is either 0° or 360°. Northness is also the same as the aspect intensity (Kirchner et al., 2014) with 0° focal aspect. Since in this analysis the snow-depth comparison is only discussed between north and south facing slopes, northness is used instead of aspect intensity for simplification. To construct the 1-m resolution canopy-height models from lidar data, the 1-m digital-elevation models were subtracted from the 1-m digital-surface models that were rasterized from the first return of the laser pulses (Figure 2.2).

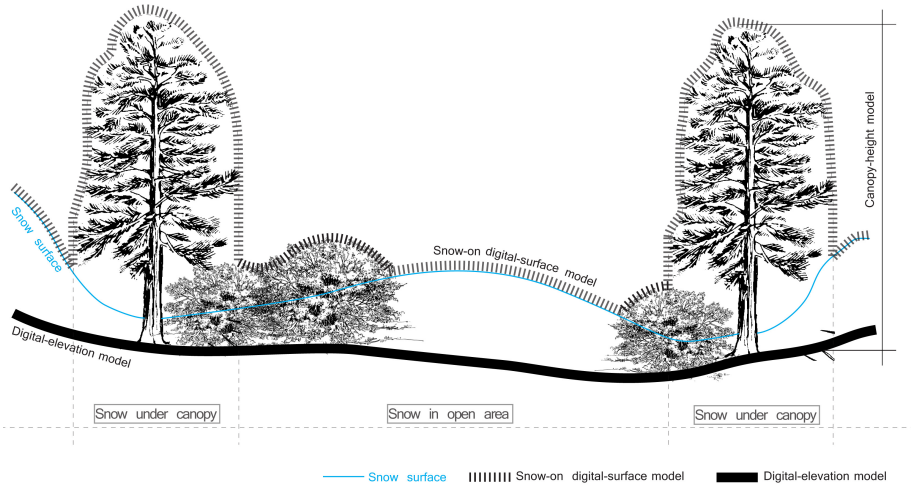

Figure 2.2: Subtracting the digital-elevation model from the digital-surface model will result in the canopy-height model. In this study the height of shrub vegetation is assumed smaller than 2 m while tree vegetation is taller than 2 m.

The snow depths were calculated directly from the snow-on lidar data. By referring to canopy-height models, all ground points in snow-on lidar datasets were classified as under canopy or in open areas. That is, if the ground point was coincident with canopy of ¿2-m height, it was classified as under canopy, and otherwise in the open, i.e., a 2-m height was used to classify shrubs versus trees. In this study we assumed that shrubs did not affect the snow depth. After classification, snow depths were calculated by subtracting the values in the digital-elevation model from the snow-on point-measurement values. The calculated point snow-depth data were further assigned into 1-m raster pixels, averaged within each pixel, formatted and then gap filled by interpolation with pixel values around it. Since not all laser pulses that generated canopy-surface returns had ground returns (Figure 2.3) and the ground-return percentage varied across the transition from the tree trunk to the edge of the canopy, interpolation was not applied to data under the canopy. The error rate of the calculated snow depth should be mainly from the instrumental elevation error, which is about 0.10 m (Kirchner et al., 2014; Nolan et al., 2015).

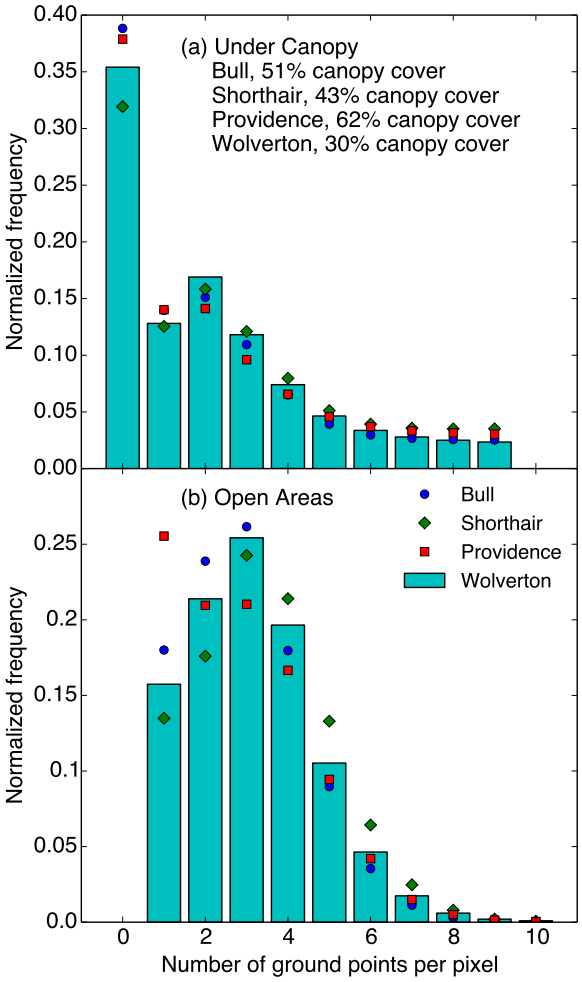

Figure 2.3: Normalized histogram of the number of ground points for (a) under-canopy and (b) open 1-m pixels.

2.2.4 Penetration Fraction

The open-canopy fraction is a factor that represents the forest density above a given pixel and is used to describe the influence of vegetation on snow accumulation and melt. However there is no algorithm to directly extract this information from lidar data. Here we use a novel approach that we call penetration fraction to approximate the open-canopy fraction from the lidar point cloud. With it we were able to quantify the impact of canopy on snow depth using linear regression. Penetration fraction is the ratio of the number of ground points to number of total points within each pixel (Figure 2.4a). Whereas pixels are generally classified as under canopy or in the open (Kirchner et al., 2014), penetration fraction is an index of fraction open in a pixel. Because the electromagnetic radiation from both lidar and sunlight beams are intercepted by canopies, the open-canopy fraction is used here

as an index to represent the fraction of sunlight radiance received on the ground under vegetation. Therefore, penetration fraction of lidar is actually another form of estimating the open-canopy fraction (Musselman et al., 2013). However, under-canopy vegetation can also intercept the lidar beam, causing a bias. To eliminate this bias, the canopy-height model was used to check if the pixel was canopy covered by using the 2-m threshold value; and if not, the local penetration fraction of the pixel was reset to 1 because the open-canopy fraction of a pixel could not be entirely represented by the penetration fraction. A spatial moving-average process was applied using a 2-D Gaussian filter to account for the effect of the vegetation around each pixel. Since the radius of the Gaussian filter needs to be specified by the user, we tested the sensitivity of smoothing results to the radius of the filter and found it is not sensitive when the radius is greater than 1.5 m (Figure 2.4b). Therefore, we specified a radius of 5 m in the Gaussian filter.

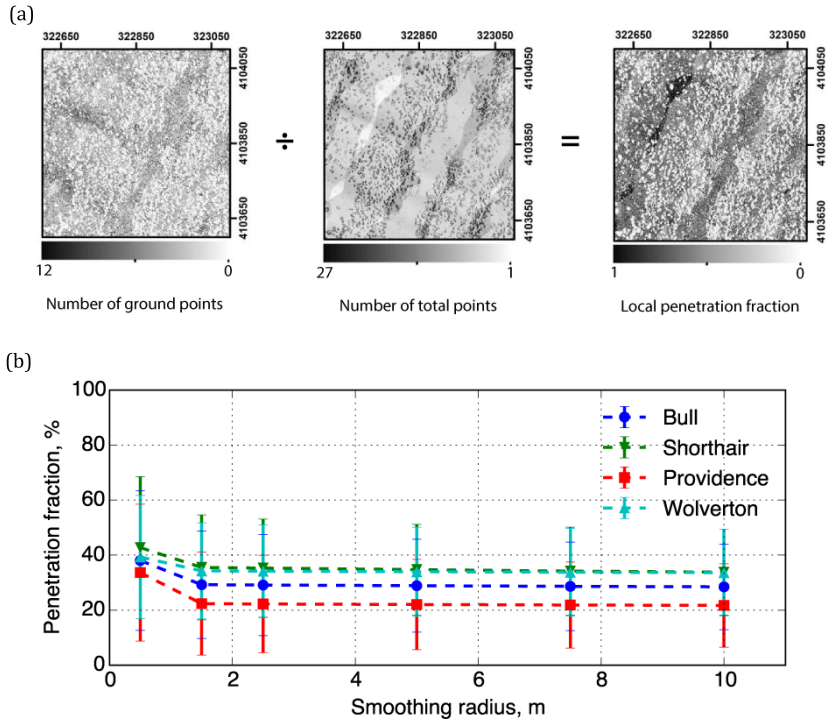

Figure 2.4: (a) Dividing the number of ground points of each 1-m pixel by the total number of points in the pixel gives the penetration fraction of the local pixel. (b) Sensitivity of the smoothed penetration fraction to the smoothing radius.

2.2.5 Statistical Analysis

The 1-m resolution snow-depth raster datasets were resampled into 2-m, 3-m, 4-m and 5-m resolution. The percentage of pixels with snow-depth measurements was calculated by

using the number of pixels with at least one ground return divided by the total number of pixels inside each site. The sensitivity of the percentage changes across different resampling resolutions and the consistency of the percentages across study sites at the same resampling resolution were analyzed by visualizing the percentages against sampling resolutions at all sites.

Using elevation, slope, aspect, penetration fraction and snow depth retrieved from lidar measurements, topographic and vegetation effects on snow accumulation were observed using residual analysis. Owing to orographic effects, there is increasing precipitation along an increasing elevation gradient in this area (Kirchner et al., 2014). Therefore, elevation was selected as the primary variable to fit the linear-regression model for calculating the residual of snow depth. All snow-depth measurements from lidar were first separated by either under canopy or in open areas, and then were binned by elevation of the location where they were measured, with a bin size of 1-m elevation. As each elevation band had hundreds of snow-depth measurements after binning, the average of all snow depths was chosen as the representative snow depth, and the standard deviation calculated to represent the snow-depth variability within each elevation band. Coefficients of determination between snow depth and elevation of each site were calculated by linear regression. The fitted linear-regression model of each site was applied to the DEM to estimate the snow depth. The residual of snow depth was calculated by subtracting the modeled snow depth from lidar-measured snow depth. The slope, aspect and penetration fraction were binned into 1° slope, 1° aspect, and 1% penetration-fraction bins with snow-depth residuals corresponding to each bin of every physiographic variable averaged and visualized along the variable gradient to check the existence of these physiographic effects.

For the variables found to correlate with the snow accumulation, the relative importance of each variable was calculated using the Random Forest algorithm (Breiman, 2001; Pedregosa et al., 2011). A multivariate linear-regression model was also applied to quantify the influence of the various physiographic variables on the snowpack distribution.

To calculate the snow-depth difference between open and canopy-covered areas along an elevation gradient, the 1-m resolution snow-depth data of the two conditions, open and canopy covered, were smoothed separately against elevation using locally weighted scatterplot smoothing (LOESS) (Cleveland, 1979). The snow-depth difference was then calculated by subtracting the smoothed canopy-covered snow depth from that in the open.

2.3 Results

The percentage of pixels having snow-depth measurements is sensitive to the sampling resolution used in processing the lidar point cloud to produce the raster data. Values go from about 65-90% across the 4 sites for 1-m resolution and gradually increase to 99% at 5-m resolution (Figure 2.5). Note that the percentage increases in going from the lower- to higher-elevation sites, reflecting lower forest density at higher elevation.

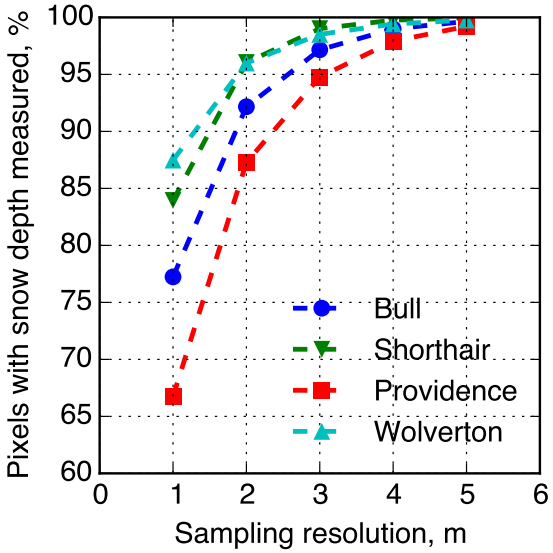

Figure 2.5: Sensitivity of the percent of pixels with snow depth measured to the sampling resolution used in processing the lidar point cloud at each site.

The snow depths in open areas and under canopy show consistent increases with elevation across all sites (Figure 2.6(a), (b)). Although orographic effects may vary between individual storms across sites, these data suggest that the cumulative effect of the 4 main snowfall events prior to the lidar flight (Kirchner, 2013) resulted in similar patterns. The variability within an elevation band for open areas (Figure 2.6(c)) is highest at about 1500 m, and gradually decreases within the rain-snow transition up to 2000-m elevation. However, above 2000 m the pattern of variability with increasing elevation varies across sites. Note that values at the upper or lower ends of elevation at each site have few pixels and thus may not have a representative distribution of other physiographic attributes (Figure 2.6(d)). The forested area of all four sites combined spans the rain-snow transition zone in lower mixed-conifer forest through snow-dominated subalpine forest, with significant areas above treeline higher up.

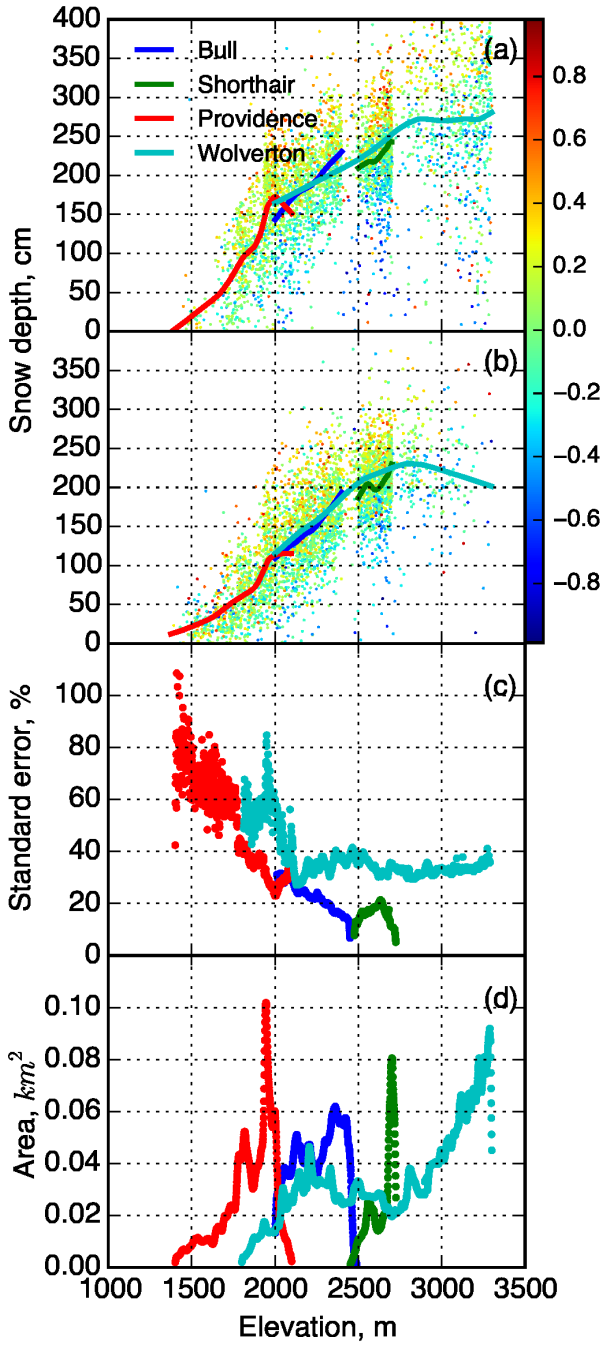

Figure 2.6: LOESS smoothed snow depth with northness color coded scatterplot of raw-pixel snow depth against elevation for (a) open and (b) under-canopy areas. (c) Standard error of the snow depth within each 1-m elevation band for open area. (d) Total area of each elevation band for both open and under-canopy areas. Values above 3300 m not shown, where there are few data.

For each individual site, a least-squares linear regression of averaged snow depth versus elevation was used to investigate the spatial variability of snow depth (Table 2.3). The median elevation of the three sites increases from Providence to Bull to Shorthair. The lowest elevation at Providence Creek is less than 1400 m, and snow depth increases steeply in this region at a rate of 38 cm per 100 m in open areas and 28 cm per 100 m under the canopy. Bull Creek has an elevation range of 2000-2400 meters, which is slightly higher than Providence, and has snow depth increasing at 21 cm per 100 m in open areas and 19 cm per 100 m under the canopy. For Shorthair Creek site, which is the highest of the three, the snow depth increases at 17 cm per 100 m in open areas and 16 cm per 100 m under the canopy. Wolverton is 64 km further south and spans a wider elevation range, going from the rain-snow transition in mixed conifer, to subalpine forest, to some area above treeline. The average snow-depth increase is smallest among all four study sites, 15 cm per 100 m in open areas and 13 cm per 100 m under the canopy. Unlike the other three lower-elevation sites, the snow depth at Wolverton decreases above 3300-m elevation and these high-elevation data were not included in the linear regression. The amount of area above this elevation is relatively small, and factors such as wind redistribution and the exhaustion of perceptible water can also affect snow depth at these elevations (Kirchner et al., 2014).

Table 2.3: Linear-regression results, averaged snow depth vs. elevation in four sites

	Bull	Shorthair	Providence	Wolverton
R^2, open	0.968	0.797	0.931	0.914
R^2, vegetated	0.978	0.737	0.921	0.972
Slope, open, cm per 100 m	21.6	16.1	37.8	15.3
Slope, vegetated, cm per 100 m	19.9	13.1	26.0	13.4

The residuals for snow in open areas were further analyzed for effects of slope, aspect and penetration fraction. The snow-depth residuals are negative and larger in magnitude on steeper slopes, i.e. less snow on steeper slopes (Figure 2.7(a)). The residual also changes from positive to negative with aspect, reflecting deeper snow on north-facing versus south-facing slopes (Figure 2.7(b)). The topographic effect can also be seen from the color pattern of northness observed in the scatterplots (Figure 2.6(a), (b)). The residual also changes from negative 20-40 cm to positive 20-40 cm as penetration fraction increases from 0% to 80%, reflecting less snow under canopy (Figure 2.7(c)). Considering all of these variables together, elevation is the most important variable at all sites except for Shorthair, which has a relatively small elevation range (Figure 2.8). Aspect exerts a stronger influence than do slope and penetration fraction in open areas. However, for under-canopy areas, penetration is more dominant than aspect at two sites. The multivariate regression model was fitted to the data with aspect transformed into 0° to 180° range (north to south). Fitted models can be represented as the following two equations for open area and under canopy respectively:

$$SD = 0.0011 \times E - 0.0112 \times S - 0.0057 \times A + 0.1802 \times P \tag{2.2}$$

$$SD = 0.0011 \times E - 0.0112 \times S - 0.0057 \times A + 0.1802 \times P \quad (2.3)$$

where SD is snow depth, E is elevation, S is slope, A is aspect, and P is penetration fraction. p-values of all regression coefficients of the two models are all smaller than 0.01. The effects quantified in these two equations are mixtures of influences that affected both precipitation and post-deposition processes.

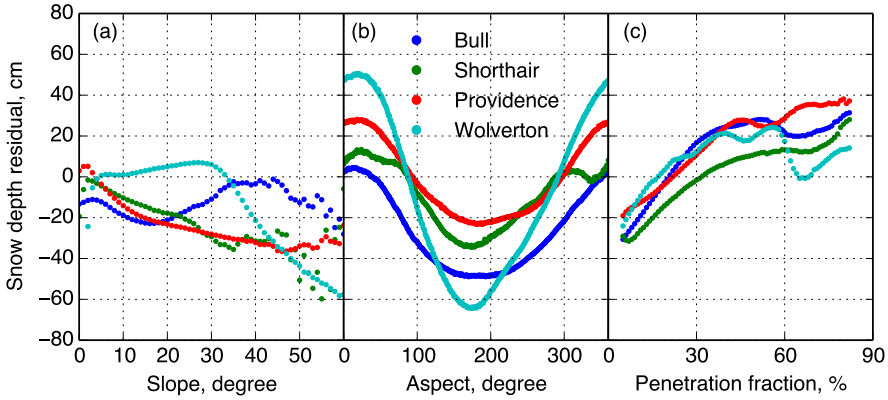

Figure 2.7: Average snow-depth residual, calculated as difference between lidar-measured snow depth and snow depth from the linear-regression models (open areas) versus: (a) slope, aspect, and (c) penetration fraction.

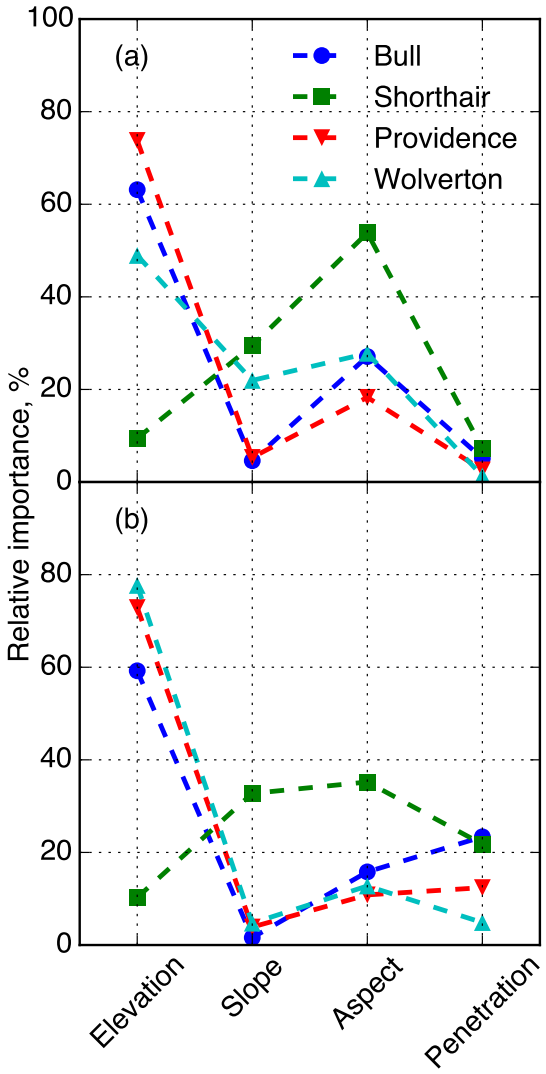

Figure 2.8: Relative importance of each physiographic variable in predicting the snow depth from each site for (a) open area (b) under-canopy area

The snow-depth difference between open and canopy-covered areas was calculated with elevation from locally smoothed snow depth. It generally increases from near zero at 1500 m, where there is little snow but dense canopy, to 40 cm in the range of 1800-2000 m, and varies from near zero to 60 cm at higher elevations where snow is deeper and the canopy less dense (Figure 2.9). It is apparent that the snow-depth difference increases with elevation in the rain-snow transition zone, but lacks a clean pattern along either elevation gradient or penetration-fraction gradient when the elevation is higher.

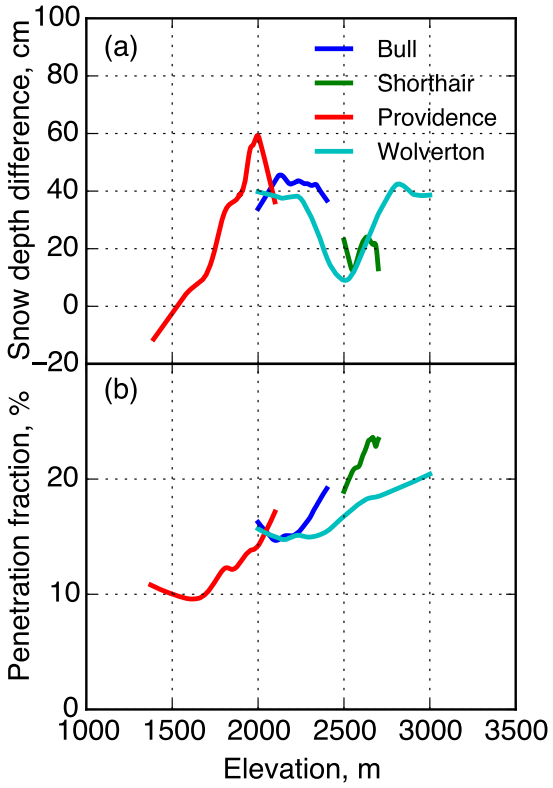

Figure 2.9: (a) Snow-depth difference along elevation for each site calculated from the LOESS smoothed snow depth. (b) Average penetration fraction versus elevation for each site.

2.4 Discussion

2.4.1 Sensitivity of measurements to sampling resolution

The results of analyzing the percentage of pixels with snow depth measured by lidar at different sampling resolutions illustrate that even high-density airborne lidar measurements do not have 100% coverage of the surveyed area at 1-m resolution, especially in densely forested areas. According to the snow-depth difference between snowpack in open areas and under canopy, a trade-off between accuracy and coverage happens when adjusting the resolution; and lower sampling resolutions can introduce overestimation into the results. This is because upon averaging, sub-pixel area under the canopy that was not measured may be represented by the open area that is measured, introducing an overestimation error into the averaged snow depth of the pixel. In order to estimate that bias for each pixel, we would need more under-canopy snow-depth measurements at 1-m resolution. In our survey areas, 28% of the total area in the main snow-producing elevations of 2000-3000 m has no returns at

1-m resolution. Assuming that using open rather than under-canopy values would introduce a bias of at least 35 cm for these unmeasured areas, a 2-m mean snow depth will have about 10 cm or 5% overestimation over the whole area. The overestimation could be higher if the area with no returns represents denser canopy with less snow than the under-canopy areas measured; and could also be more significant for shallower snowpacks. It would also be higher for a less-dense point cloud, which would introduce uncertainty into both percentage canopy cover and open versus under-canopy snow-depth differences. Therefore, the sampling resolution for processing the lidar point cloud needs to be chosen according to the objective and accuracy tolerance of the study and the average overestimation bias needs to be corrected for the study results.

2.4.2 Physiographic effects on snow accumulation

Below 3300 m, the increasing trend of snow accumulation with elevation was observed for all sites (Figure 2.6). Linear regression is applicable to model the relationship between snow depth and elevation when the study area has a broad elevation range. This holds true for all of our sites with the exception of Shorthair, where the elevation range is about 200 m and the coefficient of determination for this linear-regression model is much smaller than for the other three sites, which have ranges greater than 500 m. The bias of mean snow depth in the same elevation band between different sites is acceptable if the standard error is added to or subtracted from the mean (Figure 2.6(a), (b), (c)). The data-collection time, spatial variation and variations of other topographic features can also introduce bias across sites. However, as data-collection time in this study only differed by a few days, in situ snow-depth sensor data suggest that the melting and densification effect was under 2 cm (https://czo.ucmerced.edu/dataCatalog_sierra.html). As for other topographic variables, the observation of a slope effect, shown as the trend lines in Figure 2.7(a) and the negative regression coefficients of the two linear-regression models, could be explained by steeper slopes having higher avalanche potential, fewer trees and thus more wind; and thus some snow is more likely to be lost from these slopes. Snowpack located in south-facing slopes receives higher solar radiation, with the snowmelt being accelerated (Kirchner et al., 2014). This explains the trends observed in Figure 2.7(b) and the negative regression coefficients of the multivariate models. Although lidar has measurement errors caused by slope and aspect (Baltsavias, 1999; Deems et al., 2013; Hodgson and Bresnahan, 2004), the error is not able to be quantitatively traced back to each variable; and we assumed that its influence on the trends could be neglected. As canopy interception results in reduced snow depth under canopy, the snow-depth residuals are found changing from negative to positive with penetration fraction and the regression coefficients are positive (Figure 2.7(c)). The multivariate linear-regression model built from the lidar data is a significant improvement, as the variability of the snow distribution could explain 15-25% more than the univariate linear-regression model with elevation as the only predictive variable (Table 2.4) and the estimation bias has a narrower distribution (Figure 2.10(a), (b)). Also, fitting an individual linear-regression model for each site is slightly better than using a general model with all

data combined (Figure 2.10(c), (d)). This may be because an individual model can capture regional micro-climate within a site better than a general model. The opposite trend of the relative importance of predictive variables observed in Shorthair is because it is a relatively flat site (Figure 2.1, Figure 2.8), which implies that topographic variables other than elevation need to be considered when studying areas with small elevation ranges.

Table 2.4: Coefficients of determination of univariate and multivariate linear-regression models

	Univariate model R^2	Multivariate model R^2
Bull	0.23	0.37
Shorthair	0.06	0.32
Providence	0.39	0.53
Wolverton	0.16	0.38
All sites	0.43	0.57

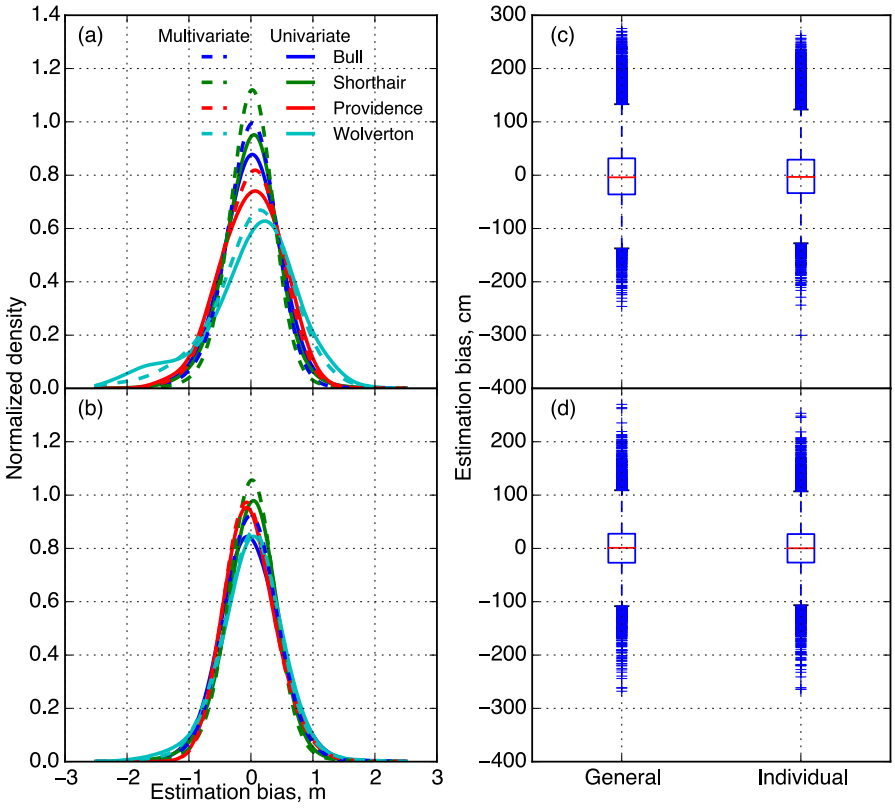

Figure 2.10: Normalized density of estimation bias for (a) open (b) under-canopy areas. Estimation bias boxplots of using one general linear-regression model with all sites data combined and four linear-regression models of each individual site for (c) open (d) under-canopy areas.

2.4.3 Vegetation effects on snow distribution along elevation

Under-canopy snow distribution is governed by multiple factors that affect the energy environment, as observed by melting (Essery et al., 2008a; Gelfan et al., 2004) and accumulation rates (Pomeroy et al., 1998; Schmidt and Gluns, 1991a; Teti, 2003). Our results show different responses when comparing the snow-depth difference between open and canopy-covered areas between study sites (Figure 2.9(a)). In the rain-snow transition zone from 1500 to 2000 m at Providence we see a sharp linear increase between open and under-canopy snow depth that is likely governed by the under-canopy energy environment and the canopy-interception effect on precipitation, which accelerate snowmelt and prevent accumulation of under-canopy snow. Above 2000 m, the snow-depth difference observed at Bull and Shorthair stabilized around 40 cm and 20 cm respectively, with fluctuations less than 10 cm along elevation.

Breaking from this pattern, the large dip in snow-depth difference, down to 10 cm, observed at Wolverton at elevations of 2250-2750 m deviates from the 35-40 cm plateau. Also, the snow-depth difference at Shorthair stabilizes around 20 cm, which is 20 cm lower than the stabilized value at Bull. Based on the scatterplots shown in Figures 2.6(a) and (b) that are color coded by northness, at an elevation range of 2300-2700 m, there are a lot more data points with both low snow depth and extremely negative northness in the open area than under the canopy, which implies that anisotropic distribution of other topographic variables is affecting the snow-depth difference. This is further shown by filtering out the data points not within a small certain range (-0.1 to 0.1) of northness, and then reproducing Figure 2.9(a) using the filtered data. As presented in Figure 2.11, it is apparent that the large dip at Wolverton is flattened out owing to a canopy effect of around 25-45 cm. Thus a sigmoidal function was used to characterize the snow-depth difference changes with elevation, excluding topographic interactions. The interactions between topographic variables and vegetation is most likely attributable to the under-canopy snowpack being less sensitive to solar radiation versus snowpack in the open area (Courbaud et al., 2003; Dubayah, 1994; Essery et al., 2008a; Musselman et al., 2008, 2012).

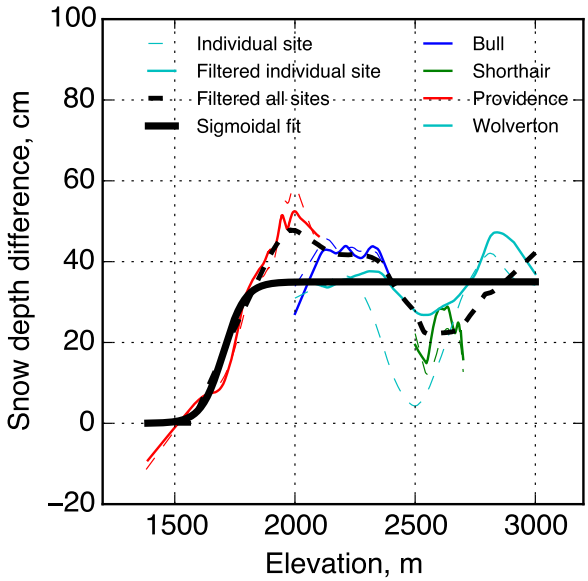

Figure 2.11: Snow-depth difference between open and under-canopy areas versus elevation, calculated as difference between raw 1-m pixel snow depth and northness-filtered 1-m pixel snow depth, together with the sigmoidal fit of the snow-depth difference.

In spite of filtering the topographic effect, there is still about a 20-cm magnitude of fluctuation in the snow-depth difference, which might be attributed to various clearing sizes of open area at different locations and various vegetation types in forests (Hedstrom and Pomeroy, 1998; Pomeroy et al., 2002; Schmidt and Gluns, 1991a); however, we were not able

to explore these features of the sites from the current lidar dataset.

2.5 Conclusion

The rasterized lidar data show that the percentage of pixels with at least one ground return, and thus a snow-depth measurement, increases from 65-90% to 99% as the sampling resolution increases from 1 m to 5 m. However, this coarser resolution may mask undersampling of under-canopy snow relative to snow in open areas. With about 28% of the area in dense mixed-conifer forest having no returns, using snow depths in open areas as estimates of snow depth under dense canopies would result in at least a 10-cm overestimation error in the average snow depth in the main snow-producing elevations of 2000-3000 m.

Using lidar data gridded at 1-m resolution, average snow depth within each 1-m elevation band shows a strong correlation with elevation and consistent pattern across all sites. The linear-regression models show that elevation explains 43% of snow-depth variability; and that over 57% of the variability is explained when including all physiographic variables. This indicates that snow distribution in the southern Sierra Nevada is primarily influenced by an orographic-lift effect on precipitation. Snow-depth residuals calculated by de-trending the elevation dependency are correlated with slope, aspect and penetration fraction; and the regression coefficients of these variables in the multivariate linear-regression model show that they are statistically significant in explaining the snow-depth variability, all with p-values smaller than 0.01. Over the elevation range of 1500-3300 m, snow depth decreases 1 cm per 1° slope, and decreases 0.5 cm per 1° aspect in going from north to south. In open areas, snow depth increases 2 cm per 10% increase in penetration fraction, while under canopy the snow depth increases 10 cm per 10% penetration-fraction increase. Although the latter three variables were observed to be less important than elevation, the relative importance of all four variables varies with local elevation range and canopy.

The snow-depth difference between open and canopy-covered areas increased in the rain-snow transition elevation range and then stabilized around 25-45 cm at high elevation. Fluctuations in certain elevation ranges are attributed part to interactions from other topographic variables. Evidence of this is found by filtering northness into a narrow band, which results in these fluctuations flattening out.

Chapter 3

Canopy and terrain interactions on spatial distributions of snowpack in the Sierra Nevada

3.1 Introduction

The snowpack in California's Sierra Nevada has long served as the primary water resource for agriculture and urban uses (Bales et al., 2006). Spring snowpack measurements across mountain basins are the foundation of forecasts of water availability. As forecasts for both seasonal water supply and flood peaks following the onset of melt turn from statistical to spatial water-balance approaches, predictions require accurate estimates of both precipitation and snowpack water storage (Hopkinson et al., 2001). Quantifying the spatial distribution of snowpack properties in forested mountainous areas is the long-standing, grand challenge in snow hydrology (Winstral and Marks, 2013; Golding and Swanson, 1986). In the high Sierras, orographic effects drive solid-phase precipitation falling over mid-to-high elevation regions, where most areas are covered with heterogeneous densities and different types of vegetation (Houze, 2012; Mott et al., 2014). The mountain's local topography introduces heterogeneity into snow-surface energy balance, which further increases spatial variabilities in snow melt and total snow volume at different scales (Marks et al., 1998, 1999). Various vegetation types and canopy densities above the snow surface make answering this question even more challenging (Musselman et al., 2012).

A major effect that coniferous canopies have on snowpack is the formation of tree wells, which are the areas with relatively lower snow depth under the canopy. Tree wells form in both snow accumulation and melting processes, dominantly by canopy interception, sublimation, and melt associated with enhanced incident thermal radiation to the snowpack, and unloading resulting in less accumulation of snow beneath canopies (Musselman et al., 2008; Sicart et al., 2004). Other than snowpack quantity, these physical effects can also result in heterogeneity in snow density, grain size, and snowpack metamorphosis (Musselman et al.,

2008, 2012). Understanding and being able to quantify these effects can be beneficial as snow models are refined to better describe spatial heterogeneity. Understanding and being able to quantify these effects will be beneficial to refine existing snow models.

Previous studies have discussed the topography-snow depth and vegetation-snow depth relationships independently (Varhola et al., 2010). Regression models and ensemble models were built for quantitatively analyzing patterns of each variable's impact and retrieving variable importances for estimating snow-depth spatially (Molotch and Bales, 2005; Molotch et al., 2005; Musselman et al., 2008). Topographic variables such as elevation and northness are important in quantifying snow-depth spatial distribution, as orographic effects drive more precipitation at higher elevations and more energy on south-facing slopes drives snow to melt faster (Zheng et al., 2016). Leaf-area index (LAI) and distance from tree bole, are two influential vegetation variables in determining snow-depth spatial distribution under canopies, the snow-depth variabilities caused by which are mostly due to varied capacities in intercepting snowfall; i.e., forest with higher LAI intercepts more snowfall and canopy leaves are less dense at the drip-edge than those are closer to the tree bole (Revuelto et al., 2015).

However, observational studies regarding how topography and vegetation interactively affect snow depth have rarely been conducted, reflecting the relative lack of high quality field data in mountains (van Heeswijk et al., 1996; Marks et al., 1998). Several control groups with respect to topographic variables and vegetation variables have to be sampled such that the altered effects across groups can be observed. Therefore, the number of samples needed will be a few times greater than in previous work. Also, varied topographic and vegetation conditions are preferred in study areas so as to extend the applicability of the results.

Regarding the measurements techniques, canopy metrics like LAI can be retrieved from satellite imagery (Zheng and Moskal, 2009; Gowda et al., 2015), however, when studying on a finer resolution (meter or sub-meter), most previous studies were based on manual surveys (Molotch and Bales, 2005; López-Moreno and Latron, 2008; Musselman et al., 2008), the samples of which are insufficient for drawing statistically significant conclusions. Similar situations exist in snow-depth surveys using sensors, although ultrasonic snow-depth sensors can be used to continuously measure snow depth, the spatial densities of sensors are minimal comparing to the scale of mountains. Over the past two decades, with lidar becoming more widely used as a remote-sensing technology in forestry and water resources mapping (Kelly and Di Tommaso, 2015), canopy structures can be detected and extracted using point-cloud data and image-processing algorithms (Li et al., 2012; Strîmbu and Strîmbu, 2015). In addition, by using change-detection techniques, spatial snow-depth mapping can be retrieved from snow-on and snow-off lidar scans over the same region (Hopkinson et al., 2001). With dense and wide-spread spatial measurements from lidar, it is expected that this technology can help fill the knowledge gap of how terrain and canopy interactions affect the spatial distribution of snow.

The overall aim of the work reported here is to improve our understanding of the canopy-terrain interactions on snow-depth spatial distribution. Using lidar data from four forested headwater areas in the southern Sierra Nevada, we addressed three questions. First, to what extent can one measure snowpack under canopy using airborne lidar? Second,

how do topography and canopy interactively affect snow-depth spatial distribution? Third, how important are these effects for estimating spatial snow quantities at different lidar measurement resolutions?

3.2 Methods

We analyzed four lidar footprints collected in the southern Sierra Nevada, California (Figure 3.1). The lidar data were processed into point clouds, with point densities from 0.1 pts $\cdot$ m^{-2} to 10 pts $\cdot$ m^{-2} and raster data sets at resolutions from 0.5×0.5 m^2 to 30×30 m^2. The canopy-height models processed from the lidar footprints were processed with tree-segmentation algorithms. The snow depth and tree-well pattern beneath the segmented trees were evaluated relative to local topographic conditions and the samples analyzed to determine how terrain and vegetation affect the spatial snow-depth distribution. We also applied a machine-learning model to predict snow depth at 0.5-m resolution, with topographic and canopy related predictors, aiming for modeling the spatial distribution of snow depth at lidar resolutions.

3.2.1 Study areas and lidar data acquisition

The study areas, Bull Creek, Shorthair Creek, Providence Creek and Wolverton Basin, are headwater study areas of the Southern Sierra Critical Zone Observatory (SSCZO), three of which are located in the upper Kings River basin, with Wolverton 80 km south in the adjacent Kaweah River basin (Figure 3.1). The four study areas range from 1500 to 3500 m in elevation (Table 3.1). Vegetation density among all sites generally decreases in high-elevation subalpine forest, with Wolverton having a large area above treeline (Goulden et al., 2012; Kirchner et al., 2014). The total surveyed area for both snow-on and snow-off data is about 150 km^2, with snow-on footprints collected in late March 2010, near peak accumulation, and snow-off footprints collected in August 2010. The 2010 water year had a wet snow season with mean snow depth of 2 m over the four sites (Zheng et al., 2016). The survey was performed by the National Center for Airborne Laser Mapping (NCALM) using Optech GEMINI Airborne Laser Terrain Mapper. The snow-on lidar data set has an average point density of 9.2 pts $\cdot$ m^{-2}, with the snow-off data averaging at 11.7 pts $\cdot$ m^{-2}.

3.2.2 Lidar data processing

The lidar data were processed to generate raster data. The raw point-cloud files were divided into 250 × 250-m^2 tiles using the LAStools software (Isenburg, 2014). We extracted the ground points from each tile and interpolated them into a 0.5 × 0.5-m^2 resolution digital elevation model (DEM) using a simple kriging model with a spherical covariance function, using the ArcMap for Desktop and its ArcPy Python application programming interface

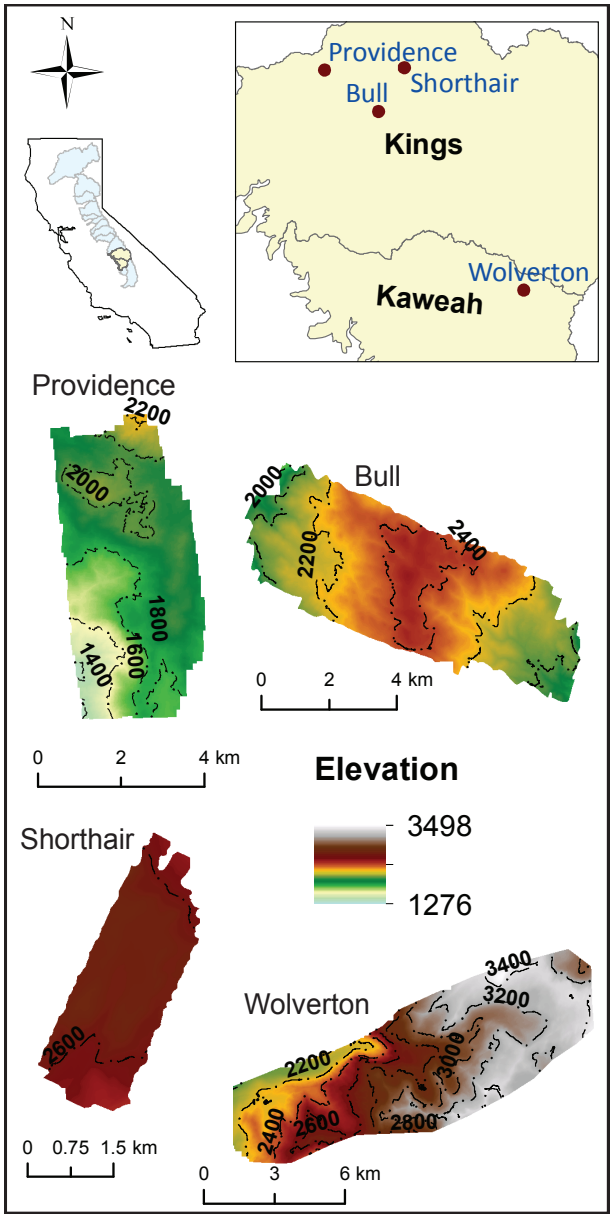

Figure 3.1: (a) The study areas are located in three watersheds: American river, Kings river, and Kaweah river basins of the Sierra Nevada mountains. Duncan and Dolly are in the north fork of American river basin. Providence, Shorthair, and Bull are in the upper Kings river, whereas Wolverton is on the boundary of Kings river and Kaweah river basins. (b) Digital elevation model derived from lidar footprints of the six study areas.

(ESRI, 2015). The 250×250-m^2 DEM tiles were mosaic-ed together to form a single DEM for each individual study area.

Table 3.1: Study sites general information

		Elevation range, m			Slope, deg		Aspect, deg	
Site	Area, km^2	min	max	Number of plots	min	max	min	max
Bull	20.7	1823	2490	37	9.5	22.3	114	264
Shorthair	5.4	2449	2753	6	12.4	16.7	81	219
Providence	18.4	1352	2218	32	10.7	27.0	145	258
Wolverton	48.0	1718	3496	84	12.8	64.7	21.3	306

A digital surface model (DSM) was generated from all first returns of the lidar point cloud. We produced a canopy-height model (CHM) by subtracting the DEM from the DSM. By using the watershed-segmentation algorithm (Roerdink and Meijster, 2000), individual trees can be segmented from the canopy-height model. The snow-depth pixels beneath each tree were also extracted.

3.2.3 Lidar point density analysis

The lidar point density (ρ) was calculated by dividing the total number of points by the projected concave area on the two-dimensional (2-D) xy-plane. The collected point-cloud density for snow-depth mapping was usually lower than 1 pt $\cdot$ m^{-2} because the laser pulses were intercepted by canopy. On average, about 5% of the point cloud are ground points over a forested area (we have tested our data set and the percentage was greater than 5%), suggesting that at least 40 ground points can be measured under a tree with a crown diameter of 10 m when the point density is about 10 pts$\cdot$m^{-2} and thus the snow-surface profile should be observable. However, how the low point density influences the total snow volume or snow water equivalent (SWE) is still unclear. In order to study the changes of lidar-derived total snow volume with the lidar point density, this study randomly resampled the snow-on point cloud data with a density ρ at a variable percentage ($\rho'/\rho,\ \rho' \leq \rho$) to get points with different densities (ρ'). Each dataset with various point densities was used to interpolate a snow-depth product using kriging, as noted above. The total volume of snowpack derived from each data set with resampled point-cloud density was calculated for comparison. We also explored how various DEM resolutions (from 0.5 m to 30 m) influence the estimated snowpack volume. The DEMs with various resolutions were generated from the original point cloud.

3.2.4 Study plot segmentation

The terrain of the four study areas were lumped into one data set for analysis, giving a broad elevation range, mild and steep slopes, and various aspects. Exploring interactions between terrain and vegetation over areas with heterogeneous topography is a non-trivial task because of the confounding effects from multiple topographic attributes. One solution

is to control the potential confounders by making their values in a narrow range. Thus, we segmented each study area by using the National Agriculture Imagery Program (NAIP) dataset, topographic data layers, and Felzenszwalb segmentation algorithm (Felzenszwalb and Huttenlocher, 2004). The algorithm merges pixels based on neighboring pixels' similarities, by doing which the neighboring pixels with similar topography and vegetation densities can be merged together and thus the value ranges of confounders can be controlled in a narrow range within a single segment. We used the algorithm implemented in the scikit-image (van der Walt et al., 2014) Python library for segmenting the multi-channel imageries. On average, the size of the segmented study plots are 0.4 km^2.

3.2.5 Statistical analysis and modeling

3.2.5.1 Terrain and canopy attributes from lidar

The spatial distribution of snow in mountainous forested areas is controlled by orographic effects, wind redistribution, and canopy (Mott et al., 2014; Houze, 2012; Winstral et al., 2002). Other than canopy, the rest of the spatial variability of snow depth are largely related to the topography of the area. The snow-depth dependency can be represented by the following equation

$$h = f(t, c) \tag{3.1}$$

where h stands for snow depth, t stands for topographic variables, and c stands for canopy variables. In our study, the topographic variables are elevation, slope, aspect, northness, and topographic roughness index. The canopy variables are canopy height, distance to tree bole, and canopy-terrain shadow. To study the snow-depth profiles of tree wells, both globally and under certain terrain circumstances, we extracted the distance to tree bole and direction from tree bole of each individual snow-depth pixel, using the coordinates of the pixel and the segmented tree polygon. We used the centroid of each segmented tree polygon as the tree bole location. The distance was calculated as

$$r = \Delta x^2 + \Delta y^2 \tag{3.2}$$

whereas the direction was calculated as

$$\theta = \arctan(\frac{\Delta y}{\Delta x}) \tag{3.3}$$

where Δx and Δy are distances the tree bole in x and y directions, respectively. θ was further converted from $[-180°, 180°)$ to $[0°,\ 360°)$ so θ is consistent with the aspect of the terrain. For each snow-depth pixel under the canopy, we calculated the standard deviation of the height of the tree above, and its crown area. In addition, we extracted a 5-m-radius circular area surrounding each snow-depth pixel and calculated the percentage of canopy-height pixels that are above 2 m. Outside the 5-m radius the canopy coverage was less correlated with snow depth.

3.2.5.2 Terrain and canopy interaction

We sampled study plots from the segmentations described in Section 3.2.4. As the aspect of certain study plots can be highly variable, we filtered the segmentations whose standard deviations of aspects were larger than 50°. For the remaining sampled plots, we developed two approaches to analyze the terrain-canopy interactions relative to snow depth.

For the first approach, we divided the plots into four groups by aspect, north, east, south, and west, based on the mean aspect value of each plot. The north group has plots with mean aspect in the range of $0°-45°$ and $315°-360°$. The east group has plots in the range of $45°-135°$. The plots in the south and west groups have 90° and 180° increments, respectively, based on the range of the east group. We then randomly sampled 10 plots from each group with replacements, meaning that we allow repeating samples in the sampled 10 plots. The reason for using replacements is because there were only 9 plots available in the west group. We verified that the samples from the north, east, and south groups were representative with regards to the distributions of topographic variables (Figure 3.2). The west group only covers a narrow range of elevation, which can be a biased sampling group for this analysis. For each sampled plot, we binned θ at a 30° increment. The snow-depth pixels were aggregated and the mean of snow depth was calculated for each bin of θ. Then the mean snow depths were visualized versus θ over the polar coordinate system for each group separately.

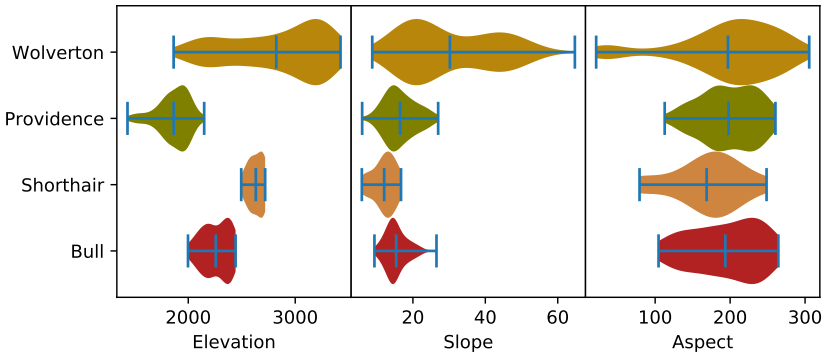

Figure 3.2: The distribution of topographic attributes for all segmented study plots of each headwater catchment site.

For the second approach, all remaining segmented plots from the filtering noted above were analyzed individually. Here we define the center of mass of all normalized snow-depth-pixel values under canopies.

$$\Delta x_c = \frac{\sum_{i=1}^{n} \Delta x_i \times h_i}{\sum_{i=1}^{n} h_i} \quad \Delta y_c = \frac{\sum_{i=1}^{n} \Delta y_i \times h_i}{\sum_{i=1}^{n} h_i} \tag{3.4}$$

The coordinates of the calculated center of masses can be converted to polar coordinates using Equation (3.2) and (3.3) to get the distance r_c and the direction θ_c from the tree bole

to the center of mass. We conducted a regression analysis between θ_c and the local aspect direction, r_c and local slope steepness of each study plot.

Both independent and dependent variables in the regressions were derived from a series of processing steps over the study plots that have a mixture of terrain and canopy conditions. To make the regression analysis more robust, we detected outliers over the 4-D space $(\theta_c, r_c, \text{aspect}, \text{slope})$ using an elliptic envelope approach that was implemented in the scikit-learn Python library (Pedregosa et al., 2011). Here we assumed that the data over the 4-D space are normally distributed.

Other than the dominant directions of tree wells, the gradient of tree well, which describes the steepness of the snow surface from the tree bole to the drip edge, can be another index representing the spatial distribution of the tree-well snow depth. For each segmented tree, we extracted all snow-depth pixels under each tree and applied linear regression of snow-depth values versus their distance to the tree bole. The slope of the univariate regression was used to characterize the gradient of tree well. We investigated the relationship between the slopes of tree wells and crown area of trees by binning the crown area from 0 to 20 m^2 at a 2-m^2 increment and calculating the mean tree-well slope for each bin.

To assist in interpreting our findings on tree-well gradients from the perspective of snow melt, we used a degree-day method with the daily temperature data from the met stations at these sites, as the incoming longwave radiation that strongly drives snow melt at early season and degree day is a good indicator of the magnitude of snow melt (Ohmura, 2001). We selected 13 March as the starting date for accumulating the degree day because that is when the most recent precipitation ends. We also retrieved the snow-pillow snow water equivalent measurements from Upper Providence (1950 m), Tamarack Summit (TMR, 2300 m), and West Woodchuck Meadow (WWC, 2700 m). Both TMR and WWC data were downloaded from the California Data Exchange Center. These two sites were selected because they are geographically closer to the study areas and their local elevations are within the elevation ranges of the study areas. We compared the estimated snow melt at the met stations and the observed snow melt at these snow-pillow sites from 13 March to 23 March.

The zonal statistics (mean, standard deviation) of tree-well snow depth were also retrieved and we engineered three canopy statistics: canopy-height standard deviation, crown area, and percentage of canopy coverage within a 10-m radius. We increased the radius for calculating the canopy coverage to make sure that the tree above can be included in this coverage statistic. The zonal mean values of snow depth were detrended by topographic variables before they were further investigated. Principal component analysis (PCA) is commonly used for projecting a set of possibly linearly correlated variables into uncorrelated variables. We used a biplot of PCA for interpreting the correlations between zonal statistics of snow and canopy; we estimated the bivariate distribution of variable pairs by using a Gaussian kernel density estimation.

3.2.5.3 XGBoost modeling of snow depth

In order to study how much spatial variability of snow depth these topographic and canopy variables can explain, we modeled the function f in Equation (3.1) by using an Extreme Gradient Boosting (XGBoost) model (Chen and Guestrin, 2016). The XGBoost model is an ensemble method that is comprised of a series of regression trees that are trained in an additive training procedure. In order to determine if the XGBoost model can quantify the tree-well snow depth correctly, we applied the XGBoost model twice. At first we used it to detrend the snow-depth dependencies on the topographic attributes. Then we used it again to model the detrended residuals using canopy attributes. Comparing to other ensemble methods such as Random Forest and Gradient Boosting Machine, the XGBoost model has more hyperparameters that need to be tuned. Important parameters that affect model performance include: number of estimators (n_estimators), maximum regression tree depth (max_depth), minimum number of samples in a child node (min_child_weight), minimum loss reduction threshold (γ), percentage of data samples (subsample), percentage of attribute samples (colsample_bytree), $L1$ or $L2$ regularization parameters (α or λ), and learning rate (λ). We tuned these parameters one after another by using a five-fold cross-validation scheme with an exhaustive grid search approach. We gained 2 sets of parameters, one set for topographic attributes only and the other set for canopy attributes only. Considering that the XGBoost approach is computationally intensive, we sampled 200,000 pixels from all lidar data for tuning and building the model. The loss function used for training the model is the mean-squared loss,

$$L = \sum_{i}^{n} (y_i - \hat{y}_i)^2 \tag{3.5}$$

We evaluated the trained models by using coefficient of determination R^2,

$$R^2 = 1 - \frac{\sum_i^n (y_i - \bar{y})^2}{\sum_i^n (y_i - \hat{y}_i)^2} \tag{3.6}$$

where y_i is the ith observed snow depth, $\bar{y}$ is the mean of all observations, and $\hat{y}_i$ is the ith model estimate. All computations are implemented using the XGBoost library and its Scikit-Learn application programming interface in Python.

In addition, we manipulated the testing dataset to determine the canopy-thinning effect on snow depth near peak accumulation. We selected the canopy height as the treated variable because it is more important than CTS in the XGBoost model. For the entire testing dataset, we randomly selected x% of total pixels where x was from 10 to 50 with an increment of 10. For the sub-sampled pixels, we multiplied their canopy heights by a percentage that is uniformly drawn from y% to 100% where y was from 10 to 90 with an increment of 20. We calculated the mean snow depth that was estimated from the XGBoost model with the manipulated inputs.

3.3 Results

We observed snow depth under canopy with both lidar point-cloud and 0.5×0.5-m^2 resolution imagery. By extracting a cross-section of canopy points from snow-off lidar point-cloud data and ground-surface points from snow-on lidar point cloud, we observed snowpack surface under both dense and sparse canopies (Figure 3.3a, b). The under-canopy snow surface has a concave shape, versus flat in the open. A similar pattern was observed with rasterized snow-depth data (Figure 3.3c).

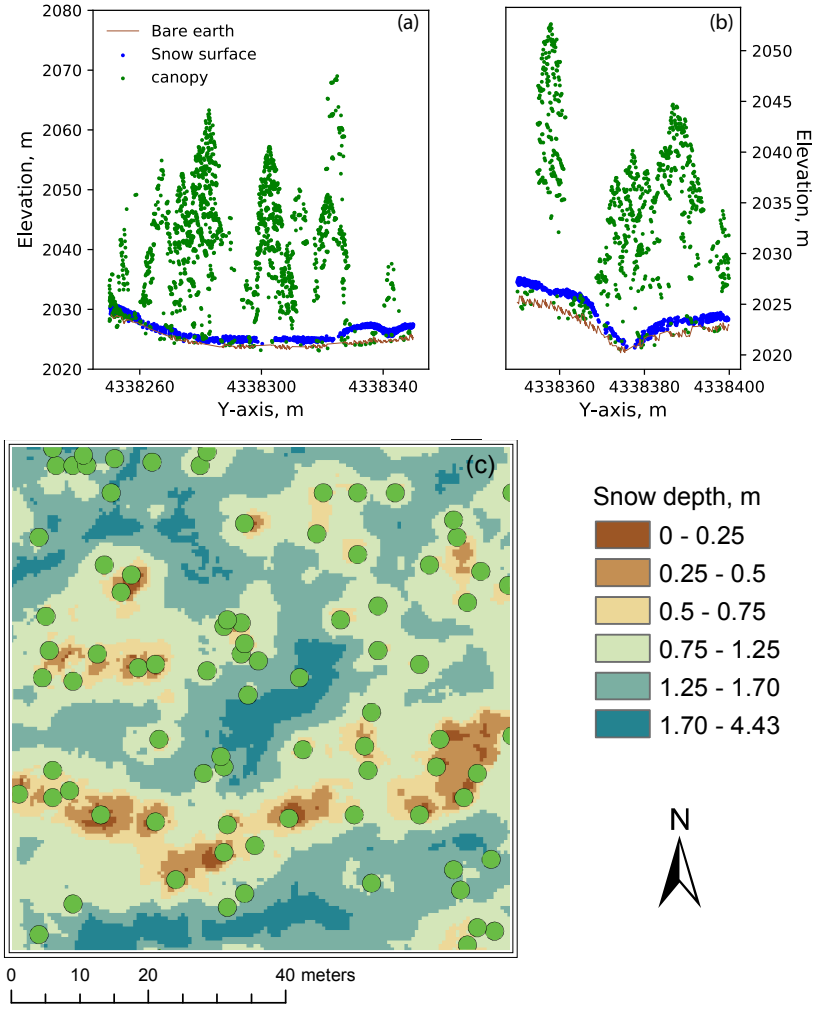

Figure 3.3: Snow-depth visualization using (a) point-cloud data with clustered canopies (b) sparse canopies, and (c) rasterized snow-depth with green markers, which are the tree tops detected from the canopy height model using the tree segmentation algorithm.

3.3.1 Snow depth interpolation using lidar with various point-cloud density

Overall, the lidar-derived total snow volume showed a slight increase with the decrease of point density when it is lower than 1 pt $\cdot$ m^{-2}, and then becomes stable afterwards (Figure 3.4). The decrease in point density only accounts for 0.5% less total snow volume at 3 sites, but a 20% decrease at the lower-elevation Providence site. Moreover, the change of point density can influence the spatial distribution of snow depth, with interpolated snow surface becoming smoother as point density decreases. The change of DEM resolution has little influence on the total snow volume estimation. However, no clear trend was observed between the snow-volume estimates and DEM resolution (Figure A.1).

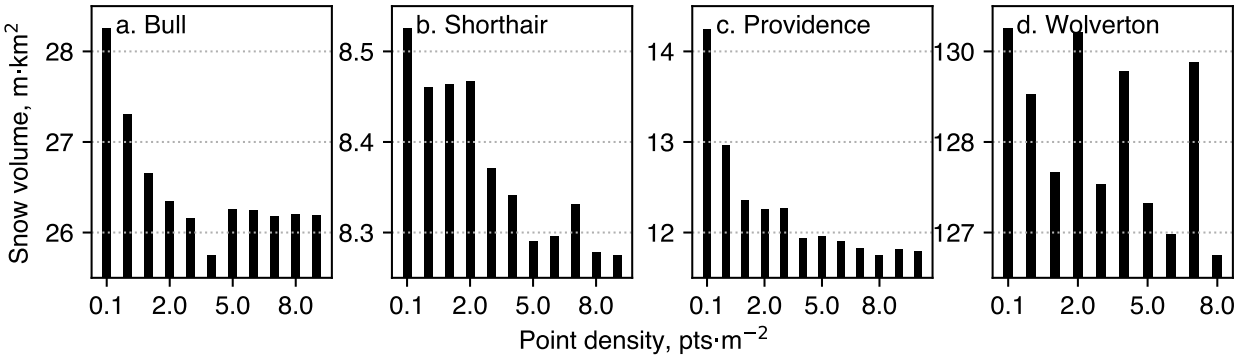

Figure 3.4: Changes of lidar-derived total snow volume with the lidar point density at (a) SSCZO Bull site, (b) Shorthair site, (c) Providence site and (d) Wolverton site.

3.3.2 Dominant tree-well directions

By applying the first approach introduced in Section 3.2.5.2 analysis, plots by dominant aspect, we observed that the under-canopy snow-depth distributions also depend on aspect. The snow depth is deeper if the direction from the tree bole to the snow-depth pixel location is the same as the local aspect, with the opposite direction usually having the shallowest snowpack (Figure 3.5). Both north-slope and east-slope groups strongly indicate this pattern, with the deeper side having about 40% more snow than the shallower direction. The south-slope and the west-slope groups have a weaker pattern, with the deepest directions shifted to the southeast and southwest, respectively, and deeper side having 10-15% more snow than the shallower side.

For the second approach in Section 3.2.5.2, we found that the direction from the tree bole to the center of mass (θ_c) for under-canopy snow at each individual study plot is positively correlated with the local aspect, with $R^2 = 0.47$ and p-value < 0.01 (Figure 3.6). The distance (r_c) from the tree bole to the center of mass is negatively correlated with the local

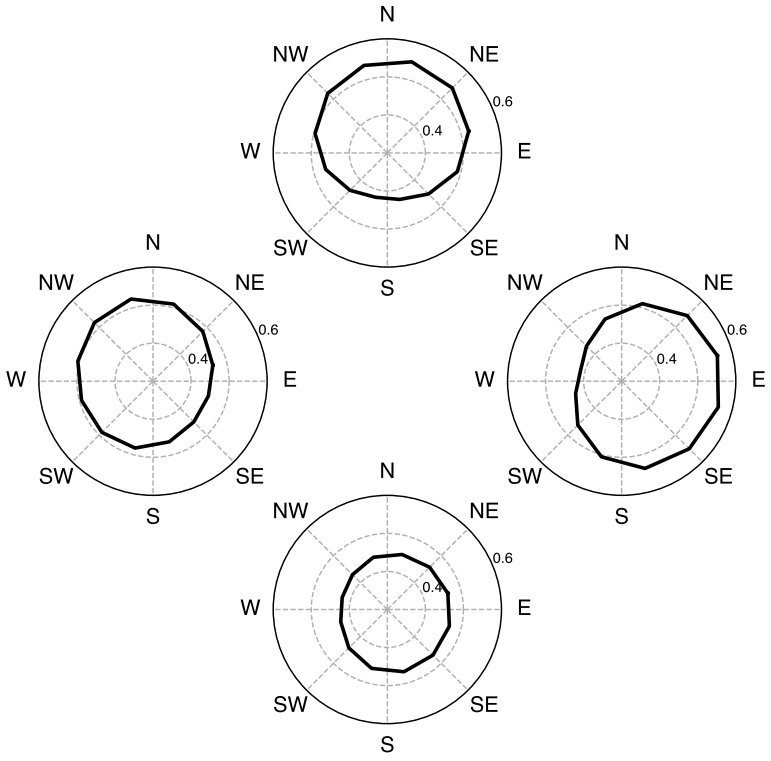

Figure 3.5: Averaged normalized snow depth under individual segmented canopy over each direction bin at four different directions slopes. The snow depth is higher in the direction that is consistent with the local aspect, i.e., for a north facing slope, the snow under the north side of the canopy is deeper whereas under the south side is shallower.

slope of the study area, with $R^2 = 0.17$ and p-value < 0.01 if the 4-D outlier detection described in Section 3.2.5.2 is used before the regression analysis. The first finding is significant and consistent with what was found using the first approach. The second finding implies that the interactions between canopy and local aspect will decay as the local slope becomes larger, however, the finding is only significant when the multivariate outliers are removed from the dataset. In order to quantify the observed trends numerically, we parameterized a new variable, canopy-terrain shadow (CTS),

$$CTS = (1 - \sin(\text{slope})) \times \cos(\theta - \text{aspect}) \tag{3.7}$$

which can be used in pixel-level modeling. The correlation analysis (Figure not shown) shows that the snow-depth residuals detrended from topographic variables increase as CTS becomes larger (p-value < 0.01).

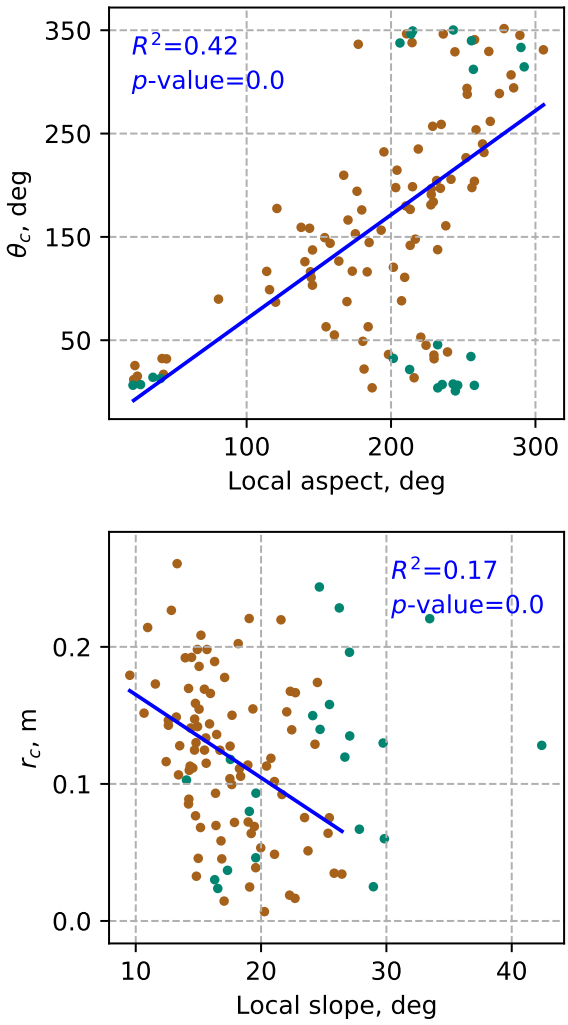

Figure 3.6: (a) The direction from center of tree wells to the tree boles (θ_c) versus local aspect and (b) the distance from center of tree wells to the tree boles (r_c) versus local slope. The green markers are outliers detected from the multivariate outlier-detection algorithm.

3.3.3 Tree-well gradients and under-canopy snow depth

The gradients of tree wells are likely to be controlled by the size of the tree above. As crown area increases, the tree-well slopes become steeper for all elevation bands except for above 2950 m (Figure 3.7). On average, the snowpack is 2 cm deeper for every 1 m away from the tree bole when the crown area is more than 8 m^2. Additionally, the slopes of tree wells are also correlated with topographic variables. However, the terrain effects can be altered as the phase of precipitation changes from rain to snow and snow melts. Providence, lies in the lower elevation range, and tree-well gradients are correlated with elevation, which is only

observed in this site (Table 3.2). For roughness and slope of the landscape, at Shorthair, these two variables are positively correlated with the tree-well gradient, while opposite trends are observed at Providence and Wolverton. The correlations with roughness and slope are not significant at Bull.

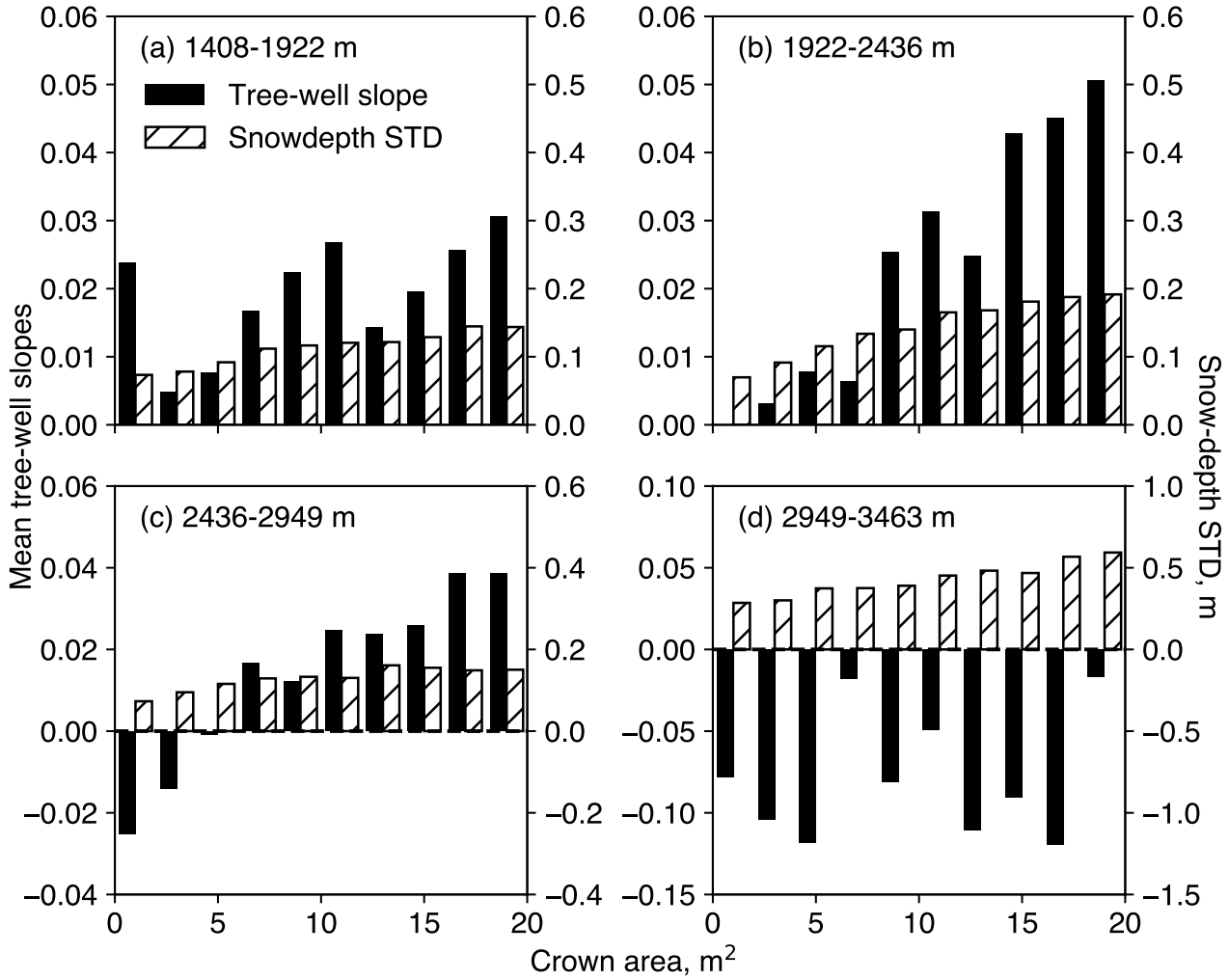

Figure 3.7: Tree-well slopes and snow-depth standard deviations for all tree wells versus crown areas by four elevation bands, indicating that as the crown area growing larger the snow-depth will have a wider distribution, and the tree-well gradient will become steeper except at the highest elevations.

The biplot (Figure 3.8a) from PCA indicates that the zonal average of snow depth is negatively correlated with all canopy attributes. The scatter plots in Figure 3.8 suggest some important correlations. First, while a taller tree and larger tree-height standard deviation can be expected to intercept more precipitation, the data suggest that the marginal effect from

Table 3.2: Correlation coefficient (R) and p-values calculated between tree-well gradients and topographic variables.

	elevation		northness		roughness		slope	
Study area	R	p	R	p	R	p	R	p
Bull	0.03	0.10	0.10	0.00	-0.01	0.51	-0.02	0.16
Shorthair	-0.02	0.24	0.02	0.31	0.16	0.00	0.17	0.00
Providence	0.23	0.00	0.07	0.00	-0.08	0.00	-0.09	0.00
Wolverton	-0.02	0.18	-0.04	0.01	-0.07	0.00	-0.06	0.00

canopy height is stronger when the height is lower than 5 m. Also, the effect from individual tree saturates as the standard deviation of canopy height reaches 4 m (Figure 3.8b). On average, the snowpack beneath a tree with near-constant height can be at least 0.2 m deeper than that under a tree with varying height (Figure 3.8d). However, the tree-height standard deviation is strongly correlated with average tree height, such that the causal effect cannot be identified with the current data set. Second, the strong effect from the surrounding canopy coverage suggests that under-canopy snow depth is not only affected by the tree above but also the surrounding canopy (Figure 3.8c). When trees are clustered together, the snowpack tends to be shallower, which is consistent with the findings from raw lidar visualization. Third, canopy size does not significantly affect the mean under-canopy snow depth, but notably affect the standard deviation of snow depth (Figure 3.8e).

3.3.4 Modeling results

3.3.5 Prediction of snow-depth patterns

We first modeled the snow depth using topographic variables only, which include elevation, slope, aspect, northness, and roughness. The tuned hyperparameters are shown in Table 3.3. By just using topographic variables, the testing R^2 equals 0.69, which is much higher than the Random Forest based model using the same data set (Zheng et al., 2016). By excluding the measurement error of 15 cm from lidar (Deems et al., 2013) from the total error of 43 cm, the testing root-mean-squared error (RMSE) is 40 cm. The snow-depth values were detrended using the best XGBoost model with topographic variables and the detrended residuals were modeled with the canopy variables (canopy height, distance to tree bole, and canopy-terrain shadow). However, the spatial variability that can be explained from the canopy variables is almost negligible comparing to that from topographic variables. The CTS variable is also the least important variable among the three. By inspecting the first two regression tree structures (Figure A.2), the canopy-terrain shadow started splitting data from the second regression tree, which confirmed it is weaker compared to the other canopy-related variables. The model combined both topographic variables and canopy variables

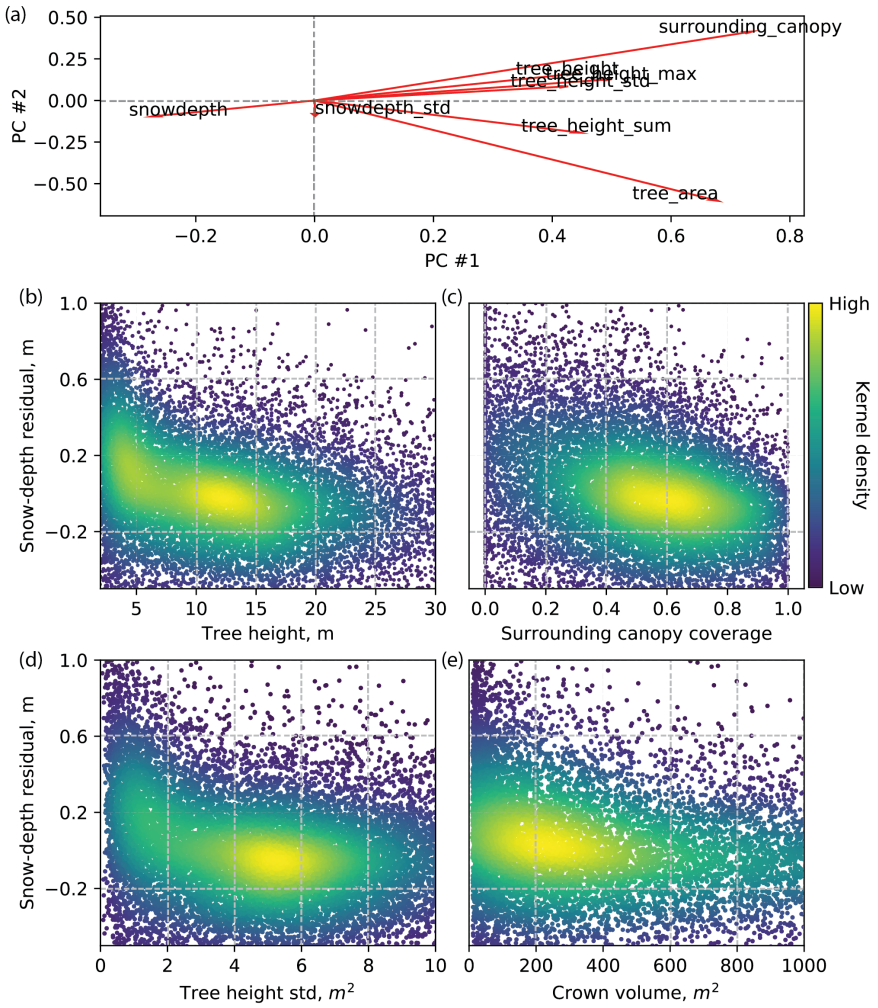

Figure 3.8: (a) Principal component analysis Detrended Under-canopy snow-depth zonal mean versus (a) canopy height standard deviation, (b) percentage of canopy covered area within 10-m radius. And under-canopy snow-depth zonal standard deviation versus (c) canopy area (d) percentage of canopy covered area within 10-m radius

has a slight improvement, with testing RMSE = 39 cm and $R^2 = 0.71$. Using the trained XGBoost model with the manipulated testing dataset, we found that the mean snow depth increases from 1.46 m to 1.50 m when there are 50% pixels manipulated with at most 90% of tree-height reduction. When there are at most 10% of tree-height reduction, the mean snow depth does not increase much (Figure 3.9).

Parameters	Tuning range	Tuned value			Tuned loss		
		Topo	Canopy	Both	Topo	Canopy	Both
n_estimators	0-5000	3000	3000	3000	0.174	0.10486	
max_depth	2-12	9	3		0.156	0.10404	
min_child_weight	1-6	5	4		0.156	0.10404	
γ	0.1-0.5	0.4	0.2		0.1559	0.10403	
subsample	0.6-0.9	0.9	0.7		0.1554	0.10401	
colsample_bytree	0.6-0.9	0.9	0.7		0.1554	0.10401	
α	0-1	1e-5	1e-5		0.1554	0.10401	
learning rate	0-1	0.01	0.01	0.01	0.1552	0.10401	

Table 3.3: XGBoost model hyperparameters tuning results

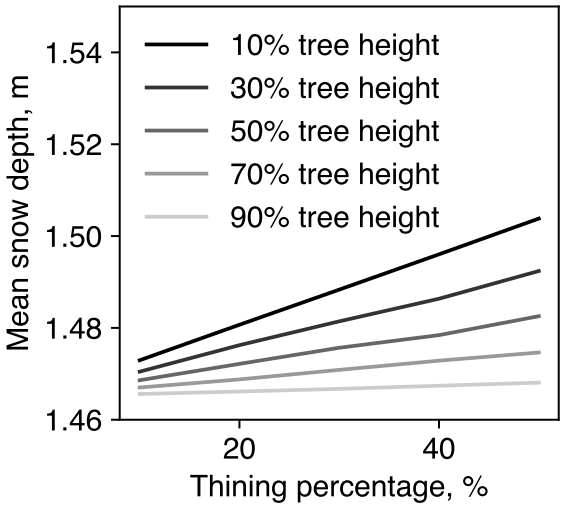

Figure 3.9: The mean snow depth of each 0.5×0.5 m^2 pixel that estimated from the XGBoost model, in which the canopy-height features were randomly adjusted to 10%, 30%, 50%, 70%, and 90% of its original height. And the manipulated pixels were randomly selected from the data set with 10%, 20%, 30%, 40%, and 50% probability. The mean snow depth linearly increases with the percentage

3.4 Discussion

3.4.1 Lidar point-cloud density effect on snow-depth estimation

The lidar point density had no significant influence on the estimation of total snow volume, although it can influence the mapped spatial distribution of snow depth. The main reason for this may be the overall smoothing effect of low-density lidar data. The low point density

may result in under-sampling of tree wells, which leads to an overestimation in the rasterized snow-depth products and total snow volume. However, the low point density may also result in under-sampling points in open and drip-edge areas with higher snow depth, which leads to an underestimation of total snow volume. The overestimation of snow depth in tree wells and the underestimation at snow peaks may balance the total snow volume estimation. However, with greater vegetation coverage, the overestimation in tree wells may become larger than the underestimation in the open. This might be the reason for the sharp increase of total snow volume at Providence when the point density becomes lower than 1 $\text{pt} \cdot \text{m}^{-2}$. Providence has a relatively larger vegetation coverage than the other three sites. Guo et al. (2010) suggested that a point density of 1 $\text{pt} \cdot \text{m}^{-2}$ is enough to generate DEM with very high accuracy, and the further increase of point density cannot bring significant change in the DEM accuracy. Therefore, we suggested that a minimum of 1 pt/m^2 lidar point density should be achieved for snow-depth estimation for cases without rain and before melt. The DEM resolution had no significant influence on the estimation of total snow volume, and the reason might be related to the estimation in the kriging algorithm. We are not elaborating on that as interpolation algorithms are not the focuses of this study.

3.4.2 Snow-depth distribution within tree wells

The formation of tree wells is caused by varied snow melt rates that are driven by heterogeneity in surface energy inputs. In a forest both canopy interception and the snow-depth distribution in tree wells observed from the lidar data can be due to unsymmetrical energy inputs from the atmosphere and forests, wind redistribution, and creeping of the snowpack. In forested snow covered areas, longwave radiation varies the most at different canopy-cover conditions (Roth and Nolin, 2017). Consider the equation below,

$$L_{\downarrow} = v(\sigma_a \delta T_a^4) + (1 - v)(\sigma_c \delta T_c^4) \tag{3.8}$$

where σ_a and σ_c are the dimensionless effective emissivities for atmosphere and canopies; T_a and T_c are air temperature and canopy temperature; δ is the Stefan-Boltzmann constant ($5.67 \times 10^{-8} \text{W} \cdot \text{m}^{-2} \cdot \text{K}^{-1}$); v is the canopy openness, usually represented by the sky-view factor (SVF) for a sub-canopy location (Essery et al., 2008b). The SVF in the upslope direction from the tree bole will be much smaller than in the downslope direction assuming the tree bole is upright. Despite that the emissivity of trees is much higher than that of the atmosphere (Howard and Stull, 2013), the shortwave radiation absorbed by the canopy can heat up the tree leaves and tree boles (Lu et al., 2014; Webster et al., 2017), which makes T_c higher than T_a. Thus from Equation 3.8, the total longwave radiation that enters the snow surface in the upslope direction under canopy will be higher, which is consistent with the observed centers of mass of tree wells being downslope (Figure 3.5, 3.6). Considering the steepness of slopes, the SVF in the downslope direction should increase as slope becomes steeper (Seyednasrollah and Kumar, 2014). However, our observations are counter-intuitive, as the distance between the tree-well center of mass and tree bole (r_c) decreases as slope increases, which is likely

due to inaccurate slope estimation because it was estimated by averaging slopes at finer resolution within the study plot. The correlation analysis (Figure A.3) between the local slope at each canopy and r_c suggests that a steeper slope will result in more snow creep, which is a similar finding as was reported in Lu et al. (2014). We also retrieved the wind speed and wind direction data from the on-site met stations. We inspected the wind-direction distribution prior to the date that the lidar were scanned, and since the last snowfall. But the wind directions are random, which suggests the observed tree-well snow distribution was not affected by wind.

3.4.3 Canopy effects and canopy-terrain effects

The terrain slope affects the interactions between canopy and terrain on the snowpack. The outliers shown in Figure 3.6 indicated that the majority of outliers are on steeper slopes, which suggests that on steeper terrain, the terrain-canopy interactions will be less likely to explain any further snow-depth distribution of the tree well.

Intuitively, larger tree canopies seem to be able to make the tree wells larger and deeper. This can also be explained from the perspective of energy inputs. The tree height, crown area, and tree-bole diameters are highly correlated in common cases (Sumida et al., 2013). Therefore, the longwave radiation absorbed by the snow surface and emitted by the canopy and tree bole is usually higher when it is under a tree with larger crown area and at the same distance to the tree bole. From Figure 3.7a-c, we observed that both tree-well gradients and snow-depth standard deviation increase as the crown area increases. This can also be due to larger crown intercepting more snow during snowfall. As a result, the mean snow depths under larger canopies are usually shallower. However, Figure 3.7d is showing opposite trend comparing to other elevations, with snow depth being negatively correlated with the distance to the tree bole. This suggests there is no snow melt yet at the elevation above 2950 m because the temperature was so much lower and the total energy inputs was not enough to drive snow melt.

The tree-well gradients are found to be correlated with elevation (Table 3.2) in the Providence site but not in the other site, which can be attributable to several reasons. First, the precipitation is more often mixed rain and snow at lower elevations, which accelerates the snow melt both in the open and under canopy, and this can make the tree-well gradients less steep comparing to regions where precipitation is mostly snow. It can also be caused by the earlier snow melt in the lower elevation region. The met station at Upper Providence has the greatest degree-day value compared to others. Intuitively, the lower met station at Providence should have a higher degree-day value, with the inconsistent pattern attributed to the differences in microclimate and energy exchange (Safeeq and Hunsaker, 2016). The degree-day values (Table 3.4) indicate that Providence has an earlier snow melt and the gradient of incoming longwave radiation along elevation, which is also driving the variability in tree-well gradients distribution at this site, but not in others. From the snow-pillow measurements, we observed that the snow melt at Taramack Summit is less than 1/3 of that at Upper Providence and the snowpack at West Woodchuck Meadow did not melt at

all. Therefore, most of the change in snow depth at higher elevation sites are due to snow compaction, which is why tree-well gradients are not affected by the elevation at this site.

Table 3.4: Degree day and snow melt from 13 March to 23 March, 2010

	Lower Providence	Upper Providence	Lower Bull	Wolverton	TMR	Upper Bull	Panther	Shorthair	WWC
Degree day, °C	51.0	76.0	40.0	25.0	N/A	55.0	48.0	45.0	N/A
ΔSWE, cm	N/A	-9.6	N/A	N/A	-2.7	N/A	N/A	N/A	-0.3
Elevation, m	1753.0	1981.0	2195.0	2218.0	2300.0	2461.0	2618.0	2708.0	2773.0

We also experienced some difficulties in applying the newly parameterized variable, canopy-terrain shadow (CTS), in the XGBoost model. We compared the variable importance based on two metrics, number of regression tree nodes that use the variable to split, and the information gain from the variable. We observed that the CTS has the 4th most node splits but has the least information gain. These suggested the CTS that being derived from the current lidar data set has great uncertainties at such a fine scale. Also, we were only able to observe the trends by averaging snow depth in different aspects (Figure 3.5) or using the center-of-mass of all normalized tree-well snow depth (Figure 3.6). But these trends are not usable for finer scale snow-depth modeling. A more accurate canopy segmentation algorithm and higher point-density lidar might be helpful in reducing the uncertainties in these canopy-related variables at finer resolution and better modeling results can be expected if that can be implemented.

Another challenge related to the canopy effect is that some of the findings are based on the zonal statistics calculated from individual canopy covered area. Although we observed these zonal statistics to be strongly related to the snow distribution under the canopy, it is challenging to transform them into usable variables that can be integrated into pixel-based models. Transfer functions or some new canopy-related features need to be engineered so that these influences on snow can be accounted effectively and accurately.

3.4.4 Implications for water resources management

Understanding the details of how the snowpack interacts with canopy and terrain using actual dense measurements such as lidar is beneficial for improving spatially distributed hydrologic modeling that is based on mass-balance of water across a watershed. Considering that for most of the watersheds in the Sierra Nevada, and also some other regions in the world that rely on mountain snowpack as primary water supplies, streamflow predictions are heavily affected by the modeling of snow accumulation and melt. Thus, improving these interactions have great practical meanings in reducing variabilities in water resources management.

The trained regression model reached an R^2 of 0.71 at 0.5-m resolution. We can expect that resampling the 0.5-m results to a coarser resolution can make the R^2 even higher. Applying the trained model on the manipulated testing dataset, although the mean snow depth increases, it is limited by an increase of 3% as 50% of the forest were thinned, which suggests that forest thinning may not have great effect on increasing the total snow near

peak accumulation. But forest thinning could be useful for preserving the water supply by reducing the evapotranspiration from the canopy (Goulden et al., 2012). The performance of the model implies that similar machine-learning methods can be practical for spatial prediction tasks, or even spatio-temporal tasks when proper temporal features are available. On the other hand, training the machine-learning models is time-consuming and needs a great amount of training data. Gathering training data can be costly so one may want to balance the cost and benefit before pursuing the statistical approach for estimating snow depth for practical purposes. Since we found that removing a large portion of lidar points does not affect the final estimates of total snow volume, the detailed modeling at fine resolution may not be necessary for water management purposes as the needed information are all at larger scales. scales.

3.5 Conclusion

The tree-well snow surface can be observed from airborne lidar with average ground-point density higher than 1 $\text{pt} \cdot \text{m}^{-2}$. The point density also affects total snow-volume estimation from interpolated raster products. The effect of point density is more significant in densely forested areas than in less-densely forested areas because the undersampling of data points under canopy and oversampling of data points in the open and drip edge areas can offset the overestimation and underestimation when forest density is moderate. The tree-well snow-depth distribution depends on both topography and the tree above the snow surface, with the statistical analysis over the sampled study plots indicating that more snowpack were accumulated at the down slope direction from the tree bole under each tree, which can be caused by both snow creeping and the thermal radiation emitted by trees. Due to larger interception capacity and stronger thermal radiation from larger trees, the gradient of the tree well increases as the crown area increases. Tree wells with larger gradients are at lower elevations because of larger crown areas. Observed from the 0.5×0.5-m^2 resolution rasters, the snow depth was correlated with tree height, surrounding canopy coverage, tree-height standard deviation, and also crown volume. Both the topographic variables and vegetation variables are important in terms of predicting the snow depth spatially at different scales using the trained XGBoost model. From the simulated forest thinning experiments tested with the trained XGBoost model, we found that the effect of forest thinning on increasing snow volume near peak accumulation is limited thus is may not be a cost-effective approach for increasing water supply.

Chapter 4

Canopy effects on snow accumulation, an observational study from time-series data over three instrumented catchments

4.1 Introduction

The snowpack in California's Sierra Nevada has long been served as the primary water resources for agricultural and urban uses (Bales et al., 2006). For seasonal forecasts of flood peaks following the onset of snow melt, the estimation methods are turning from statistical estimates that use historical records to spatio-temporal water-balance estimates with integrated data sources (Zheng et al., 2018; Hopkinson et al., 2001). Quantifying the spatio-temporal distribution of snow accumulation allows more accurate forecast of snow melt and streamflow, but it is also a long-standing challenge in snow hydrology (Winstral and Marks, 2013; Golding and Swanson, 1986). In the high Sierras, orographic effect drives solid-phase precipitations falling over mid-to-high elevation regions, where most areas are covered with heterogeneous densities and different types of vegetation (Houze, 2012; Mott et al., 2014). During the snow accumulation period, the vegetation intercepts snowfall, causing snowpack distribute unevenly under canopy. As much as 60% of cumulative snowfall may be intercepted by forest in mid-winter and annual sublimation losses can be $30 - 40\%$ of annual snowfall (Hedstrom and Pomeroy, 1998). Being able to accurately quantify the canopy interception of snowfall is the foundation to estimate the total snow melt with higher accuracy and precision during the Spring season.

The canopy interception of snowfall can be quantified as the snow storage capacity of the canopy and interception efficiency (interception/snowfall). The snow storage capacity is the maximum amount of snowfall that can be intercepted by the canopy. It is determined by the leaf area, tree species, and initial canopy snow load (Storck et al., 2002). The inter-

ception efficiency is found to decrease with increasing snowfall, initial canopy snow load and temperature. It increases with increasing leaf-area index and canopy coverage (Hedstrom and Pomeroy, 1998; Schmidt and Gluns, 1991b).

The coniferous canopies interception on snowfall is difficult to measure and quantify. Previous studies designed special weighing devices such that the weight of the intercepted snow accumulated snow can be measured at the same time. The total snow interception is found to be correlated with the accumulated snowfall (Storck et al., 2002; Hedstrom and Pomeroy, 1998). Thus, several process models have incorporated this statistical finding and account canopy-cover effect on snow accumulation (Marks et al., 1999; Hellstrm, 2001; Bartelt and Lehning, 2002; Lehning et al., 2006).

To calculate canopy interception, using canopy metrics that are highly correlated with the total snow accumulations is a common solution. Retrieving canopy metrics has advanced in recent years. The technology has been advancing from the traditional plant canopy analyzer (Gower and Norman, 1991; Stenberg et al., 1994; Hellstrm, 2001; Sturm et al., 2001; Pomeroy et al., 2002), to hemispherical-view camera (Musselman et al., 2008; Sirpa et al., 2012), and recently, to lidar (Zheng and Moskal, 2009; Zheng et al., 2016). The plant canopy analyzer was commonly used for retrieving the LAI in the forest. By using the hemispherical-view camera, the pixels of the taken images can be classified as either canopy-cover or clear, thus the percentage of clear view for each zenith angle can be quantified as sky-view factor, which was also found to be a statistically significant predictors for parameterizing snowfall interception in the process models (Musselman et al., 2008, 2012). The point-cloud data collected using lidar can be used for reconstructing the 3-dimensional canopy structures if the point-cloud has enough density. Algorithms have been developed for deriving LAI from the lidar point clouds and it will be interested to develop new canopy metrics from lidar for quantifying the snowfall interception.

In addition to canopy-metric retrieval from lidar, the canopy effect can also be quantified by using statistical models, with dense spatial measurements of snow depth or snow water equivalent (SWE) (Musselman et al., 2012; Zheng et al., 2016). Most previous studies were conducted using lidar measurements, either airborne or terrestrial. Both the airborne and terrestrial lidar can provide dense spatial snow-depth measurements ($>$ 10pts/m). With extensive footprint provided by airborne lidar scans, the canopy effect on snowpack spatial distribution can be quantified with large samples. The terrestrial lidar has a much smaller footprint comparing to airborne lidar (Revuelto et al., 2015), however, it is able to provide multiple scans per season. Thus the temporal variation in canopy effects can also be determined.

One short-coming in using lidar is it lacks temporal completeness, especially during the precipitation season, when it is difficult to take measurements. Lidar requires clear sky condition to take measurements to prevent the laser pulse intensity from attenuating because of rain drops and snow flakes (Filgueira et al., 2017). A dense cluster of snow-depth sensors can compensate the weakness of lidar in terms of temporal consistency. Combining the vegetation structures derived from lidar measurements and continuous snow-depth measurements, there is potential that the spatial variation of snow accumulation can be

accurately quantified. In our study, we used long-term spatially dense snow measurements in the Sierra Nevada, together with the lidar-derived canopy metrics, to study the canopy effect on seasonal snow accumulations.

The general objective of the work reported here is to explore the possibility of studying the spatial variability of snow accumulation by using lidar-derived canopy metrics and clustered snow-depth sensor measurements. We address two major question. First, to what extent can one use lidar-derived canopy metrics to predict the snow accumulation spatially. Second, for all developed lidar-derived canopy metrics, what is the relative importance between them.

4.2 Method

4.2.1 Study areas and snow-depth sensor data

The study was conducted over three areas in the Sierra Nevada: Pinecrest in the Central Sierra, and Providence and Wolverton in the Southern Sierra (Figure 4.1(a)). For each study area, snow-depth sensors (Judd Communications) are instrumented and they are placed into clusters (Figure 4.1(b, c)), with topographic characteristics (elevation, aspect) varying between clusters and canopy-cover conditions varying within each cluster. Pinecrest is the lowest in elevation and also flat in terms of elevation gradient. The lower site of Providence has similar elevation range as Pinecrest and the upper site is 200-m higher. Wolverton is the highest of the three study areas, with elevation around 2200 m at the lower site and 2600 m at the upper site. The sensors in Pinecrest were installed in 2014 and the sensors in both Wolverton and Providence were installed back in 2008 (Table 4.1).

Table 4.1: Summary of data from the study sites

Site	Sub-site	Elevation, m	Data availability
Pinecrest	Upper	1808 - 1834	WY2014-WY2017
	Lower	1748 - 1778	WY2014-WY2017
Providence	Upper	1975-1984	WY2008-WY2016
	Lower	1730-1740	WY2008-WY2016
Wolverton	Site1	2225-2227	WY2008-WY2016
	Site2	2250-2266	WY2008-WY2016
	Site3	2590-2602	WY2008-WY2016
	Site4	2630-2648	WY2008-WY2016

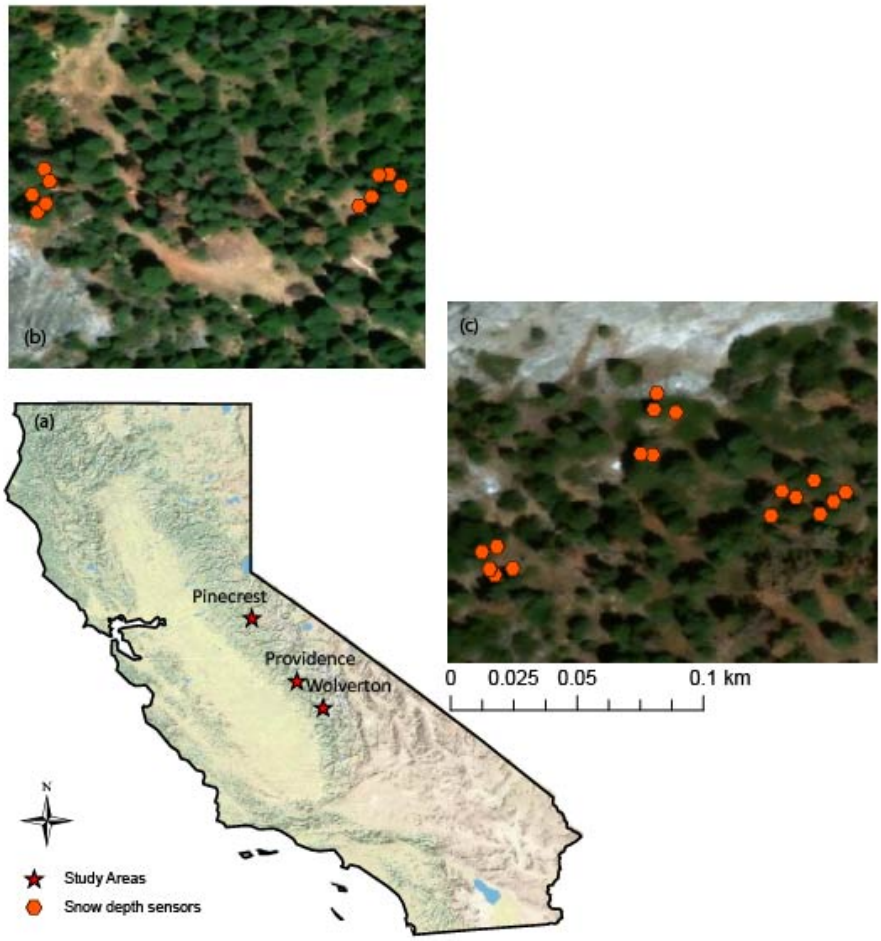

Figure 4.1: (a) The study areas locations in the Sierra Nevada. Snow-depth sensor locations around the (b) lower met stations and (c) upper met stations in the Providence site.

4.2.2 Lidar data

The point-cloud lidar data were used for generating raster data sets. The raw point-cloud files were divided into 250×250-m tiles using LAStools lidar processing software. We extracted the ground points from each tile and interpolated them into a 0.5-m resolution digital elevation model (DEM) by using a simple kriging model with a spherical covariance function. The 250×250-m DEM tiles were mosaicked together to form a single DEM of the study area. Digital surface model (DSM) were generated from all first returns of the lidar point cloud. DEM were subtracted from the DSM for producing canopy height model (CHM). Individual canopy was segmented out from the CHM using watershed segmentation algorithm implemented in SAGA GIS software. Over each snow-depth sensor location, canopy metrics such as canopy height mean, standard deviation, and canopy density were extracted at searching radius from 2 m to 40 m with 1-m increment. Also, the distance from the sensor location to

the closest tree canopy is also calculated.

4.2.3 Canonical-view images

The canonical-view images were taken below each individual sensor node, facing straight-up to the sky. The sky-view factors f at each individual zenith angle θ were derived from the raw image and the sky-view factor of the entire image is also estimated using the equation below,

$$f_{tot} = \frac{\int_{\theta=1}^{\theta=90} \sin(\theta) f(\theta)}{\int_{\theta=1}^{\theta=90} \sin(\theta)} \tag{4.1}$$

The sky-view factors data are available for Wolverton only. We included the total sky-view factor and the sky-view factors at each zenith angle as independent variables for modeling the snow accumulations observed using the snow-depth sensor data. The results are compared with the modeling using lidar data as independent variables, only over Wolverton.

4.2.4 Snow accumulation events detection

The snow-depth sensors reporting time ranges are shown in Table **??**. To study the canopy effect on snow accumulation, we extracted all events when snow accumulate in solid forms. The event extraction can be performed in the following procedure,

1. Get the moving average of each snow depth time-series with a window size of 2. Then calculate the 1st order gradient of time-series. This will make the following estimation avoid influence from the high frequency noise in the snow depth data.

2. The 1st order gradient over all sensors are used to calculate the x% quartile of the gradient. The quartile value was then compared with a pre-configured threshold to determine if most sensors observe snow accumulation. And the neighboring accumulating days are grouped together to form a single event.

3. Quartile thresholds for snow precipitation and melting events are different. We set the quartile for snow accumulation as 30%. It means that if 30% of sensors show an ascending trend in one day, we can classify this day as an accumulation day.

4. The gradient thresholds are also different for snow accumulation events. The optimized threshold for snow accumulation events is 0.1 cm. Three closed events can be combined into one events if they satisfy some requirements.

   For snow accumulation events, the optimized way to combine two neighboring events together is to first judge if the length of gaps between two events are shorter than one third of the sum of length of two events. Then, if the snow depth data in most sensors doesnt show a descending trend during the gap period, the two closed events can be combined into one.

4.2.5 Statistical analysis

All extracted accumulation events are used for statistical modeling with the features derived from the lidar data and the sky-view factors derived from the canonical-view camera images. We conducted regression analysis to study if canopy metrics can be used as predictors for estimating snow accumulating at various canopy-covered conditions. For each individual accumulation event, the total snow accumulation at each sensor node was estimated as $\Delta H = H_k - H_1$ where H_k is the snow-depth at the last time step and H_0 is the snow-depth at the initial time step. Considering the topographic effects on precipitation along the elevation gradient, we offset the total solid precipitation for each individual event at each site using topographic variables. The offset results are standardized to the range of $0 - 1$. The detrended target values are regressed using Elastic Net, which is a regularized regression method that linearly combines both $L1$ and $L2$ penalties in the regression model. Assuming we have a linear regression problem defined as,

$$y = X\beta + \varepsilon \tag{4.2}$$

where y is the target value and X is the matrix of all covariates. The estimates of the regression coefficients $\hat{\beta}$ is defined as,

$$\hat{\beta} = \arg\min_{\beta}(\|y - X\beta\|^2 + \lambda_2\|\beta\|^2 + \lambda_1\|\beta\|_1) \tag{4.3}$$

The Elastic Net was chosen than other regularized regression approaches for its ability of addressing correlated covariates and when the number of covariates is high. In our case, the canopy metrics can be highly correlated when the searching radii are close and the number of covariates included in our analysis is more than 100.

In order to have representative estimate of how much variability that can be explained by the Elastic Net model. We used bootstrap to resample the data for 20 iterations and we estimated the cross-validated coefficient of determination (R^2) within each iteration. The distribution of the R^2 can be estimated from multiple bootstrapping results.

We also applied correlation analysis to explore the most informative radius of lidar-derived canopy features and the most informative zenith angle of the sky-view factors from the canonical view images. We correlated the snow accumulation from each individual event with the Lidar-derived mean canopy height at various searching radii and at various zenith angles. The correlation coefficients Rs are compared at various radii and angles for selecting the optimal radius and zenith angle. Considering Pinecrest has a relatively short record, most of which is during the heavy drought of California, we did not conduct the analysis for Pinecrest. Also, camera images are not available for Providence thus we only radius dependency analysis at that site. For the data at Wolverton, we selected a few near-optimal searching radii and zenith angles. We used these selected variables and conducted a step-wise linear regression process for exploring the relative importance between variables.

4.3 Results

4.3.1 Snow accumulation events extracted from snow-depth time-series

We applied our snow accumulation events extraction algorithm on all snow-depth sensor clusters for all time periods when clean snow-depth data are available. The performance of the detection algorithm is similar to manual extraction that needs to be done by human. As is shown in Figure 4.2, the algorithm is able to detect most major snow accumulation periods. And the summary of accumulation events detected for each site is shown in Table 4.2 and the distribution of the magnitude of the accumulation at each study area is shown in Figure 4.3.

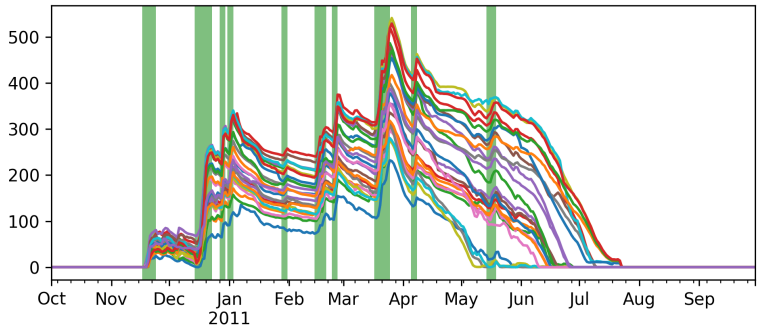

Figure 4.2: Snow accumulation events extracted using the accumulation detection algorithm, for Wolverton in 2011.

Table 4.2: Number of events detected for each water year from the three different study sites

Water Year	Providence	Wolverton	Pinecrest
2008	1	3	NaN
2009	6	8	NaN
2010	10	11	NaN
2011	7	10	NaN
2012	7	10	NaN
2013	7	5	NaN
2014	6	7	1
2015	5	8	3
2016	9	NaN	8
2017	NaN	NaN	8

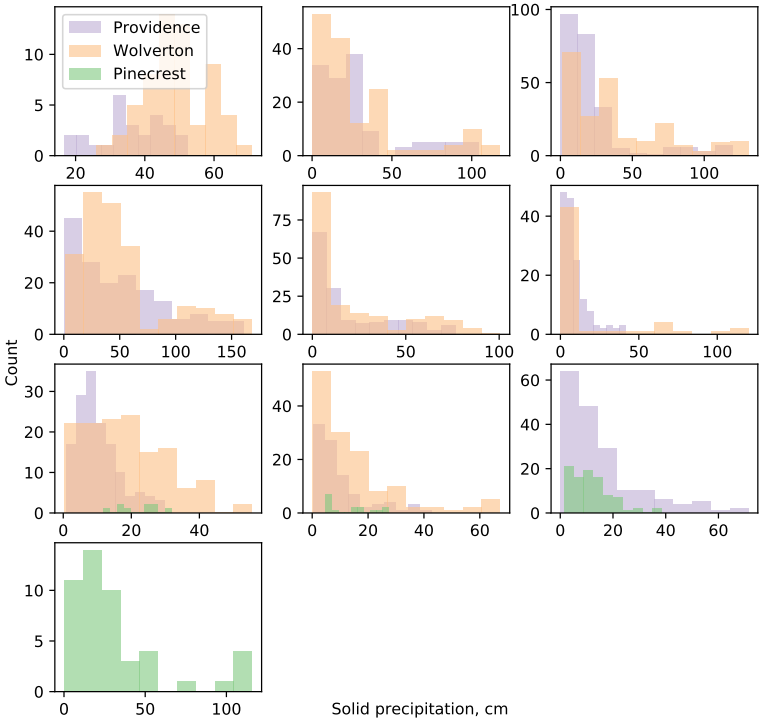

Figure 4.3: Solid-form precipitations distributions observed from three sites over 10 years

4.3.2 Statistical modeling results

The variability that the Elastic Net model can explain over the three sites are shown as in Figure 4.4. The uncertainty range of the variability that can be explained by the Elastic Net model is much larger for the Pinecrest analysis than the other two areas. And the average of the explained variability decreases as the elevation becomes higher.

At Providence and Wolverton, excluding the minor accumulation events ($\leq$ 15 cm) can significantly increase the variability that can be explained by the Elastic Net model, with more than 50% explained at Providence and 40%$-$50% explained at Wolverton. Due to the fact that for minor accumulation events the signal strengths are not significantly greater than the uncertainty range of the snow-depth sensors, including these data points will defect the performance of the Elastic Net model. At Wolverton, the spatial variability of snow accumulation can be explained reaches the maximum when the mean snow accumulation is between 15 cm and 30 cm. At Pinecrest, no particular trends can be observed as the amount of data points is limited. When including most of the data points, the variability explained

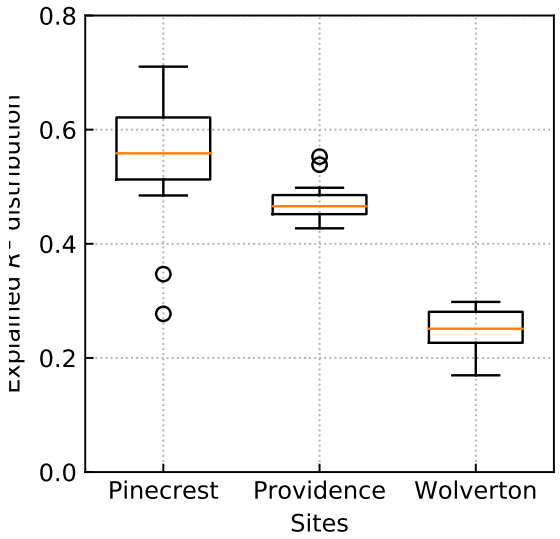

Figure 4.4: R^2 distribution over three sites

stabilized around 40%−60%.

Considering Wolverton is the only study area that both SVF and lidar are available and the trends observed in Figure 4.5. We constrained the valid mean precipitation in the range of 15−30 cm. We conducted three sets of analysis, including using lidar-derived canopy metrics as the predictors, using SVF as the predictors, and using both lidar and SVF as the predictors in the Elastic Net model. We did not observe much difference among the results from the three different sets of analysis. And the improvement of using both predictors is marginal (Figure 4.6).

The correlation analysis (Figure 4.7(a)) show that the surrounding canopies have a stronger effect on the snow accumulation on the ground than the canopy right above. The canopy mean height within 15-m radius at Providence is the most effect distance while the optimal radius is about 8 m at Wolverton. For sky-view factor, the optimal zenith angle is about 21° at Wolverton. In Figure 4.7(a), we identify each individual precipitation event by the transparency of each curve, from which we can see that heavier storms have more dominant weights on characterizing the canopy effects at different searching radii from Lidar data and zenith angles from canonical view imageries. In addition, the step-wise regression analysis conducted on the selected optimal variables of Lidar-derived and canonical view imagery features suggest that the canonical view imagery features are more important and the marginal information that Lidar provides is limited comparing to the first canonical view imagery feature selected (Figure 4.7(b)).

In addition, we compared the correlation coefficient between different types of lidar-derived canopy-related features and the snow accumulation over different sensor nodes. The features include mean canopy height over the searching radius, standard deviation of the

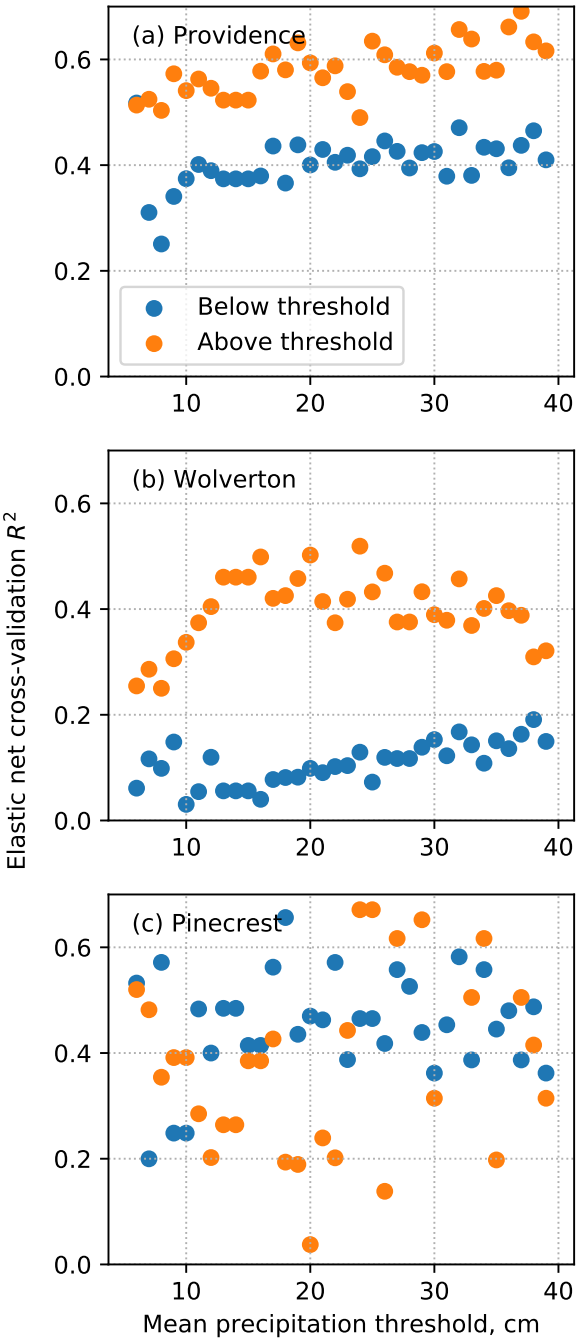

Figure 4.5: R^2 distribution over three sites vs. mean accumulation across sensors

height, maximum canopy height, and canopy coverage. As is shown in Figure 4.8, the amount of data points at Pinecrest is not enough to draw solid conclusions. At Providence and Wolverton, the correlation coefficient, is a concave shaped function of both canopy-

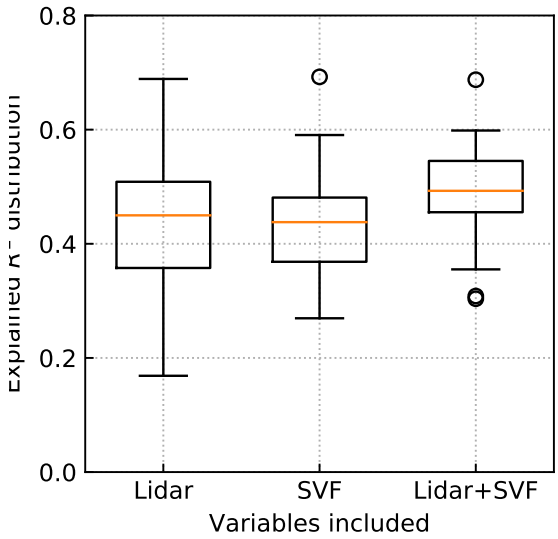

Figure 4.6: Explained variability over all sites using both lidar and SVF variables

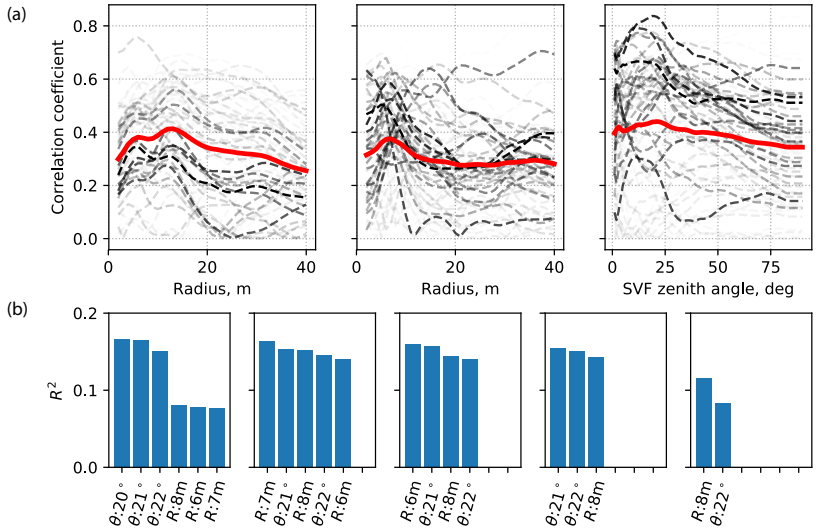

Figure 4.7: (a) Correlation coefficients estimated by correlating total snow accumulation of each event with canopy height and SVF at increment searching radii. (b) Coefficient of determination by step-wise regression analysis.

height mean and canopy coverage at various searching radii. The maximum canopy height at the smallest searching radius correlates the most with the snow accumulation. The standard deviations of the canopy heights at various searching radii show contrast trends at Providence and Wolverton.

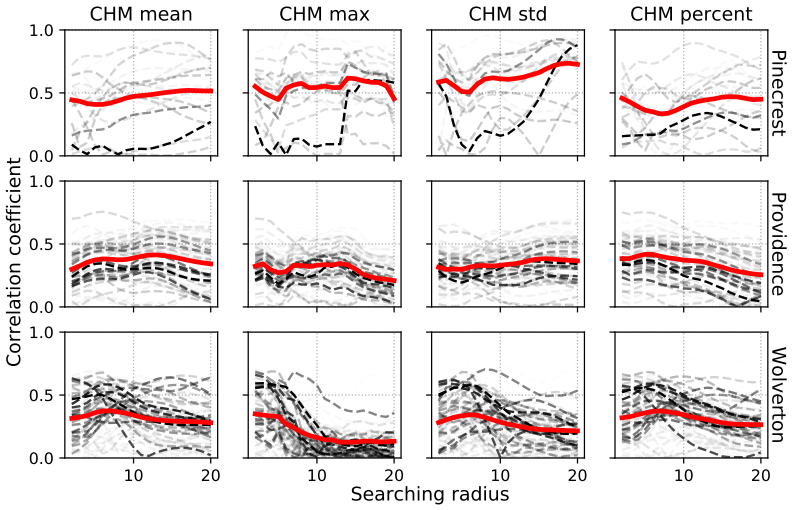

Figure 4.8: The correlation coefficient estimated between total snow accumulation of each event and lidar-derived canopy features at increment searching radii

4.4 Discussion

4.4.1 Canopy effects at different elevations

Among the three sites studied, the variability of snow accumulations that the canopy-related variables can explain vary from site to site and also depend on the mean cumulative precipitation over the entire event. The difference between sites can be attributable to different elevations as the canopy-cover density decreases as elevation increases and the solid phase precipitation increases with elevation. For example, the instrumentation locations at Pinecrest and Providence are at much lower elevations comparing to Wolverton. About 40% of snow-accumulation variability is attributable to the canopy effects at these two sites however only 25% can be explained over Wolverton. This suggests that at higher elevations, where precipitations are heavier, the canopy effects can be diluted by the heavy snowfall, which is similar to Schmidt and Gluns (1991b) has found, which stated that total interception of snowfall will saturate when the total precipitation reaches certain thresholds for different tree species. In addition, we observed some noise introduced by the low precipitation events in the regression analysis. Figure 4.5 suggests that the spatial variability of precipitation is less explainable by the canopy-related variables when the total precipitation is small.

4.4.2 Optimal variables characterizing canopy effects on snow accumulation

The canopy related variables derived from lidar and canonical-view images are compared. Based on Figure 4.6, the coefficient of determination calculated from 20 bootstrapping runs of predicting the snow accumulation suggests that the trained models are in lack stability in predicting the total snow accumulation at the unobserved sensor locations if using lidar-derived variables because the variability of the R^2 is larger than that using the sky-view factors. Also, the third box-plot of this figure suggests that the lidar-derived variables and sky-view factors are complementary and using both types variables can improve both R^2 and stability of prediction.

The snow-cover information is slightly more important than canopy metrics, including tree heights and tree-height standard deviations. This was verified by correlation coefficients in the regression analysis between snow accumulation and both tree height at increment searching radius and SVF at increment zenith angles. The SVFs are more correlated with snow accumulation than tree height in general. The step-wise regression analysis also suggested that sky-view factor at optimal zenith angle is more important than tree height at optimal searching radius. Although the tree height is an important metric characterizing trees in the forest but it does not necessarily represent the density and interception capacity of the canopy. Even sky-view factor only represents the canopy-cover condition at the lowest layer of canopy, it still explain partial variability in the interception capacity of the entire tree crown, which is the reason that it can be more important than lidar-derived canopy metrics.

Comparing within lidar-derived canopy metrics at increment radius, Figure 4.8 suggests that the most important canopy structures may not be the canopy layers right above the measured locations. The canopy surrounding within a few meters could be even more important as the interception capacity can be larger when the trees are clustered together than a single tree stand.

4.5 Conclusion

We found correlation between the lidar-derived canopy attribute and the snow accumulation extracted from the multi-year time-series snow-depth measurements. The correlation is stronger when the precipitation event has higher snow accumulation. And the correlation is also much stronger at a lower elevation because of denser vegetation. Although the lidar-derived canopy attributes are complementary to sky-view factor in explaining the snow-accumulation variability, the SVF is more important than lidar-derived variables when analyzing based on the step-wise regression. The canopy surrounding the snow surface within 8-m radius is more important than canopy structures within either smaller radius or larger radius, indicating clustered canopy effect is stronger than a single tree. The above findings suggest great potential of using lidar and ground measurements for studying canopy effect

on mountain snowpack.

Chapter 5

Spatial snow-water equivalent estimation using Wireless-sensor networks and remote sensing products

5.1 Introduction

In the state of California, ecosystem processes and water supplied for agricultural and urban uses depend on the snowpack in the Sierra Nevada as the primary source of spring and summer streamflow (Bales et al. (2006)). As the prediction of water availability and flood peaks depend in part on snowpack conditions, accurate knowledge of the snowpack can assist decision making for water resources management (California Department of Water Resources (2013)).

Current decision making for water management in California during the snowmelt season relies on ground measurements in the Sierra Nevada, which include continuous snow-pillow and snow-depth sensor measurements, and monthly manual snow surveys (Molotch and Bales (2005)). Ground stations are sparsely placed in the mountains compared to the spatial scale of each watershed. Therefore, the measurements may not be representative of physiographic features required to capture spatial variability of snow depth and snow water equivalent (SWE), either at the site or basin scale. Satellite-based remote sensing, such as MODIS and Landsat, has been used to map snow coverage at regional to global scales. However, they provide only pixel-wise fractional snow-coverage information, with no direct information on snow depth or SWE (Dozier et al. (2008); Molotch and Margulis (2008); Painter et al. (2009); Raleigh et al. (2013); Rittger et al. (2013); Rosenthal and Dozier (1996)). A modeled snow-data product that is commonly used in the Continental United States is the Snow Data Assimilation System (SNODAS), which integrates snow information from both satellite and ground stations, providing daily snow depth and snow water equivalent information at 1-km^2 resolution (Barrett (2003)). Recent work validating the SNODAS spatial product with lidar suggested that the performance of SNODAS in

the Tuolumne River basin is less accurate than 3-D ($x, y,$ elevation) bilinear interpolation of ground stations (Bair et al. (2016)).

Snow-coverage information and modeled spatial land-surface meteorological data can be used to back-integrate SWE from the snow melt-out date to the date of maximum SWE at the beginning of the snowmelt season. This technique has been applied across several mountain ranges and is referred to as the SWE-reconstruction technique (Bair et al. (2016); Guan et al. (2013); Margulis et al. (2016); Rittger (2012)). Although SWE reconstruction captures both temporal variability and spatial variability, it can only be done at the end of the season when the daily energy inputs and snow covered area are known (Cline et al. (1998)).

As a complement to satellite-based estimates of snow distribution, numerous statistical models have been developed to interpolate point-based snow information. Multivariate linear regression, commonly used in previous studies, can relate physiographic variables, historical SWE data, and snow covered area imagery with the observed SWE; and the accuracy is reasonably better than techniques such as inverse-distance weighting and simple kriging (Schneider and Molotch (2016); Fassnacht et al. (2003)). However, the linear-regression-based methods do not provide spatially smooth maps and the independent variables do not necessarily have a linear relationship with SWE (Zheng et al. (2016)). Other than regression, one category of methods that have shown promise are nearest-neighbor-based algorithms. These algorithms are attractive because they are easy to implement, nonparametric, learning based, and can learn linear and nonlinear trends in observations (Ni and Nguyen (2009)). Simulations and estimations at either fine temporal or spatial resolutions using parametric models can be computationally intensive. Nearest-neighbor approaches have therefore become an alternative solution to many problems in spatio-temporal modeling, not only for their advantage in time complexity, but also for their superior accuracy and ability to preserve patterns from observations. The k-NN algorithm has been used for multivariate time-series simulation for weather forecasting (Rajagopalan and Lall (1999)), disaggregating meteorological time-series data to finer time scales (Prairie et al. (2007); Kalra and Ahmad (2011)), and downscaling spatial climate-model data (Gangopadhyay and Clark (2005)). The k-NN algorithm was found to be superior in preserving the spatio-temporal covariability of the observation than multivariate autoregressive approaches.

To address the issues in presently available basin-scale water-balance data, a prototype real-time observation network that includes monitoring the snow conditions is being developed for the headwater areas of the American River basin in the Sierra Nevada (Zhang et al. (2017b)). The system enables combining ground measurements of snow depth and historical SWE reconstruction using a k-nearest neighbors (k-NN) algorithm for real-time spatial SWE estimation (Larose (2005)).

This work documents the k-nearest neighbors spatial-SWE-estimation method and evaluates the estimates against a spatial SWE product that is derived from lidar-measured snow depth. Three questions that motivated the present study are:

1. Does a k-NN approach for spatial SWE interpolation in mountainous regions provide

accurate SWE estimates relative to other products?

2. How is the error of the k-NN estimation distributed with regard to topographic variables?

3. Is it possible to further decrease the error of the k-NN estimates by distributing the residuals spatially?

5.2 Methods

We applied the k-nearest neighbors (k-NN) algorithm to estimate spatial snow water equivalent (SWE) in three basins in the Sierra Nevada, California, USA (Figure 5.1a, Table 5.1). The experiment for the American River basin focused on estimating the 2014 spatial SWE using 10 clusters of snow-depth measurements for 2014 from wireless-sensor networks, and historical SWE reconstructions based on MODIS from 2001 to 2013, aiming to evaluate the k-NN estimates temporally over the melt season. The SWE reconstructions were used by the algorithm for learning the SWE spatial distribution embedded in the data set. We did similar experiments in the Merced (2014) and Tuolumne (2014, 2016) basins using lidar-based SWE estimates to evaluate the k-NN results spatially. For these two basins, since we have fewer sensor networks deployed, we instead selected representative pixels as hypothetical sensor-network locations based on physiographic variables using a Gaussian-mixture model; and used these lidar-based SWE values for the k-NN experiments. In this setup we used historical SWE reconstructions, historical lidar-derived SWE, and historical SNODAS SWE as spatial training data to explore if different data sources matter. The spatial results over the two basins were evaluated using the lidar-derived SWE as a ground-truth data set.

Table 5.1: Topography summary of the three studied basins

Basin	Elevation range, m	Area, km^2 (above 1500-m elevation)
American	142−3070	2116
Tuolumne	408−3870	1136
Merced	1021−3927	853

5.2.1 American River basin analysis using wireless-sensor network data

The 10 wireless-sensor networks (Table 5.2) were deployed in the seasonally snow-covered region of the 5570 km^2 American basin (Figure 5.1b). Each network has ten or eleven sensor nodes (Figure 5.1c) that measure snow depth, temperature, relative humidity, soil moisture, and short-wave solar radiation (Zhang et al., 2017b; Brun-Laguna et al., 2016).

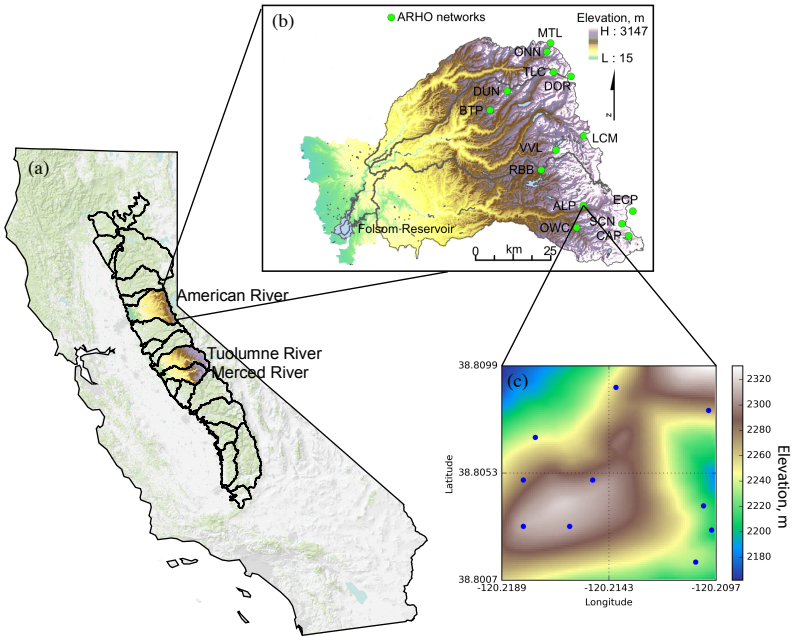

Figure 5.1: (a) The study areas of this research work are American River, Merced River and Tuolumne River basins that lie on the west side of the Sierra Nevada. (b) American River basin is instrumented with 14 wireless-sensor networks, which forms the American River Hydrologic Observatory (ARHO) (Zhang et al., 2017b). Please note the analysis in this study used 10 clusters' data. (c) Sensor locations of site Alpha in the Observatory, showing that the sensor locations of the network capture elevation gradient at the site.

The placements were strategically selected, aiming to capture snow depth and meteorological variability from elevation gradients, south versus north-facing slopes, steep versus flat areas, and various vegetation densities. All sensors take measurements at a 15-minute intervals, and the network manager of each sensor cluster forwards the data to a central webserver (Zhang et al., 2017b). Daily data averaged over each cluster were used in the current analysis.

5.2.2 Snow water equivalent reconstruction data

Snow water equivalent reconstruction is an existing data set that was produced by estimating historical spatial SWE for past snowmelt seasons (Guan et al., 2013; Molotch et al., 2017). The time extent of the SWE reconstructions is from 2000 to 2014 and the spatial extent covers the entire Sierra Nevada. The SWE-reconstruction method uses a snow-surface energy and mass-balance model:

$$M_p \rho L = S\downarrow(1-\alpha) + LW\downarrow + LW\uparrow + SH + LH \tag{5.1}$$

Table 5.2: Topographic Statistics of Sensor Clusters in the American River basin.

Cluster	Latitude	Longitude	Elevation, m	Slope, deg	Aspect, deg	Canopy Coverage, %
Alpha	38.80	-120.21	2319	2.7	181.1	55
Bear Trap	39.09	-120.58	1538	3.5	328.7	61
Caples Lake	38.71	-120.04	2430	4.1	220.6	20
Rice Creek*	39.15	-120.37	2024	7.0	246.6	30
Duncan Peak	39.15	-120.51	2111	10.4	264.3	42
Echo Peak	38.85	-120.07	2510	16.8	197.1	21
Lost Corner*	39.02	-120.21	2310	13.6	266.6	15
Mount Lincoln	39.29	-120.33	2405	8.1	194.4	2
Onion Creek	39.28	-120.36	1888	1.5	247.7	24
Owens Camp*	38.74	-120.24	1552	3.5	223.3	25
Robbs Saddle	38.91	-120.38	1828	3.5	107.9	32
Schneiders	38.75	-120.07	2694	9.9	293.3	42
Talbot Camp*	39.19	-120.38	1756	4.8	151.2	60
Vanvleck	38.94	-120.31	2023	2.7	202.8	48

* These sites were operational after the summer in 2014 so they were not included in the k-NN analysis.

where M_p(m) is the potential snowmelt (assuming full snow coverage), ρ(kg/m^3) is the liquid-water density, L(kJ/kg) is the latent heat of fusion, $S\downarrow$ (J/m^2) is the subcanopy insolation, α(unitless) is snow albedo, $LW\downarrow$ (J/m^2) is the downwelling longwave radiation, $LW\uparrow$ (J/m^2) is the longwave radiation emitted from the snowpack. SH(J/m^2) and LH(J/m^2) are sensible heat exchange and latent heat exchange accordingly. We need to note that the SWE-reconstruction model did not account for precipitation that occurs during the melt period, which may introduce bias in the estimates. The potential snowmelt M_p is scaled by the fractional snow-covered area (f_{SCA}) derived from MODIS to estimate the actual daily snowmelt,

$$M = M_p \times f_{SCA} \tag{5.2}$$

The time-series SWE for the season is calculated by back integrating the daily snowmelt since snow meltout:

$$\text{SWE}_0 = \text{SWE}_n + \sum_{j=1}^{n} M_j \tag{5.3}$$

where SWE_n is SWE at time step n, SWE_0 is the initial SWE, and M_j is the actual snowmelt during time step j. The initial SWE at each model pixel can be reconstructed at the time when snow disappearance observed from the satellite ($f_{SCA} = 0$):

$$\text{SWE}_0 = \sum_{j=1}^{n} M_j \text{ when } \text{SWE}_n = 0 \tag{5.4}$$

5.2.3 *k*-nearest-neighbor-based SWE estimation

A k-nearest neighbors algorithm was used to find the closest snowpack conditions in historical SWE reconstructions to real-time ground observations from the sensor networks data that are introduced in Section 5.2.1. The daily historical SWE reconstructions that were estimated for April 1st to August 31st for each year from 2001 to 2013, resulted in a dataset containing 1988 d-dimensional data points, where d is the number of independent variables, with each variable being a SWE value estimated from a spatially scaled ground measurement of snow depth. Before the execution of the k-NN algorithm, preprocessing was involved:

1. The ground measurements are of snow depth, whereas the SWE reconstructions are snow water equivalent. The conversion factor between the two is snow density. The spatial variation of snow water equivalent in the Sierra Nevada caused by snow density is small compared to the snow depth (Painter et al., 2016); and no spatial patterns in snow density were apparent in the 2014 data (Zhang et al., 2017b). In our model, the density value was estimated as the mean ratio of the co-located snow pillows and snow-depth sensors' measurements in the basin. We tested the relationships between the snow densities and terrain variables but did not find any. Therefore in further calculations we assumed that the snow density is uniform across the model spatial extent at each time step.

2. The spatial resolution (i.e. 500 m) of the SWE reconstructions is consistent with our model, however the sensor-network measurements are not. To make the sensor-network measurements consistent, we grouped the sensors bounded by the same SWE-reconstruction pixel and took their mean as the ground observation that is representative of the SWE-reconstruction pixel; these values were used in the k-NN algorithm. The grouped sensors were mapped to 49 SWE-reconstruction pixels. In this manner the multiple sensors within each 500-m pixel account for some of the sub-pixel variability found within the pixel. That said, the degree to which we sample the sub-grid variability cannot be explicitly determined. A detailed analysis of sub-pixel snow depth variability is beyond the scope of the current study.

3. Certain pixels in the SWE reconstructions that correspond to sensor-network measurements can be highly biased and inaccurate based on the comparison between 2014 sensor-network measurements and the SWE reconstructed for the same year. The bias has been found to affect the distance metric for the k-NN algorithm (Li et al., 2016; Liu et al., 2014). In order to filter out the biased and inaccurate SWE-reconstruction pixels, we calculated the correlation coefficient in time between each pair of ground measurements and SWE reconstructions during the 2014 snowmelt. A threshold (p-value ≤ 0.001) was used to decide if the pixel was retained: if the p-value exceeded the threshold then the ground measurements and SWE reconstructions for that pixel were excluded. Of the 49 pixels, 21 were retained after filtering; and the retained pixels' correlation matrices are shown in Figure 5.2. All pixel pairs show that the R^2s are above 0.5. A high temporal correlation between pixels suggests that the spatial patterns of SWE are consistent in time but with the basin-wide mean SWE changing over the season. This filtering step is not needed if the historical spatial data is from measurements like lidar.

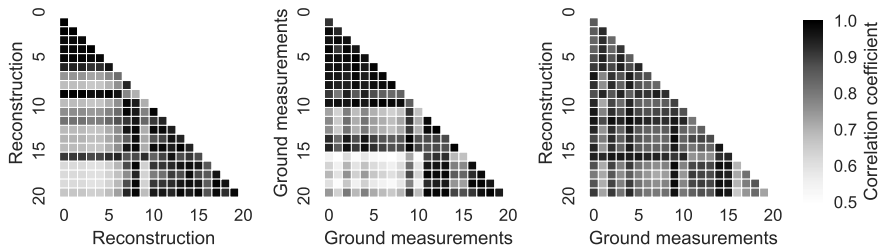

Figure 5.2: Lower triangle of correlation matrices of SWE reconstruction, ground measurements and correlation between the two for the American River basin, with autocorrelations excluded.

4. The default setting of a k-NN algorithm uses the Euclidean distance as a metric for comparing pair-wise distance between data points. The unique distribution and collinearity of a mountain snowpack's spatial distribution implies that using Euclidean distance might unevenly weight each dimension when calculating the distance (Figure 5.2). Therefore, we subtracted the mean from each variable and then used the Mahalanobis-distance metric to normalize the data by its covariance matrix,

$$d(\vec{x}_1, \vec{x}_2) = \sqrt{(\vec{x}_1 - \vec{x}_2)^T S^{-1} (\vec{x}_1 - \vec{x}_2)} \tag{5.5}$$

where $d(\vec{x}_1, \vec{x}_2)$ is the Mahalanobis distance between two vectors $\vec{x}_1$ and $\vec{x}_2$, S is the empirical covariance matrix. The ill-conditioned empirical covariance matrix was adjusted by adding a small number to all diagonal elements such that the covariance matrix will become full rank without losing much information and its inverse is computable after the adjustment.

5. In the k-nearest neighbors algorithm, we stored the filtered 21 pixel values from SWE reconstructions into a Balltree data structure (Cayton, 2009). The number of nearest neighbors to be searched was determined by a transformed leave-one-out cross-validation tuning scheme. A typical cross-validation scheme leaves out part of the samples as a testing set for evaluating the predictive model trained by the remaining samples (training set). In our task, we need to test if the method is adequate to estimate SWE spatially and holding out SWE reconstruction samples does not help evaluating the spatial predictive performance. Therefore, we left out one pixel in the training set and evaluated on it in validation; and by doing so we validated whether the method developed can estimate SWE at unobserved locations.

The 21 selected pixels' time series from the 2001-2013 SWE reconstructions were formated to the training data set and the corresponding snow-depth ground measurements from 2014 were converted to SWE and formated to the testing data set. We ran the k-NN algorithm using these formated data. The number of nearest neighbors (k) was chosen to

be 30 since the error calculated in the leave-one-out cross-validation did not significantly decrease when k became larger than 30.

5.2.4 Analysis using lidar data

The Merced-Tuolumne basins were surveyed by airborne lidar at sub-monthly temporal frequency during snowmelt by NASA's Airborne Snow Observatory (ASO). The surveyed areas have elevation ranges of 1021 to 3927 m in the Merced basin and 408 to 3871 m in the Tuolumne basin. ASO produces a 50-m resolution SWE product that is derived from lidar-measured snow-depth and modeled snow density (Painter et al., 2016). We used the ASO products from 2014 and 2016 (Table 5.3) to evaluate the k-NN estimation method spatially.

Table 5.3: Lidar survey dates in 2014 and 2016 at Merced and Tuolumne basins.

	2014	**2016**
Merced	03-24, 04-06, 04-14, 04-23, 04-29 05-03, 05-12	N/A
Tuolumne	03-23, 04-07, 04-13, 04-20, 04-28 05-02, 05-11, 05-17, 05-27, 05-31	04-01, 04-07, 04-16, 04-26, 05-27 06-07, 06-13, 06-20

ASO collected and processed lidar under the following standards: The raw lidar data were collected using a Riegl Q1560 airborne laser scanner to measure surface elevations. Snow-depth maps were calculated by subtracting snow-off gridded surfaces from snow-on gridded surfaces. The spatial resolution of the lidar snow-depth raster product is 3-m resolution and the snow-depth estimates have mean absolute errors of < 8 cm, with bias < 1 cm when compared with manually measured depths at the 15×15m scale (Painter et al., 2016). This 3-m snow-depth raster product was resampled to 50-m resolution to match the spatially distributed version of the snowcover energy and mass balance model resolution (ISNOBAL) (Marks et al., 1999). The resampled 50-m snow-depth data were then converted to SWE by multiplying by the spatial snow density estimated from the ISNOBAL model. Our k-NN simulations were based on the 50-m resolution SWE products. To enable simulating k-NN using lidar data, the ASO 50-m resolution SWE product was resampled again to 500-m resolution by averaging all 50-m grids inside the corresponding 500-m grid. The SWE estimates from the k-NN simulation were evaluated against the 500-m lidar product. The evaluation of the k-NN simulation was compared to an evaluation of SNODAS against the lidar data. SNODAS is an operational, spatial snow product. It produces a spatially distributed SWE estimates at 1-km resolution in near real time since 2004. SNODAS assimilates a physically based model with SNOTEL observations and remotely sensed snow-covered-area images (Barrett, 2003). Previous work suggests that SNODAS works well in environments that are geographically closer to the SNOTEL stations, and the accuracy decays as the distance increases (Clow et al., 2012). The snow-depth comparison results between SNODAS and lidar

in Colorado's Rocky Mountains show that the accuracy is reasonable in general (Hedrick et al., 2015; Schneider and Molotch, 2016). Therefore we used it as a SWE-estimation performance benchmark.

Since there are only 4 small sensor clusters deployed in the Merced and Tuolumne basins, and in order to conduct similar experiments as what we did in the American River basin, we used a Gaussian-mixture model to select physiographically representative locations and treated them as sensor-network instrumented locations. These locations' corresponding pixel values were extracted from the lidar-derived SWE maps and they were used as inputs in the k-NN algorithm for both basins. After running the k-NN algorithm, Gaussian-process regression was conducted to distribute residuals spatially across these two basins. In order to determine if the spatial SWE estimates perform better than a typical SWE product, the k-NN SWE estimates were compared to SNODAS.

As the spatial distribution of SWE is highly dependent on physiographic variables such as elevation, slope, aspect and vegetation (Zheng et al., 2016), the 3-m resolution digital elevation models (DEM) of both basins retrieved from the snow-off lidar measurements were resampled to 500-m resolution DEMs and were further processed to derive slope and aspect at 500-m resolution. A 30-m resolution National Land Cover Database 2011 (NLCD 2011) USFS Tree Canopy Analytical dataset was clipped, resampled, and georegistered to the same resolution and extent as the 500-m resolution DEMs. These 4 variables were combined with latitude and longitude to form a 6-dimensional vector (i.e., the combined $\mathbb{R}^6$, $\mathbf{x} = [x^{\text{latitude}}, x^{\text{longitude}}, x^{\text{elevation}}, x^{\text{slope}}, x^{\text{aspect}}, x^{\text{canopy}}]$). Selection of the most-representative locations for siting sensor networks was accomplished using a Gaussian mixture model (Oroza et al., 2016). The Gaussian mixture model is a parametric probability density function represented as a weighted sum of Gaussian component densities as given by the equation,

$$p(\mathbf{x}|\lambda) = \sum_{i=1}^{M} w_i \mathcal{N}(\mathbf{x}|\boldsymbol{\mu}_i, \boldsymbol{\Sigma}_i) \tag{5.6}$$

where w_i is the mixture weight and $g(\mathbf{x}|\boldsymbol{\mu}_i, \boldsymbol{\Sigma}_i)$ is the component Gaussian density for each Gaussian component. Each component density is a D-variate Gaussian function of the form,

$$\mathcal{N}(\mathbf{x}|\boldsymbol{\mu}_i, \boldsymbol{\Sigma}_i) = \frac{1}{(2\pi)^{D/2}|\boldsymbol{\Sigma}_i|^{1/2}} \exp\left\{-\frac{1}{2}(\mathbf{x} - \boldsymbol{\mu}_i)'\boldsymbol{\Sigma}_i^{-1}(\mathbf{x} - \boldsymbol{\mu}_i)\right\} \tag{5.7}$$

with mean vector $\boldsymbol{\mu}_i$ and covariance matrix $\boldsymbol{\Sigma}_i$. The mixture weights satisfy the constraint that $\sum_{i=1}^{M} w_i = 1$. The objective of the Gaussian mixture model is to maximize the likelihood function (5.8) by estimating the parameters using the Expectation Maximization (EM) algorithm.

$$p(X|\lambda) = \prod_{t=1}^{T} p(\mathbf{x}_t|\lambda) \tag{5.8}$$

where λ is the collection of parameters (i.e., $\lambda = \{w_i, \boldsymbol{\mu}_i, \boldsymbol{\Sigma}_i\} \quad i = 1, ..., M$).

The estimated mean vector of each Gaussian component is the expected 6-dimensional vector. Since the given set of data does not necessarily have a data point equal to this mean, the data point that has the smallest Euclidean distance to the estimated mean vector is selected as the sampling location.

The number of sampling locations needed is decided by the Akaike information criterion (AIC). AIC is a measure of the relative quality between statistical models that are fitted with the same given set of data. It offers a relative estimate of the information lost when a given model is used to represent a process that generates the given data. In doing so it addresses the trade-off between the model's goodness of fit and model complexity. For the Gaussian-mixture model, the parameter that differentiates between models is the number of Gaussian components (i.e., sampling locations in this case). By using the AIC equation,

$$\mathrm{AIC}(\lambda) = -2\ln\left(p(X|\lambda)\right) + 2d \tag{5.9}$$

where $p(X|\lambda)$ is the maximized likelihood and d is the number of Gaussian components, the integer value of d was selected as the number of sampling locations for which the corresponding model had the lowest AIC score.

The sensor-network locations selected were used to extract 500-m resolution lidar-derived SWE pixels. These pixels were used to simulate k-NN algorithm with historical SWE reconstructions (described in Section 5.2.3). The preprocessing steps were not applied because they are specific to the snow-depth sensor data. The k-NN estimated SWE maps were evaluated against the lidar-derived SWE map on a pixel-wise basis and the error statistics calculated. The error statistics used were root-mean-square error (RMSE),

$$\mathrm{RMSE} = \sqrt{\frac{1}{n}\sum_{i=1}^{n}(\hat{y}_i - y_i)^2} \tag{5.10}$$

and mean-absolute error (MAE),

$$\mathrm{MAE} = \frac{1}{n}\sum_{i=1}^{n}|\hat{y}_i - y_i| \tag{5.11}$$

where n is the number of pixels, $\hat{y}$ is the k-NN estimated pixel value and y is the lidar-derived pixel value.

5.2.5 Bias-correction on *k*-NN simulation using Gaussian process regression

The SWE-reconstruction product is inherently embedded with systematic bias because of (i) the inaccuracy to infer the final date of the seasonal snow cover from remote sensing; (ii) errors and coarse spatial scales of meteorological data; and (iii) weaknesses in the snow model used for SWE reconstructions (Slater et al., 2013). The k-NN interpolated SWE could be

biased because the spatial distribution of SWE depends on SWE reconstructions. To correct the bias inherited from SWE reconstructions, we calculated the k-NN estimation residuals for all sensor observed locations and the residuals were modeled using a Gaussian-process regression. The entire process of applying k-NN algorithm and Gaussian-process regression is called k-NN+GP in the following text.

Gaussian-process regression, the same as simple kriging in geostatistics, is a technique that has been extensively used in spatial inference. The regression relates the observation y to an underlying function $f(x)$ through a Gaussian noise model:

$$y = f(x) + \mathcal{N}(0, \sigma_n^2) \tag{5.12}$$

The essence of regression is the search for $f(x)$; in Gaussian process regression, what relates one observation to another is the *covariance function*, $k(x, x')$. For example, a popular choice of covariance function is the *squared exponential function*, and by folding the Gaussian noise into the covariance function, we have

$$k(x, x') = \sigma_f^2 \exp\left[\frac{-(x - x')^2}{2l^2}\right] + \sigma_n^2 \delta(x, x') \tag{5.13}$$

where σ_f^2 is the maximum allowable covariance, l is the length scale parameter of the covariance function, and $\delta(x, x')$ is the Kronecker delta function.

Since the key assumption in Gaussian-process modeling is that our data can be represented as a sample from a multivariate Gaussian distribution, we have

$$\begin{bmatrix} \mathbf{y} \\ y_* \end{bmatrix} = \mathcal{N}\left(\mathbf{0}, \begin{bmatrix} K & K_*^{\mathrm{T}} \\ K_* & K_{**} \end{bmatrix}\right) \tag{5.14}$$

where K, K_* and K_{**} can be summarized in the equations below.

$$K = \begin{bmatrix} k(x_1, x_1) & k(x_1, x_2) & \cdots & k(x_1, x_n) \\ k(x_2, x_1) & k(x_2, x_2) & \cdots & k(x_2, x_n) \\ \vdots & \vdots & \ddots & \vdots \\ k(x_n, x_1) & k(x_n, x_2) & \cdots & k(x_n, x_n) \end{bmatrix} \tag{5.15}$$

$$K_* = [k(x_*, x_1) \quad k(x_*, x_2) \quad \cdots k(x_*, x_n)] \tag{5.16}$$

$$K_{**} = k(x_*, x_*) \tag{5.17}$$

From the above equations,

$$y_* | \mathbf{y} \sim \mathcal{N}(K_* K^{-1} \mathbf{y}, K_{**} - K_* K^{-1} K_*^{\mathrm{T}}) \tag{5.18}$$

In doing the SWE residual interpolation, the independent variables $\mathbf{x}$ are the same as those being used in the Gaussian mixture model. The Matérn covariance function was used for its better prediction accuracy than other functions. The parameters in the covariance function were optimized with regards to SWE residuals at observed locations.

5.2.6 Using historical lidar scans and SNODAS as training data

Considering that the k-NN interpolation method for estimating spatial SWE can be used with any historical spatial SWE product, not just SWE reconstructions, we repeated the k-NN and k-NN+GP analysis for 2016 over the Tuolumne basin, but with all SWE reconstructions replaced with two different historical data sets, the 2014 lidar-derived SWE and the SWE estimated from SNODAS for the years of 2004−2015. In the setup with 2014 lidar data, only 10 scenes are included in the training set, which is only 0.5% of the number of historical SWE reconstructions. When running the k-NN algorithm we used $k = 1$ because we had a limited number of historical lidar scenes. The setup with SNODAS has 1461 scenes so we kept the same configuration as in the analysis using the SWE reconstructions. We compared these estimates based on the mean bias error (MBE), systematic root-mean-square error ($\mathrm{RMSE_s}$), unsystematic root-mean-square error ($\mathrm{RMSE_{us}}$) that are introduced in Willmott (1982).

5.3 Results

5.3.1 *k*-nearest neighbors plus Gaussian-process regression (*k*-NN+GP) using SWE reconstructions

Spatial estimates of American River SWE of three days around peak season in 2014 are shown in Figure 5.3. Snow accumulated across the high-elevation region of the basin during March and early April and the peak SWE is observed on April 5th. The snowpack melted quickly within two weeks. The SWE for most high-elevation regions are below 0.25 m and only the peak regions of the mountains have about 0.5 m of SWE, as is shown in the spatial SWE map estimated for the May 3rd. A comparison between ground observations and the k-NN estimates (Figure 5.4) suggests that the k-NN algorithm has low bias on a basin-wide scale, but can be highly biased for certain pixels. The bias is likely attributable to both error induced by upscaling ground measurements to 500-m resolution and the inherent bias in the SWE reconstructions as sensor-network measurements are more accurate than SWE reconstructions.

Although SWE reconstructions are not accurate estimates of SWE, it is still interesting to determine whether k-NN could be a technique for extrapolating the ground measurements across the basin. Figure 5.5 shows a time series comparison between ground observations, k-NN estimates, and SWE reconstructions at 3 selected 500-m-resolution pixels. The k-NN estimation for each pixel is evaluated using leave-one-out cross-validation. Comparing the k-NN estimates with ground observations, some pixels have low bias at all times, while most of the pixels differ somewhat throughout time series. We found that the bias does not depend on elevation (Figure A.6). The magnitude of error could be as large as 0.4 m for certain pixels. The SWE-reconstruction curve suggests that SWE reconstructions underestimate SWE at all locations during the entire snowmelt season and the magnitude of error can be

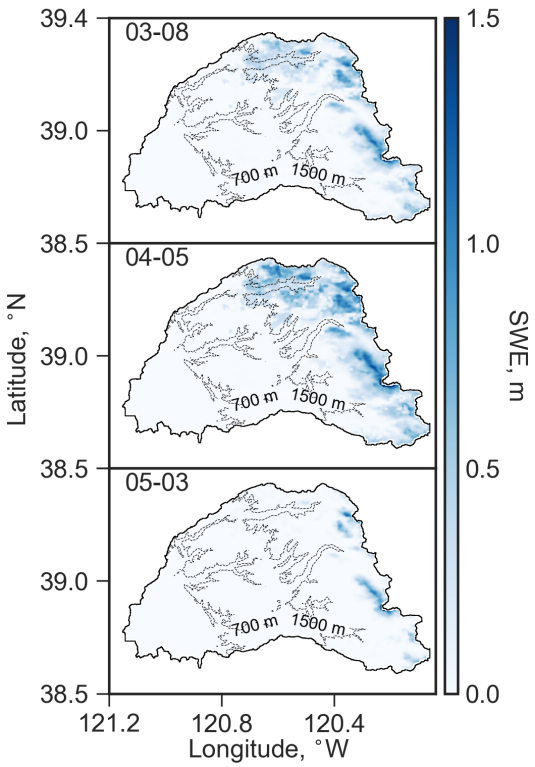

Figure 5.3: Snow water equivalent maps in the American River basin created using ground measurements and historical SWE-reconstruction data through k-NN algorithm. Bi-weekly maps are shown in Figure fig:c4s1.

as large as 0.8 m for certain pixels.

To evaluate the k-NN estimation in the Merced and Tuolumne basins, 24 locations in the Merced and 33 locations in the Tuolumne were selected using a Gaussian mixture model (Figure 5.6). Figure 5.7 shows a pixel-wise comparison of three estimation methods with the lidar-derived SWE. Point colors on the scatter plots represent the estimated Gaussian distribution kernel density of these data points over $\mathbb{R}^2$. The k-NN+GP estimation exhibits minimum bias relative to lidar (fitted linear regression line is closest to the 1:1 line in Figure 5.7 on the majority of days in both basins). Slopes and coefficients of determination presented in Figure 5.8 suggest the same. The RMSEs and MAEs of these estimation methods for each lidar date are shown as a time series, also in Figure 5.8. From these we observe that RMSEs and MAEs of the k-NN and the k-NN+GP estimates are smaller than SNODAS for the majority of days in 2016 over the Tuolumne basin. Both error statistics can be reduced as much as 10 cm during a normal snow season (2016). Similar results were observed from the analysis over the Merced basin in 2014. The estimated bias in reconstructed SWE starts to increase with elevation. The elevation-band-mean SWE estimated from k-NN has a maximum bias of -15 cm at elevations below 3000 m and +15 cm above 3000 m. k-

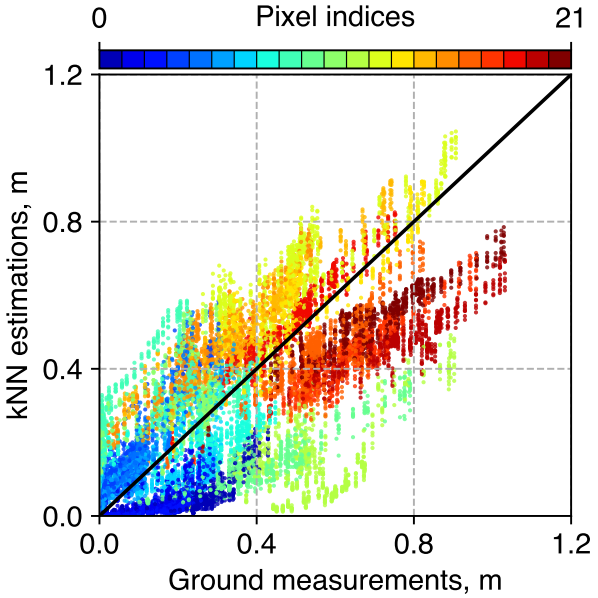

Figure 5.4: Scatter plot showing ground measurements and searched k-nearest neighbors at 21 locations (each location is a different color, referred as pixel index) in the American River basin. The estimations vs. measurements shows 1:1 trend overall; however, the relationship for each individual sensor is not necessarily 1:1 and the intercept for each may not be zero.

NN+GP can correct part of the bias over a few elevation bands. However, SNODAS has large underestimation bias for regions above 3000 m (Figure 5.9).

5.3.2 Estimation using historical lidar-derived SWE and SNODAS as training set

Although only 10 lidar-derived SWE maps produced in 2014 were included in the training set, the prediction SWE for 2016 is highly correlated with the SWE derived from lidar (correlation inferred from scatterplots and kernel densities in Figure 5.10). The detailed statistics (Table 5.4) reinforce that by showing that R^2s are in the range of $0.82-0.87$ for these four days. Also, both RMSEs and MAEs estimated using lidar-derived SWE are at least 10 cm less than that using SWE reconstructions. Also, the systematic error decreases drastically when GP is used. The only drawback we found from this experiment is that the slopes of the scatter plots decrease as the season approaches to the end. The MBEs suggest that the basin-wide mean SWE is unbiased if using SNODAS SWE as training data but the R^2s suggest it can only explain $40-50\%$ of the variability (Table 5.4).

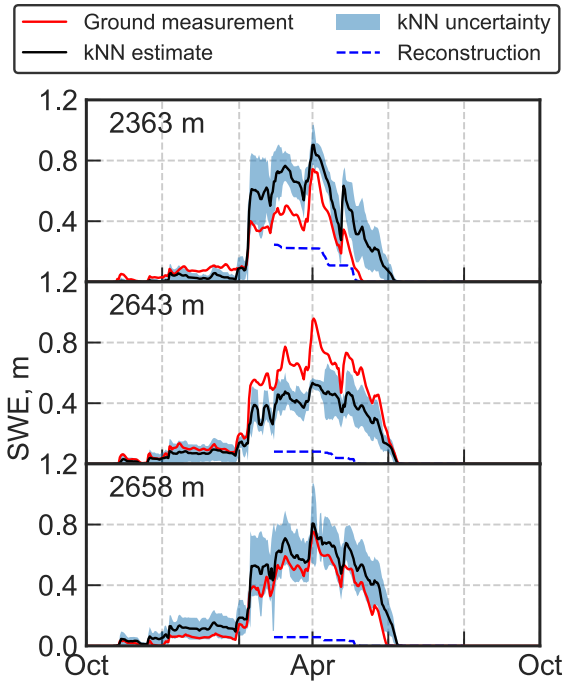

Figure 5.5: Daily snow water equivalent time series from the ground measurements, k-NN estimations, and SWE reconstructions at 3 selected pixels, in the American River basin for the 2014 water year. See Figure A.6 for 20 locations sorted by elevations.

5.3.3 k-NN estimation accuracy versus number of SWE-reconstruction scenes

The performance of a statistical prediction model depends in part on the size of the training data set, as verified in computer vision and machine learning research (Zhu et al., 2016). This finding agrees with our intuition to include as many SWE-reconstruction scenes as possible in the data set used to train the nearest neighbors algorithm. Since each SWE-reconstruction scene is embedded with a unique spatial distribution of snow water equivalent, the estimation accuracy should be improved as long as more scenes are stored. In other words, the k-NN algorithm will have a higher probability of finding closer neighbors when more scenes are included in the training set.

We verified this hypothesis by randomly selecting SWE-reconstruction scenes and increasing the number of scenes incrementally in our training set from 10% to 100% of the total number of scenes available (rounding up the percent scene numbers to the closest integer if needed). We compared the k-NN estimation results with the 500-m lidar-derived SWE from the Tuolumne basin, using RMSEs as error statistics representing estimation performance. RMSEs decrease when more SWE-reconstruction scenes are included in the training set for most days simulated for the Tuolumne basin (Figure 5.11). Similar patterns were observed when running the same experiment on the American-River-basin wireless-

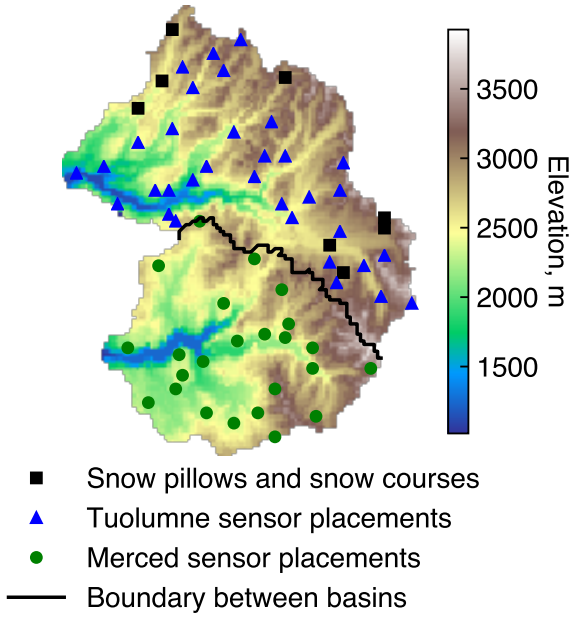

Figure 5.6: Snow pillows, snow courses, and selected simulation sensor locations at Merced and Tuolumne basins.

sensor-network data (Figure 5.12), in which the cross-validation RMSEs are shown because a lidar evaluation set is not available. Both figures imply that in general the decrease of the RMSEs tends to become saturated when the training set has more than 50% of all SWE reconstructions, suggesting 1000 SWE reconstructions are sufficient for capturing spatial SWE variability. There is also case when RMSEs are not sensitive to the number of SWE reconstructions (April 23rd, 2014, Figure fig:c4s4), when lidar data was collected immediately following a storm. The SWE-reconstruction model did not include the melting season precipitation events in the surface energy and mass balance calculation, which could explain why the k-NN results estimated for post-precipitation days were insensitive to the number of SWE-reconstruction scenes.

5.4 Discussion

5.4.1 Importance of ground measurements

The American River basin wireless-sensor networks provided unprecedented spatially distributed snowpack observations. The spatio-temporal data allow us to evaluate existing spatial SWE products and enable real-time spatial SWE estimation. The comparison between the sensor-network observations and SWE reconstructions over time (Figure 5.5, S2) suggests that the SWE reconstructions we are using are biased over the sensor locations.

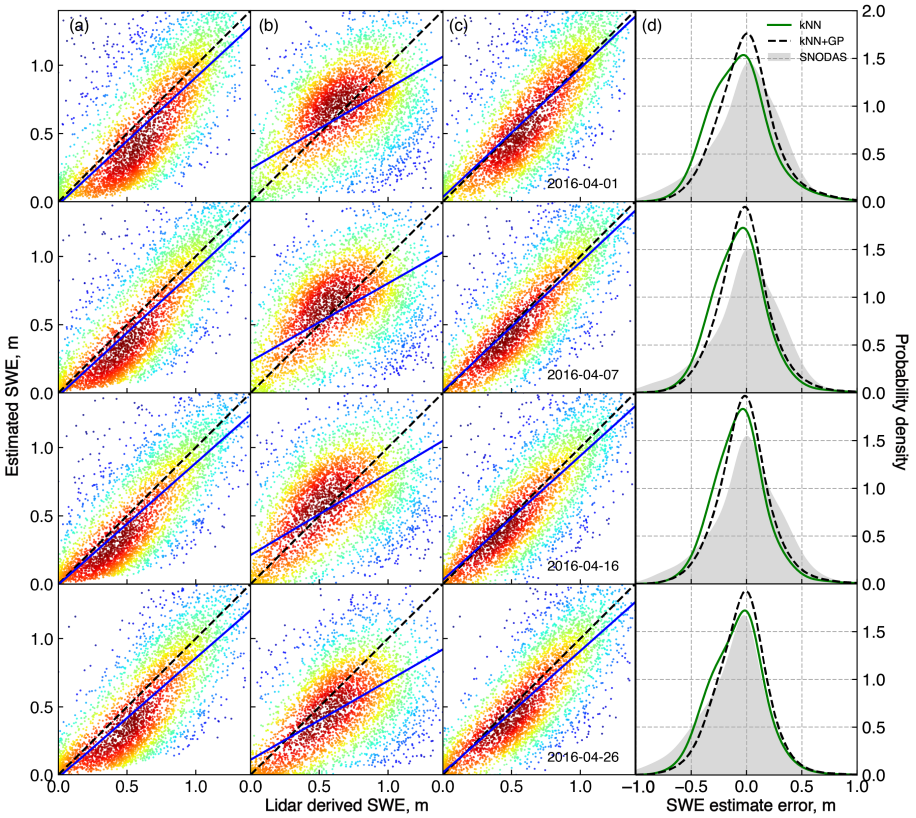

Figure 5.7: (a) k-NN (b) SNODAS and (c) k-NN+GP estimated snow water equivalent versus lidar derived snow water equivalent on four dates during the peak season in 2016 at the Tuolumne River basin, with color showing the point density (red is high density and blue is low density). (d) Snow water equivalent estimation error distribution shows that k-NN+GP is the best spatial estimation method.

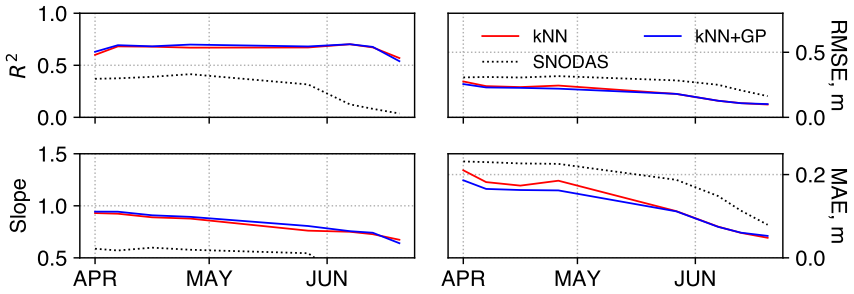

Figure 5.8: Slopes and coefficients of determination estimated from linear regressions between SWE estimations vs. lidar, RMSE and MAE of SWE estimations and lidar at Tuolumne basin in 2016. Statistics for other years and basins are shown in Figure fig:c4s3.

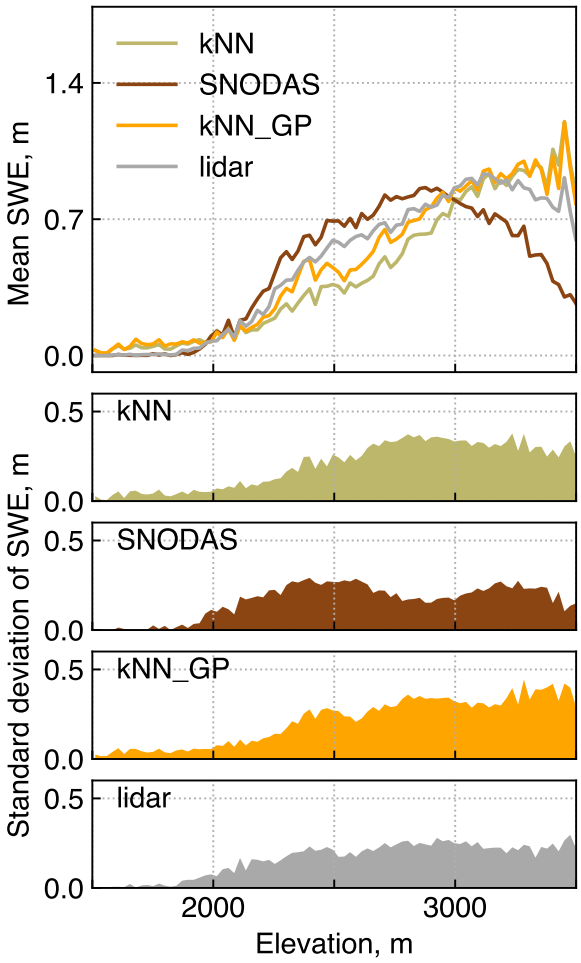

Figure 5.9: The Tuolumne basin's snow water equivalent mean and standard deviation along the elevation gradient.

However, the bias was reduced in the k-NN estimates that used SWE reconstructions as training data. This emphasizes that accurate and spatially distributed ground measurements are important for correcting the error when the historical training data are biased. The more ground measurement locations we have, the less error that the k-NN estimates would have, even though it is used with a biased training data set (Figure S5).

The ground measurements are also important for residual distribution. Although the ground measurements used in the Tuolumne-Merced experiment were simulated from the lidar products, the results that are shown in Table 5.4 suggest that spatially dense and representative ground measurements are important when systematic bias exist in the training data and non-removable from the k-NN method. The bias in the k-NN estimates can be corrected systematically with a Gaussian process regression model trained from the residuals

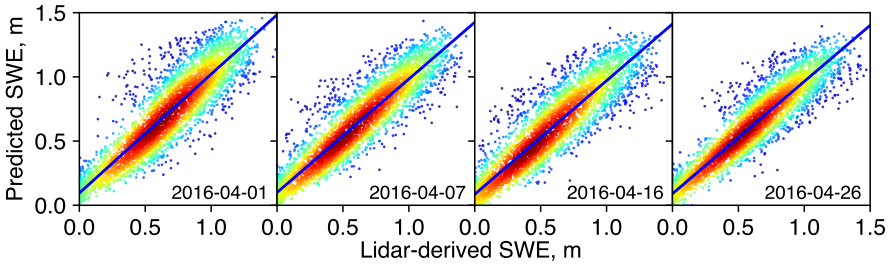

Figure 5.10: k-NN+GP estimated snow water equivalent versus lidar derived snow water equivalent on four dates during the peak season in 2016 at Tuolumne River basin, using the 2014 lidar-derived SWE as training set, with color showing the point density (red is high density and blue is low density).

Table 5.4: Statistics estimated from predicted SWE and lidar-derived SWE using historical lidar and SNODAS as training set.

Date	Training Data	+GP	MAE, m	MBE, m	RMSE, m	$RMSE_s$, m	$RMSE_{us}$, m	Slope	R^2
2016-04-01	SNODAS		0.24	-0.08	0.31	0.15	0.27	0.61	0.37
		✓	0.20	**-0.02**	0.26	0.09	0.24	0.73	0.51
	lidar		0.43	0.43	0.48	0.48	0.05	0.34	**0.82**
		✓	**0.11**	-0.05	**0.15**	0.05	0.14	**0.93**	**0.82**
2016-04-07	SNODAS		0.23	0.03	0.30	0.17	0.24	0.51	0.36
		✓	0.22	**0.02**	0.29	0.16	0.24	0.54	0.39
	lidar		0.38	0.38	0.45	0.45	0.04	0.33	**0.89**
		✓	**0.10**	-0.03	**0.14**	0.05	0.13	**0.88**	0.85
2016-04-16	SNODAS		0.23	0.07	0.31	0.19	0.24	0.49	0.34
		✓	0.20	0.04	0.27	0.14	0.23	0.62	0.48
	lidar		0.34	0.34	0.42	0.42	0.04	0.34	**0.89**
		✓	**0.11**	**-0.02**	**0.15**	0.05	0.14	**0.88**	0.84
2016-04-26	SNODAS		0.22	0.09	0.30	0.19	0.23	0.52	0.39
		✓	0.21	0.08	0.28	0.17	0.22	0.56	0.43
	lidar		0.37	0.37	0.44	0.44	0.03	0.34	**0.92**
		✓	**0.09**	**-0.02**	**0.13**	0.05	0.12	**0.87**	0.87

MBE: mean-bias error
$RMSE_s$: systematic root-mean-square error
$RMSE_{us}$: unsystematic root-mean-square error

over the ground measurement locations.

The importance of the ground measurements is also relative to the quality of the historical training data. Comparing the analysis from using SWE reconstructions versus lidar, we believe there is a trade-off between the quality of the historical training data and the amount of ground measurements that are needed. With more lidar scans or more accurate historical SWE products available, we may not need to have that many sensor locations for accurate k-NN estimates and the residual distribution procedure may not be needed.

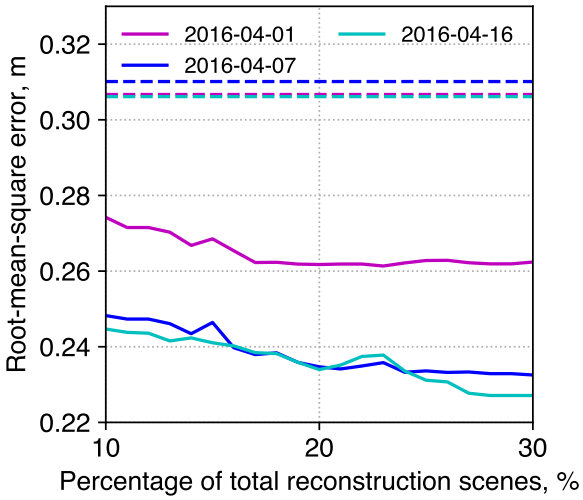

Figure 5.11: Solid lines are root-mean-square error versus the percentage of total number of SWE-reconstruction scenes (1988 scenes) that were included in the k-NN method. The errors are estimated from the results of the analysis for the 2016 Tuolumne basin data. The dashed lines are the errors of SNODAS at the same dates, which are used as baselines of prediction performance. The RMSEs decrease saturates around 30% of total number of SWE-reconstruction scenes. RMSEs and MAEs for more days in 2014 for the Merced basin are shown in Figure fig:c4s4.

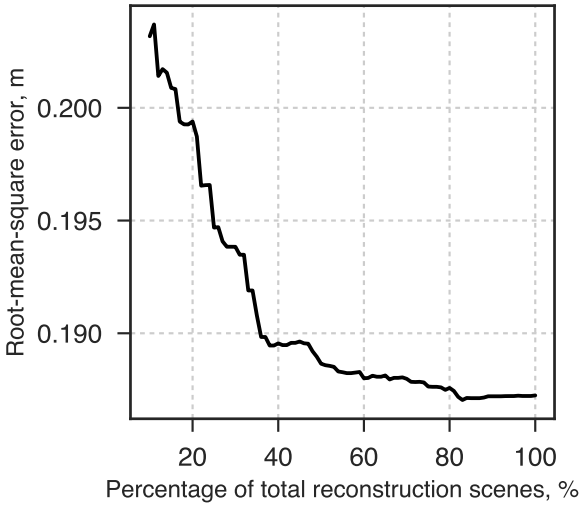

Figure 5.12: Root-mean-square error versus the percentage of total number of SWE-reconstruction scenes (1988 scenes) that were included in the k-NN method. The errors are estimated from the results of the analysis for the 2014 American River basin data.

5.4.2 Bias and uncertainties in the *k*-NN SWE estimates

In general, the k-NN approach intrinsically preserves the autocorrelation structure of the spatial SWE, which was also found and reported in other applications of the k-NN method (Gangopadhyay and Clark, 2005; Prairie et al., 2007). These studies also found that the k-NN method does not fully preserve the temporal autocorrelation structure, which was not observed in our results (not shown) and the finding can be specific to particular applications. The unexplained spatial variabilities are mostly due to the bias and inaccuracies of the historical training data, which can be decomposed into the following aspects:

1. As was discussed in Section 5.2.5, multiple error sources can contribute to the bias in SWE reconstructions; and thus affect the estimation accuracy of the k-NN interpolation method. Since we can use a Gaussian-process regression model to correct the bias in the k-NN SWE estimates, the bias is likely due to physiographic features affecting the SWE reconstructions.

2. The MODIS f_{SCA}, which was the basic of the SWE-reconstruction products that we used, was derived using the method in Painter et al. (2009). The local zenith for f_{SCA} can be significantly affected by the subpixel topographic variability, which can cause errors in the estimate of both fractional snow cover and derived snow properties. In densely vegetated area, quantifying fractional snow cover is beyond our capacity of using MODIS and we may only detect snow's presence or absence, which contributes uncertainties in SWE reconstructions over forested areas, with the bias accumulating throughout the entire modeling season (Raleigh et al., 2013). Also, MODIS has the detection capacity down to $10-15\%$ of fractional snow covered area; and thus the inferred final date of seasonal from MODIS snow coverage can be earlier than the actual melt-out date (Painter et al., 2009; Liu et al., 2008; Rice et al., 2011).

3. Other than the snow-covered-area images, errors can also be caused by the spatial meteorological data that are used for estimating the heat flux that drives the snowmelt. These data have a much larger spatial scale than the SWE-reconstruction model, and downscaling is often performed by predicting values at the smaller scale using a statistical model that takes topographic variables as predicting features. Since the model is trained using the coarser-scale data, applying the model at a different scale, especially a smaller scale can cause errors in the estimates (Hostetler, 1994; Fowler and Wilby, 2007).

4. In addition to these snowmelt estimation errors in most SWE reconstructions, the SWE-reconstruction model used in this study does not capture precipitation events during the melt season (Guan et al., 2013). Warm winds usually come with rain-on-snow events and they can drive snowpack to melt faster by altering the energy balance (Garvelmann et al., 2014) and it is more likely to happen in the rain-snow transition zones ($1500-2000$ m in elevation) in the Sierra Nevada (Lundquist et al., 2008). Not considering precipitation events can greatly affect the accuracy of the estimated snow distributions at different elevation ranges.

Comparing to the analysis using the SWE reconstructions, the accuracy of the estimates using historical lidar as training set improved significantly (Figure 5.10). Most reported error

statistics (Table 5.4) were greatly reduced in the k-NN estimates if the GP was applied. This suggests that the GP model is effective on correcting the systematic errors in the k-NN estimation. Erratically, the coefficients of determination (R^2s) are generally greater in the k-NN estimates that are without the GP corrections comparing to these with the GP corrections, suggesting that the spatial distribution of SWE is stationary, such that the real-time SWE distribution can be accurately quantified by blending the real-time ground measurements and historical lidar scans.

The uncertainties of the estimates that use SNODAS as training data are much greater than that using either lidar or SWE reconstructions. The statistics of the k-NN analysis suggest that the historical SNODAS SWE estimates cannot capture the spatial pattern of the SWE distribution.The GP does not boost the performance, as observed in the analysis using historical lidar as training data, which suggests that the residuals cannot be related with the physiographic variables and most of the errors are unsystematic and are difficult to be corrected.

Comparing to linear-regression-based interpolation methods, the RMSEs of the SWE estimates from k-NN+GP that uses historical lidar as training set are all below 15 cm, which are similar to the errors reported in Fassnacht et al. (2003). We need to notice that the errors reported in our study could be more credible because the results are evaluated with a spatial data set, while previous studies only reported cross-validation errors. Also, most previous interpolation studies use SNOTEL data in the Rocky Mountains as ground observations, which can be biased training samples of the studied area because the SNOTEL sites in the Rocky Mountains can overestimate surrounding SWE by up to 200% (Molotch and Bales, 2005). Considering that the total snow accumulation in the 2016 water year is about the average of the long-term historical records, an acceptable spatio-temporal SWE estimation should have RMSEs below 20 cm.

5.4.3 Potential of the k-NN SWE estimation approach

Considering that SWE reconstructions can capture the spatial patterns of SWE, plus the high density of scenes available for these daily data, it can be an adequate data set to use with the k-NN method even though SWE reconstructions underperform in estimating the absolute magnitude of SWE. However, the experiment introduced in Section 5.2.6 and 5.3.2 suggests that the k-NN approach does not have to be limited to using SWE reconstructions as the training set, and any improvements that lead to better SWE distribution estimates can help in advancing the k-NN estimates. Other time series of historical spatial SWE data can be used as the training set, these include:

1. A more-accurate SWE-reconstruction data set produced by finer-resolution meteorological data and better f_{SCA} product processed by a more-advanced snow-coverage-mapping algorithm.

2. A new archive of lidar-derived SWE maps. We observed a performance boost with using only 10 scenes of historical lidar instead of historical SWE reconstructions. Although

those scenes were collected during the recent drought, we can see they are able to help predict spatial SWE in a normal SWE year. It will be also interesting to see how much more the k-NN approach can be improved when we have a longer series of lidar-derived SWE maps.

3. A new satellite-based SWE mapping product. We envision that in the future there will be lidar systems helping to map the land surface from the space, in real time. Considering they can be easily affected by cloud cover, we can apply the k-NN method with their historical record to fill in the gap and better serve real-time water-resources decision making.

We summarized the existing spatial SWE products for the Sierra Nevada that were introduced in previous studies and can be used for studying the spatial distribution of SWE in mountainous area (Table 5.5). The information provided in these data sets are worth studying for their rich content of spatio-temporal distribution of SWE, which can potentially motivate new techniques being developed for real-time spatial SWE estimation and water-resources decision making. Also, with similar techniques as k-NN, the number of real-time lidar flights can be greatly reduced during the winter season and thus reduce the financial cost to water agencies. With changes in global climate and increased variability of regional climate in the mountains, it requires having techniques that are data driven and model assisted, like the k-NN approach, for providing more-accurate and timely spatial SWE estimates. Thus more-precise and efficient water-resources management can be achieved for coping with the future challenges.

Table 5.5: Spatial SWE products information

Type	Resolution	Year range	Remote-sensing data source	Literature
Reanalysis	100 m	1985-2015	Landsat	Margulis et al. (2016)
Reconstruction	500 m	2000-2016	MODIS	Dozier et al. (2016)
Reconstruction	500 m	2000-2016	MODIS	Rittger et al. (2016)
Regression	5 km	1950-2003 (1 April only)	N/A	Howat and Tulaczyk (2005)
Reanalysis	1/16 deg	1915-2011	N/A	Livneh et al. (2013)

5.5 Conclusion

k-NN and k-NN+GP are effective approaches to blend ground-measured snowpack and remotely sensed snow-coverage information to estimate spatial snow water equivalent. The k-NN approach, using spatially representative snow-depth sensor data, built on historical spatial SWE estimates, can provide a near-real-time spatial estimate of SWE. The residual-distribution analysis using the Gaussian-process model indicated that the estimation errors from the k-NN method depend on the topography of each modeled pixel. By using the Gaussian-process model to distribute the errors spatially, estimation errors can be reduced

by about 5−10% during the peak season. The k-NN and k-NN+GP simulation results using lidar data from the Merced and Tuolumne basins reached $R^2 = 0.7$ for most modeled days during a normal snow season in 2016, with RMSEs < 15 cm (< 25 cm) and MAEs < 10 cm (< 20 cm) in 2014 (2016). The comparison with SNODAS indicates that these two approaches are able to provide a more-accurate estimation, regardless of climate conditions (2014 is a drought year; 2016 is a normal year). The decreasing RMSE with increasing number of SWE reconstructions suggests that the more historical information in a training set, the better quality the k-NN can achieve. The k-NN method can also be significantly improved as more-accurate historical spatial-SWE products, such as lidar snow-depth products, become available.

Chapter 6

Conclusions

Lidar, as a maturing measurement technology in remote sensing, is found to be useful in providing snow-depth mapping information across different scales for mountainous areas.

At fine scales, we are able to use lidar to map snow depth at sub-meter resolution, from which we are able to observe detailed snow-depth patterns both in open areas and under canopies. Other than the orographic effect on snow accumulation and snow-depth distribution, we also observed that snow-depth distributions depend on other topographic attributes such as slope, aspect, and northness, which is likely to be caused by energy variation over different slope-facing terrains, e.g. south-facing surfaces receive stronger solar radiation over those with north aspect. The open-canopy fraction, derived from the ratio of the ground-point density and total pulse density of the lidar data, suggest that snow depth is deeper when the fraction is closer to 1. All these are strong evidence suggesting topographic and vegetation controls on the snow-depth distribution in the Sierra Nevada.

With segmented canopy structures, we deepened our understanding of canopy effects on snow-depth distributions. The snow-depth distribution can be affected by canopy structure and terrain interactively. The tree wells, which are the areas under canopy that have shallower snowpack, usually have more snow accumulated over the the down slope direction from the tree bole because of the snow creeping and longwave radiation heating effect. For similar reasons the gradients of tree wells are affected by the crown size, with gradients being steeper when the crown size is larger.

With these exploratory results, we constructed machine-learning models, more specifically, Random Forest and XGBoost regression models. The Random Forest regression approach can achieve a testing R^2 of 0.57 and the XGBoost regression model can achieve a testing R^2 of 0.71. XGBoost model shows great potential in modeling the snow-depth distribution at fine resolution in mountainous areas.

Temporally, the total snow accumulation is affected by canopy structures because of canopy interception. We extracted vegetation attributes from the lidar-derived canopy structures and sky-view factor (SVF) from the canonical-view camera images. The two types of attributes were found to be complementary to each other in terms of influencing snow accumulation under canopies. The magnitude of the effect depends on the total precipitation,

with the effect being more consistent and stronger when the precipitation is heavier. Also, the stronger influence does not come from the canopy right above the snow surface, but from the entire canopy cover within a certain radius (about 10 m).

The most important contribution of this dissertation is that we developed an approach using a k-nearest neighbors search and a Gaussian process regression for blending the real-time wireless-sensor networks snow measurements with historical spatial SWE maps as prior knowledge of spatial distribution of SWE. The approach is found to be accurate, supported by the validation results using SWE products derived from lidar collected from 2016. The R^2 is at least 0.82 if using 2014 lidar-derived SWE as training data. Although both SNODAS and historical SWE reconstructions can be used as training data, the spatial accuracy is much lower than that using lidar.

These findings help envision the future of a more integrated and intelligent snow-water information system for the Sierra Nevada and the state of California. The information system will be integrated with data from multiple platforms: ground measurements with wireless-sensor networks, satellite based remote-sensing imagery from MODIS and LandSat, as well as infrequent lidar scans. Each of the data sources has its unique value for estimating the spatial SWE in real time. Wireless-sensor networks provide real-time ground-truth measurements, remote-sensing imagery provides spatial snow coverage for modeling and data assimilation, and lidar data serve for algorithm evaluation and spatial data mining. And these data can be integrated using machine-learning and data-assimilation techniques. With further development the current water-information system should be resilient enough to respond to a changing climate.

Bibliography

Bair, E. H., Rittger, K., Davis, R. E., Painter, T. H., and Dozier, J. (2016). Validating reconstruction of snow water equivalent in California's Sierra Nevada using measurements from the NASA Airborne Snow Observatory. *Water Resources Research*, pages 1943–1959. (Cited on pages 3 and 62.)

Bales, R. C., Hopmans, J. W., O'Geen, A. T., Meadows, M., Hartsough, P. C., Kirchner, P., Hunsaker, C. T., and Beaudette, D. (2011). Soil Moisture Response to Snowmelt and Rainfall in a Sierra Nevada Mixed-Conifer Forest. *Vadose Zone Journal*, 10(3):786. (Cited on page 8.)

Bales, R. C., Molotch, N. P., Painter, T. H., Dettinger, M. D., Rice, R., and Dozier, J. (2006). Mountain hydrology of the western United States. *Water Resources Research*, 42(8). (Cited on pages 1, 26, 47, and 61.)

Baltsavias, E. (1999). Airborne laser scanning: basic relations and formulas. *ISPRS Journal of Photogrammetry & Remote Sensing*, (54):199–214. (Cited on page 21.)

Barrett, A. P. (2003). National Operational Hydrologic Remote Sensing Center SNOw Data Assimilation System (SNODAS) Products at NSIDC. *NSIDC Special Report 11*, (Natl. Snow and Ice Data Cent.: Boulder, CO):19. (Cited on pages 3, 6, 61, and 68.)

Bartelt, P. and Lehning, M. (2002). A physical snowpack model for the swiss avalanche warning: Part i: numerical model. *Cold Regions Science and Technology*, 35(3):123 – 145. (Cited on page 48.)

Breiman, L. (2001). Random forest. *Machine Learning*, 45(1):5–32. (Cited on page 14.)

Brun-Laguna, K., Oroza, C., Zhang, Z., Malek, S., Watteyne, T., and Glaser, S. (2016). Sierranet: Monitoring the snowpack in the sierra nevada: Demo. In *Proceedings of the Eleventh ACM Workshop on Challenged Networks*, CHANTS '16, pages 33–34, New York, NY, USA. ACM. (Cited on page 63.)

California Department of Water Resources (2013). California' s Flood Future: Recommendations for Managing the State's Flood Risk. Technical Report November. (Cited on page 61.)

Cayton, L. (2009). Efficient bregman range search. In Bengio, Y., Schuurmans, D., Lafferty, J. D., Williams, C. K. I., and Culotta, A., editors, *Advances in Neural Information Processing Systems 22*, pages 243–251. Curran Associates, Inc. (Cited on page 67.)

Chen, T. and Guestrin, C. (2016). XGBoost. In *Proceedings of the 22nd ACM SIGKDD International Conference on Knowledge Discovery and Data Mining - KDD '16*, pages 785–794, New York, New York, USA. ACM Press. (Cited on page 34.)

Cleveland, W. S. (1979). Robust Locally Weighted Regression and Smoothing Scatterplots. *Journal of the American Statistical Association*, 74(368):829–836. (Cited on page 14.)

Cline, D. W., Bales, R. C., and Dozier, J. (1998). Estimating the spatial distribution of snow in mountain basins using remote sensing and energy balance modeling. *Water Resources Research*, 34(5):1275. (Cited on pages 3 and 62.)

Clow, D. W., Nanus, L., Verdin, K. L., and Schmidt, J. (2012). Evaluation of SNODAS snow depth and snow water equivalent estimates for the Colorado Rocky Mountains, USA. *Hydrological Processes*, 26(17):2583–2591. (Cited on pages 6 and 68.)

Courbaud, B., De Coligny, F., and Cordonnier, T. (2003). Simulating radiation distribution in a heterogeneous Norway spruce forest on a slope. *Agricultural and Forest Meteorology*, 116(1-2):1–18. (Cited on page 24.)

Deems, J. S., Fassnacht, S. R., and Elder, K. J. (2006). Fractal Distribution of Snow Depth from Lidar Data. *Journal of Hydrometeorology*, 7(2):285–297. (Cited on page 7.)

Deems, J. S., Painter, T. H., and Finnegan, D. C. (2013). Lidar measurement of snow depth: a review. *Journal of Glaciology*, 59(215):467–479. (Cited on pages 7, 21, and 40.)

Dozier, J., Bair, E. H., and Davis, R. E. (2016). Estimating the spatial distribution of snow water equivalent in the world's mountains. *Wiley Interdisciplinary Reviews: Water*, 3(3):461–474. (Cited on page 83.)

Dozier, J., Painter, T. H., Rittger, K., and Frew, J. E. (2008). Time-space continuity of daily maps of fractional snow cover and albedo from MODIS. *Advances in Water Resources*, 31(11):1515–1526. (Cited on page 61.)

Dubayah, R. C. (1994). Modeling a solar radiation topoclimatology for the Rio Grande River Basin. *Journal of Vegetation Science*, 5(5):627–640. (Cited on page 24.)

Erickson, T. a., Williams, M. W., and Winstral, A. (2005). Persistence of topographic controls on the spatial distribution of snow in rugged mountain terrain, Colorado, United States. *Water Resources Research*, 41(4):1–17. (Cited on page 7.)

Erxleben, J., Elder, K., and Davis, R. (2002). Comparison of spatial interpolation methods for estimating snow distribution in the Colorado Rocky Mountains. *Hydrological Processes*, 16(18):3627–3649. (Cited on page 7.)

ESRI (2015). ArcGIS Desktop. (Cited on page 29.)

Essery, R., Bunting, P., Rowlands, A., Rutter, N., Hardy, J., Melloh, R., Link, T., Marks, D., and Pomeroy, J. (2008a). Radiative Transfer Modeling of a Coniferous Canopy Characterized by Airborne Remote Sensing. *Journal of Hydrometeorology*, 9(2):228–241. (Cited on pages 23 and 24.)

Essery, R. and Etchevers, P. (2004). Parameter sensitivity in simulations of snowmelt. *Journal of Geophysical Research: Atmospheres*, 109(D20). (Cited on page 1.)

Essery, R., Pomeroy, J., Ellis, C., and Link, T. (2008b). Modelling longwave radiation to snow beneath forest canopies using hemispherical photography or linear regression. *Hydrological Processes*, 22(15):2788–2800. (Cited on page 43.)

Fassnacht, S. R., Dressler, K. A., and Bales, R. C. (2003). Snow water equivalent interpolation for the Colorado River Basin from snow telemetry (SNOTEL) data. *Water Resources Research*, 39(8). (Cited on pages 4, 62, and 82.)

Felzenszwalb, P. F. and Huttenlocher, D. P. (2004). Efficient Graph-Based Image Segmentation. *International Journal of Computer Vision*, 59(2):167–181. (Cited on page 31.)

Filgueira, A., Gonzlez-Jorge, H., Lagela, S., Daz-Vilario, L., and Arias, P. (2017). Quantifying the influence of rain in lidar performance. *Measurement*, 95:143 – 148. (Cited on page 48.)

Fowler, H. J. and Wilby, R. L. (2007). Beyond the downscaling comparison study. *International Journal of Climatology*, 27(12):1543–1545. (Cited on page 81.)

Gangopadhyay, S. and Clark, M. (2005). Statistical downscaling using K-nearest neighbors. *Water Resources Research*, 41(W02024). (Cited on pages 62 and 81.)

Garvelmann, J., Pohl, S., and Weiler, M. (2014). Variability of Observed Energy Fluxes during Rain-on-Snow and Clear Sky Snowmelt in a Midlatitude Mountain Environment. *Journal of Hydrometeorology*, 15(3):1220–1237. (Cited on page 81.)

Gelfan, a. N., Pomeroy, J. W., and Kuchment, L. S. (2004). Modeling Forest Cover Influences on Snow Accumulation, Sublimation, and Melt. *Journal of Hydrometeorology*, 5(5):785–803. (Cited on page 23.)

Golding, D. L. and Swanson, R. H. (1986). Snow distribution patterns in clearings and adjacent forest. *Water Resources Research*, 22(13):1931–1940. (Cited on pages 26 and 47.)

Goulden, M. L., Anderson, R. G., Bales, R. C., Kelly, A. E., Meadows, M., and Winston, G. C. (2012). Evapotranspiration along an elevation gradient in California's Sierra Nevada. *Journal of Geophysical Research: Biogeosciences*, 117(G3):n/a–n/a. (Cited on pages 8, 28, and 46.)

Gowda, P., Oommen, T., Misra, D., Schwartz, R., Howell, T., and Wagle, P. (2015). Retrieving Leaf Area Index from Remotely Sensed Data Using Advanced Statistical Approaches. *Journal of Remote Sensing & GIS*, 05(01). (Cited on page 27.)

Gower, S. T. and Norman, J. M. (1991). Rapid estimation of leaf area index in conifer and broadleaf plantations. *Ecology*, 72(5):1896–1900. (Cited on page 48.)

Guan, B., Molotch, N. P., Waliser, D. E., Jepsen, S. M., Painter, T. H., and Dozier, J. (2013). Snow water equivalent in the Sierra Nevada: Blending snow sensor observations with snowmelt model simulations. *Water Resources Research*, 49(8):5029–5046. (Cited on pages 3, 4, 6, 62, 64, and 81.)

Guo, Q., Li, W., Yu, H., and Alvarez, O. (2010). Effects of Topographic Variability and Lidar Sampling Density on Several DEM Interpolation Methods. *Photogrammetric Engineering & Remote Sensing*, 76(6):701–712. (Cited on page 43.)

He, Z. H., Parajka, J., Tian, F. Q., and Blöschl, G. (2014). Estimating degree-day factors from modis for snowmelt runoff modeling. *Hydrology and Earth System Sciences*, 18(12):4773–4789. (Cited on page 3.)

Hedrick, A., Marshall, H.-P., Winstral, A., Elder, K., Yueh, S., and Cline, D. (2015). Independent evaluation of the SNODAS snow depth product using regional-scale lidar-derived measurements. *The Cryosphere*, 9(1):13–23. (Cited on page 69.)

Hedstrom, N. R. and Pomeroy, J. W. (1998). Measurements and modelling of snow interception in the boreal forest. *Hydrological Processes*, 12(10-11):1611–1625. (Cited on pages 24, 47, and 48.)

Hellstrm, R. A. (2001). Forest cover algorithms for estimating meteorological forcing in a numerical snow model. *Hydrological Processes*, 14(18):3239–3256. (Cited on page 48.)

Hodgson, M. E. and Bresnahan, P. (2004). Accuracy of Airborne Lidar-Derived Elevation : Empirical Assessment and Error Budget. *Photogrammetric engineering and remote sensing*, 70(3):331–339. (Cited on page 21.)

Hopkinson, C., Sitar, M., Chasmer, L., Gynan, C., Agro, D., Enter, R., Foster, J., Heels, N., Hoffman, C., Nillson, J., and Others (2001). Mapping the spatial distribution of snowpack depth beneath a variable forest canopy using airborne laser altimetry. *Proceedings of the 58th Annual Eastern Snow Conference*. (Cited on pages 1, 2, 7, 26, 27, and 47.)

Hostetler, S. W. (1994). Hydrologic and atmospheric models: The (continuing) problem of discordant scales. *Climatic Change*, 27(4):345–350. (Cited on page 81.)

Houze, R. A. (2012). Orographic effects on precipitating clouds. *Reviews of Geophysics*, 50(1). (Cited on pages 26, 31, and 47.)

Howard, R. and Stull, R. (2013). IR Radiation from Trees to a Ski Run: A Case Study. *Journal of Applied Meteorology and Climatology*, 52(7):1525–1539. (Cited on page 43.)

Howat, I. M. and Tulaczyk, S. (2005). Climate sensitivity of spring snowpack in the Sierra Nevada. *Journal of Geophysical Research: Earth Surface*, 110(F4):n/a–n/a. (Cited on pages 7 and 83.)

Hunsaker, C. T., Whitaker, T. W., and Bales, R. C. (2012). Snowmelt Runoff and Water Yield Along Elevation and Temperature Gradients in California's Southern Sierra Nevada1. *JAWRA Journal of the American Water Resources Association*, 48(4):667–678. (Cited on pages 8 and 9.)

Isenburg, M. (2014). LAStools - efficient LiDAR processing software. (Cited on page 28.)

Julander, R. P., Wilson, G. R., and Nault, R. (1998). The Franklin Basin Problem. In *66th Annual Western Snow Conference*. Western Snow Conference. (Cited on page 6.)

Kalra, A. and Ahmad, S. (2011). Evaluating changes and estimating seasonal precipitation for the Colorado River Basin using a stochastic nonparametric disaggregation technique. *Water Resources Research*, 47(W05555). (Cited on page 62.)

Kelly, M. and Di Tommaso, S. (2015). Mapping forests with Lidar provides flexible, accurate data with many uses. *California Agriculture*, 69(1):14–20. (Cited on page 27.)

Kirchner, P. B. (2013). *Electronic Theses and Dissertations UC Merced SNOW HYDROLOGY OF THE SOUTHERN SIERRA NEVADA , CALIFORNIA A dissertation submitted in partial fulfillment of the requirements for the degree of Doctor of Philosophy by Peter Bernard Kirchner in Environmental S.* PhD thesis, University of California, Merced. (Cited on page 15.)

Kirchner, P. B., Bales, R. C., Molotch, N. P., Flanagan, J., and Guo, Q. (2014). LiDAR measurement of seasonal snow accumulation along an elevation gradient in the southern Sierra Nevada, California. *Hydrology and Earth System Sciences Discussions*, 11:5327–5365. (Cited on pages 1, 7, 8, 9, 10, 11, 12, 14, 17, 21, and 28.)

Larose, D. T. (2005). k-Nearest Neighbor Algorithm. In *Discovering Knowledge in Data*, pages 90–106. John Wiley & Sons, Inc., Hoboken, NJ, USA. (Cited on page 62.)

Lehning, M., Vlksch, I., Gustafsson, D., Nguyen, T. A., Sthli, M., and Zappa, M. (2006). Alpine3d: a detailed model of mountain surface processes and its application to snow hydrology. *Hydrological Processes*, 20(10):2111–2128. (Cited on page 48.)

Li, W., Guo, Q., Jakubowski, M. K., and Kelly, M. (2012). A New Method for Segmenting Individual Trees from the Lidar Point Cloud. *Photogrammetric Engineering & Remote Sensing*, 78(1):75–84. (Cited on page 27.)

Li, X.-J., Ma, X.-J., and Zhang, J.-X. (2016). Robust feature screening for varying coefficient models via quantile partial correlation. *Metrika*, pages 1–33. (Cited on page 66.)

Liu, J., Li, R., and Wu, R. (2014). Feature Selection for Varying Coefficient Models With Ultrahigh-Dimensional Covariates. *Journal of the American Statistical Association*, 109(505):266–274. (Cited on page 66.)

Liu, J., Woodcock, C. E., Melloh, R. A., Davis, R. E., McKenzie, C., and Painter, T. H. (2008). Modeling the view angle dependence of gap fractions in forest canopies: Implications for mapping fractional snow cover using optical remote sensing. *Journal of Hydrometeorology*, 9(5):1005–1019. (Cited on page 81.)

Livneh, B., Rosenberg, E. A., Lin, C., Nijssen, B., Mishra, V., Andreadis, K. M., Maurer, E. P., and Lettenmaier, D. P. (2013). A Long-Term Hydrologically Based Dataset of Land Surface Fluxes and States for the Conterminous United States: Update and Extensions*. *Journal of Climate*, 26(23):9384–9392. (Cited on page 83.)

López-Moreno, J. I. and Latron, J. (2008). Influence of canopy density on snow distribution in a temperate mountain range. *Hydrological Processes*, 22(1):117–126. (Cited on page 27.)

Lu, H., Wei, W.-s., Liu, M.-z., Han, X., and Hong, W. (2014). Observations and modeling of incoming longwave radiation to snow beneath forest canopies in the west Tianshan Mountains, China. *Journal of Mountain Science*, 11(5):1138–1153. (Cited on pages 43 and 44.)

Lundquist, J. D., Neiman, P. J., Martner, B., White, A. B., Gottas, D. J., and Ralph, F. M. (2008). Rain versus Snow in the Sierra Nevada, California: Comparing Doppler Profiling Radar and Surface Observations of Melting Level. *Journal of Hydrometeorology*, 9(2):194–211. (Cited on page 81.)

Mahat, V. and Tarboton, D. G. (2013). Representation of canopy snow interception, unloading and melt in a parsimonious snowmelt model. *Hydrological Processes*, 6336(December 2013):n/a–n/a. (Cited on page 1.)

Malek, S. A., Avanzi, F., Brun-Laguna, K., Maurer, T., Oroza, C. A., Hartsough, P. C., Watteyne, T., and Glaser, S. D. (2017). Real-time alpine measurement system using wireless sensor networks. *Sensors*, 17(2583). (Cited on page 3.)

Margulis, S. A., Cortés, G., Girotto, M., and Durand, M. (2016). A Landsat-Era Sierra Nevada Snow Reanalysis (19852015). *Journal of Hydrometeorology*, 17(4):1203–1221. (Cited on pages 3, 62, and 83.)

Marks, D., Domingo, J., Susong, D., Link, T., and Garen, D. (1999). A spatially distributed energy balance snowmelt model for application in mountain basins. *Hydrological Processes*, 13(12-13):1935–1959. (Cited on pages 3, 26, 48, and 68.)

Marks, D., Dozier, J., and Davis, R. E. (1992). Climate and energy exchange at the snow surface in the alpine region of the sierra nevada: 2. snow cover energy balance. *Water Resources Research*, 28(11):3043–3054. (Cited on page 3.)

Marks, D., Kimball, J., Tingey, D., and Link, T. (1998). The sensitivity of snowmelt processes to climate conditions and forest cover during rain-on-snow: a case study of the 1996 Pacific Northwest flood. *Hydrological Processes*, 12(10-11):1569–1587. (Cited on pages 26 and 27.)

Marks, K. and Bates, P. (2000). Integration of high-resolution topographic data with floodplain flow models. *Hydrological Processes*, 14(July 1998):2109–2122. (Cited on pages 2 and 7.)

Molotch, N. P. and Bales, R. C. (2005). Scaling snow observations from the point to the grid element: Implications for observation network design. *Water Resources Research*, 41(11):1–16. (Cited on pages 2, 3, 27, 61, and 82.)

Molotch, N. P., Colee, M. T., Bales, R. C., and Dozier, J. (2005). Estimating the spatial distribution of snow water equivalent in an alpine basin using binary regression tree models: The impact of digital elevation data and independent variable selection. *Hydrological Processes*, 19(December 2004):1459–1479. (Cited on pages 7 and 27.)

Molotch, N. P., Guan, B., and Lestak, L. R. (2017). Snow Water Equivalent (SWE) for Water Supply and Management in California. INSTAAR and NASA's Jet Propulsion Laboratory, University of Colorado at Boulder, Colorado, USA. Digital media available by request. (Cited on page 64.)

Molotch, N. P. and Margulis, S. a. (2008). Estimating the distribution of snow water equivalent using remotely sensed snow cover data and a spatially distributed snowmelt model: A multi-resolution, multi-sensor comparison. *Advances in Water Resources*, 31(11):1503–1514. (Cited on pages 6 and 61.)

Mott, R., Scipin, D., Schneebeli, M., Dawes, N., Berne, A., and Lehning, M. (2014). Orographic effects on snow deposition patterns in mountainous terrain. *Journal of Geophysical Research: Atmospheres*, 119(3):1419–1439. (Cited on pages 26, 31, and 47.)

Musselman, K. N., Margulis, S. a., and Molotch, N. P. (2013). Estimation of solar direct beam transmittance of conifer canopies from airborne LiDAR. *Remote Sensing of Environment*, 136:402–415. (Cited on page 13.)

Musselman, K. N., Molotch, N. P., and Brooks, P. D. (2008). Effects of vegetation on snow accumulation and ablation in a mid-latitude sub-alpine forest. *Hydrological Processes*, 22(15):2767–2776. (Cited on pages 1, 24, 26, 27, and 48.)

Musselman, K. N., Molotch, N. P., Margulis, S. A., Kirchner, P. B., and Bales, R. C. (2012). Influence of canopy structure and direct beam solar irradiance on snowmelt rates in a

mixed conifer forest. *Agricultural and Forest Meteorology*, 161:46–56. (Cited on pages 24, 26, 27, and 48.)

Ni, K. and Nguyen, T. (2009). An Adaptable k-Nearest Neighbors Algorithm for MMSE Image Interpolation. *IEEE Transactions on Image Processing*, 18(9):1976–1987. (Cited on page 62.)

Nolan, M., Larsen, C., and Sturm, M. (2015). Mapping snow-depth from manned-aircraft on landscape scales at centimeter resolution using Structure-from-Motion photogrammetry. *The Cryosphere Discussions*, 9:333–381. (Cited on page 11.)

Ohmura, A. (2001). Physical Basis for the Temperature-Based Melt-Index Method. *Journal of Applied Meteorology*, 40(4):753–761. (Cited on pages 3 and 33.)

Oroza, C. A., Zheng, Z., Glaser, S. D., Tuia, D., and Bales, R. C. (2016). Optimizing embedded sensor network design for catchment-scale snow-depth estimation using LiDAR and machine learning. *Water Resources Research*, 52(10):8174–8189. (Cited on pages 3 and 69.)

Painter, T. H., Berisford, D. F., Boardman, J. W., Bormann, K. J., Deems, J. S., Gehrke, F., Hedrick, A., Joyce, M., Laidlaw, R., Marks, D., Mattmann, C., McGurk, B., Ramirez, P., Richardson, M., Skiles, S. M. K., Seidel, F. C., and Winstral, A. (2016). The Airborne Snow Observatory: Fusion of scanning lidar, imaging spectrometer, and physically-based modeling for mapping snow water equivalent and snow albedo. *Remote Sensing of Environment*, 184:139–152. (Cited on pages 2, 66, and 68.)

Painter, T. H., Rittger, K., McKenzie, C., Slaughter, P., Davis, R. E., and Dozier, J. (2009). Retrieval of subpixel snow covered area, grain size, and albedo from MODIS. *Remote Sensing of Environment*, 113(4):868–879. (Cited on pages 2, 61, and 81.)

Pedregosa, F., Varoquaux, G., Gramfort, A., Michel, V., Thirion, B., Grisel, O., Blondel, M., Louppe, G., Prettenhofer, P., Weiss, R., Dubourg, V., Vanderplas, J., Passos, A., Cournapeau, D., Brucher, M., Perrot, M., and Duchesnay, É. (2011). Scikit-learn: Machine Learning in Python. *Journal of Machine Learning Research*, 12:2825–2830. (Cited on pages 14 and 33.)

Pomeroy, J. W., Gray, D. M., Hedstrom, N. R., and Janowicz, J. R. (2002). Prediction of seasonal snow accumulation in cold climate forests. *Hydrological Processes*, 16(18):3543–3558. (Cited on pages 24 and 48.)

Pomeroy, J. W., Parviainen, J., Hedstrom, N., and Gray, D. M. (1998). Coupled modelling of forest snow interception and sublimation. *Hydrological Processes*, 12(15):2317–2337. (Cited on page 23.)

Prairie, J., Rajagopalan, B., Lall, U., and Fulp, T. (2007). A stochastic nonparametric technique for space-time disaggregation of streamflows. *Water Resources Research*, 43(W03432). (Cited on pages 62 and 81.)

Rajagopalan, B. and Lall, U. (1999). A k -nearest-neighbor simulator for daily precipitation and other weather variables. *Water Resources Research*, 35(10):3089–3101. (Cited on page 62.)

Raleigh, M. S., Rittger, K., Moore, C. E., Henn, B., Lutz, J. a., and Lundquist, J. D. (2013). Ground-based testing of MODIS fractional snow cover in subalpine meadows and forests of the Sierra Nevada. *Remote Sensing of Environment*, 128:44–57. (Cited on pages 61 and 81.)

Revuelto, J., López-Moreno, J. I., Azorin-Molina, C., and Vicente-Serrano, S. M. (2015). Canopy influence on snow depth distribution in a pine stand determined from terrestrial laser data. *Water Resources Research*, 51(5):3476–3489. (Cited on pages 27 and 48.)

Rice, R. and Bales, R. C. (2010). Embedded-sensor network design for snow cover measurements around snow pillow and snow course sites in the Sierra Nevada of California. *Water Resources Research*, 46(3):1–13. (Cited on page 6.)

Rice, R., Bales, R. C., Painter, T. H., and Dozier, J. (2011). Snow water equivalent along elevation gradients in the merced and tuolumne river basins of the sierra nevada. *Water Resources Research*, 47(8). W08515. (Cited on pages 7 and 81.)

Rittger, K. (2012). *Spatial estimates of snow water equivalent in the Sierra Nevada*. PhD thesis, University of California, Santa Barbara. (Cited on pages 3 and 62.)

Rittger, K., Bair, E. H., Kahl, A., and Dozier, J. (2016). Spatial estimates of snow water equivalent from reconstruction. *Advances in Water Resources*, 94:345–363. (Cited on page 83.)

Rittger, K., Painter, T. H., and Dozier, J. (2013). Assessment of methods for mapping snow cover from MODIS. *Advances in Water Resources*, 51:367–380. (Cited on page 61.)

Roe, G. H. (2005). Orographic Precipitation. *Annual Review of Earth and Planetary Sciences*, 33(1):645–671. (Cited on page 1.)

Roerdink, J. B. and Meijster, A. (2000). The watershed transform: Definitions, algorithms and parallelization strategies. *Fundam. Inf.*, 41(1,2):187–228. (Cited on page 30.)

Rosenberg, E. a., Wood, A. W., and Steinemann, A. C. (2011). Statistical applications of physically based hydrologic models to seasonal streamflow forecasts. *Water Resources Research*, 47(3):n/a–n/a. (Cited on pages 2 and 6.)

Rosenthal, W. and Dozier, J. (1996). Automated mapping of montane snow cover at subpixel resolution from the Landsat Thematic Mapper. *Water Resources Research*, 32(1):115–130. (Cited on pages 2 and 61.)

Roth, T. R. and Nolin, A. W. (2017). Forest impacts on snow accumulation and ablation across an elevation gradient in a temperate montane environment. *Hydrology and Earth System Sciences*, 21(11):5427–5442. (Cited on page 43.)

Safeeq, M. and Hunsaker, C. T. (2016). Characterizing Runoff and Water Yield for Headwater Catchments in the Southern Sierra Nevada. *JAWRA Journal of the American Water Resources Association*, 52(6):1327–1346. (Cited on page 44.)

Schmidt, R. a. and Gluns, D. R. (1991a). Snowfall interception on branches of three conifer species. *Canadian Journal of Forest Research*. (Cited on pages 23 and 24.)

Schmidt, R. A. and Gluns, D. R. (1991b). Snowfall interception on branches of three conifer species. *Canadian Journal of Forest Research*, 21(8):1262–1269. (Cited on pages 48 and 58.)

Schneider, D. and Molotch, N. P. (2016). Real-time estimation of snow water equivalent in the Upper Colorado River Basin using MODIS-based SWE Reconstructions and SNOTEL data. *Water Resources Research*, 52(10):7892–7910. (Cited on pages 4, 62, and 69.)

Seyednasrollah, B. and Kumar, M. (2014). Net radiation in a snow-covered discontinuous forest gap for a range of gap sizes and topographic configurations. *Journal of Geophysical Research*, 119(17):10,323–10,342. (Cited on page 43.)

Sicart, J. E., Essery, R. L. H., Pomeroy, J. W., Hardy, J., Link, T., and Marks, D. (2004). A Sensitivity Study of Daytime Net Radiation during Snowmelt to Forest Canopy and Atmospheric Conditions. *Journal of Hydrometeorology*, 5(5):774–784. (Cited on page 26.)

Sirpa, R., David, G., Harri, K., Ari, L., Achim, G., OlliKalle, K., Ola, L., Anders, L., Kai, R., Magnus, S., and Per, W. (2012). Estimation of winter leaf area index and sky view fraction for snow modelling in boreal coniferous forests: consequences on snow mass and energy balance. *Hydrological Processes*, 27(20):2876–2891. (Cited on page 48.)

Slater, A. G., Barrett, A. P., Clark, M. P., Lundquist, J. D., and Raleigh, M. S. (2013). Uncertainty in seasonal snow reconstruction: Relative impacts of model forcing and image availability. *Advances in Water Resources*, 55:165–177. (Cited on page 70.)

Stenberg, P., Linder, S., Smolander, H., and Flower-Ellis, J. (1994). Performance of the lai-2000 plant canopy analyzer in estimating leaf area index of some scots pine stands. *Tree Physiology*, 14(7-8-9):981–995. (Cited on page 48.)

Storck, P., Lettenmaier, D. P., and Bolton, S. M. (2002). Measurement of snow interception and canopy effects on snow accumulation and melt in a mountainous maritime climate, oregon, united states. *Water Resources Research*, 38(11):5–1–5–16. (Cited on pages 47 and 48.)

Strîmbu, V. F. and Strîmbu, B. M. (2015). A graph-based segmentation algorithm for tree crown extraction using airborne LiDAR data. *ISPRS Journal of Photogrammetry and Remote Sensing*, 104:30–43. (Cited on page 27.)

Sturm, M., Holmgren, J., McFadden, J. P., Liston, G. E., III, F. S. C., and Racine, C. H. (2001). Snowshrub interactions in arctic tundra: A hypothesis with climatic implications. *Journal of Climate*, 14(3):336–344. (Cited on page 48.)

Sumida, A., Miyaura, T., and Torii, H. (2013). Relationships of tree height and diameter at breast height revisited: analyses of stem growth using 20-year data of an even-aged Chamaecyparis obtusa stand. *Tree Physiology*, 33(1):106–118. (Cited on page 44.)

Teti, P. (2003). Relations between peak snow accumulation and canopy density. *Forestry Chronicle*, 79(2):307–312. (Cited on page 23.)

van der Walt, S., Schönberger, J. L., Nunez-Iglesias, J., Boulogne, F., Warner, J. D., Yager, N., Gouillart, E., and Yu, T. (2014). scikit-image: image processing in Python. *PeerJ*, 2:e453. (Cited on page 31.)

van Heeswijk, M., Kimball, J. S., and Marks, D. (1996). Simulation of Water Available for Runoff in Clearcut Forest Openings During Rain-On-Snow Events in the Western Cascade Range of Oregon and Washington. Technical report, U.S. Geological Survey. (Cited on page 27.)

Varhola, A., Coops, N. C., Weiler, M., and Moore, R. D. (2010). Forest canopy effects on snow accumulation and ablation: An integrative review of empirical results. *Journal of Hydrology*, 392(3-4):219–233. (Cited on page 27.)

Webster, C., Rutter, N., and Jonas, T. (2017). Improving representation of canopy temperatures for modeling subcanopy incoming longwave radiation to the snow surface. *Journal of Geophysical Research: Atmospheres*, 122(17):9154–9172. (Cited on page 43.)

Willmott, C. J. (1982). Some Comments on the Evaluation of Model Performance. *Bulletin of the American Meteorological Society*, 63(11):1309–1313. (Cited on page 72.)

Winstral, A., Elder, K., and Davis, R. E. (2002). Spatial snow modeling of wind-redistributed snow using terrain-based parameters. *Journal of Hydrometeorology*, 3(5):524–538. (Cited on page 31.)

Winstral, A. and Marks, D. (2013). Longterm snow distribution observations in a mountain catchment: Assessing variability, time stability, and the representativeness of an index site. *Water Resources Research*, 50(1):293–305. (Cited on pages 26 and 47.)

Zhang, Z., Glaser, S., Bales, R., Conklin, M., Rice, R., and Marks, D. (2017a). Insights into mountain precipitation and snowpack from a basinscale wirelesssensor network. *Water Resources Research*, 53(8):6626–6641. (Cited on page 3.)

Zhang, Z., Glaser, S. D., Bales, R. C., Conklin, M., Rice, R., and Marks, D. G. (2017b). Technical report: The design and evaluation of a basin-scale wireless sensor network for mountain hydrology. *Water Resources Research*, 53(5):4487–4498. (Cited on pages vi, 3, 62, 63, 64, and 66.)

Zheng, G. and Moskal, L. M. (2009). Retrieving Leaf Area Index (LAI) Using Remote Sensing: Theories, Methods and Sensors. *Sensors*, 9(4):2719–2745. (Cited on pages 27 and 48.)

Zheng, Z., Kirchner, P. B., and Bales, R. C. (2016). Topographic and vegetation effects on snow accumulation in the southern Sierra Nevada: a statistical summary from lidar data. *The Cryosphere*, 10(1):257–269. (Cited on pages 4, 27, 28, 40, 48, 62, and 69.)

Zheng, Z., Molotch, N. P., Oroza, C. A., Conklin, M. H., and Bales, R. C. (2018). Spatial snow water equivalent estimation for mountainous areas using wireless-sensor networks and remote-sensing products. *Remote Sensing of Environment*, 215:44 – 56. (Cited on pages 5 and 47.)

Zhu, X., Vondrick, C., Fowlkes, C. C., and Ramanan, D. (2016). Do We Need More Training Data? *International Journal of Computer Vision*, 119(1):76–92. (Cited on page 75.)

Appendix A

Supplementary Figures

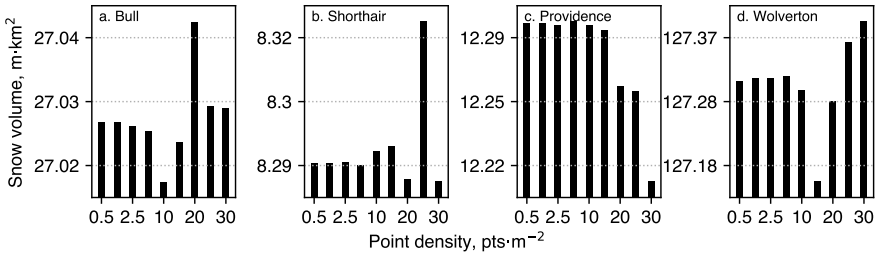

Figure A.1: Changes of lidar-derived total snow volume with the DEM resolution at (a) SSCZO Bull site, (b) Shorthair site, (c) Providence site and (d) Wolverton site.

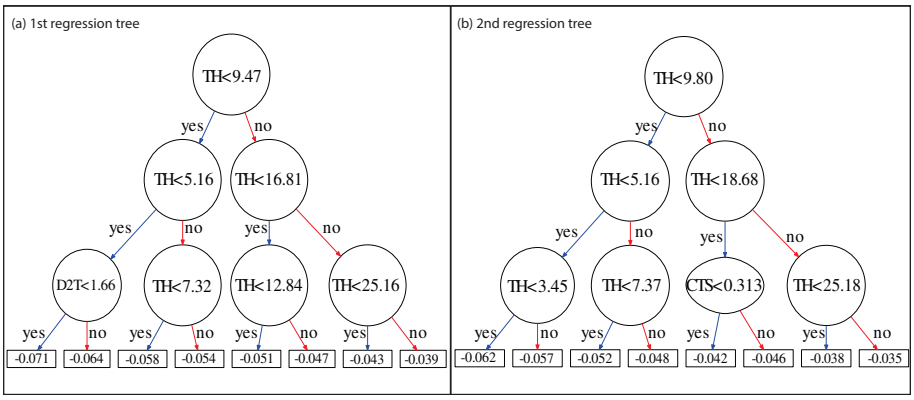

Figure A.2: Comparison between (a) the 1st regression tree and (b) the second regression tree trained in the XGBoost model. The canopy height is dominant comparing to the distance to the tree bole and canopy-terrain shadow.

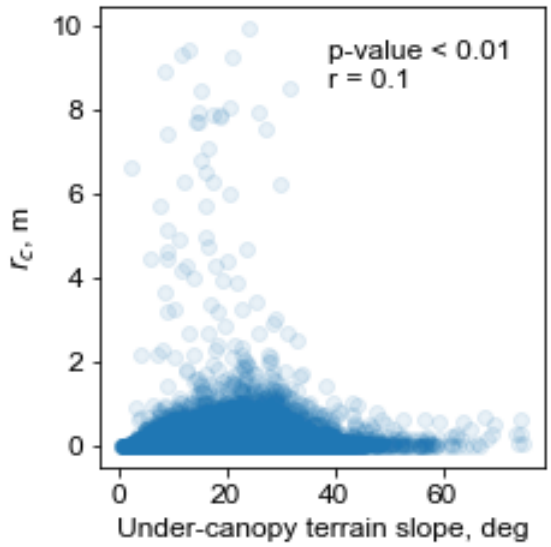

Figure A.3: Correlation analysis between the distance from the tree bole to the center of mass of tree well r_c and the local slope under the canopy.

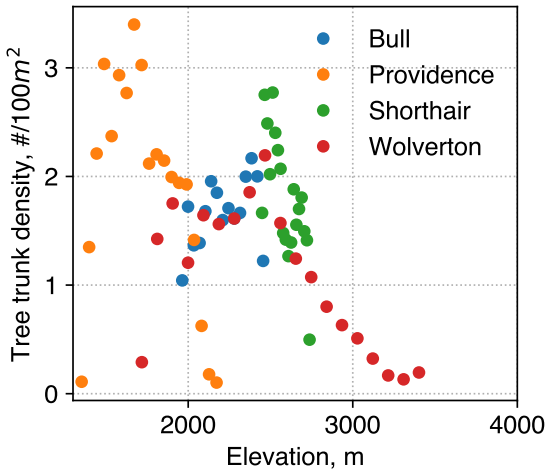

Figure A.4: Segmented canopy density by elevation at four study areas

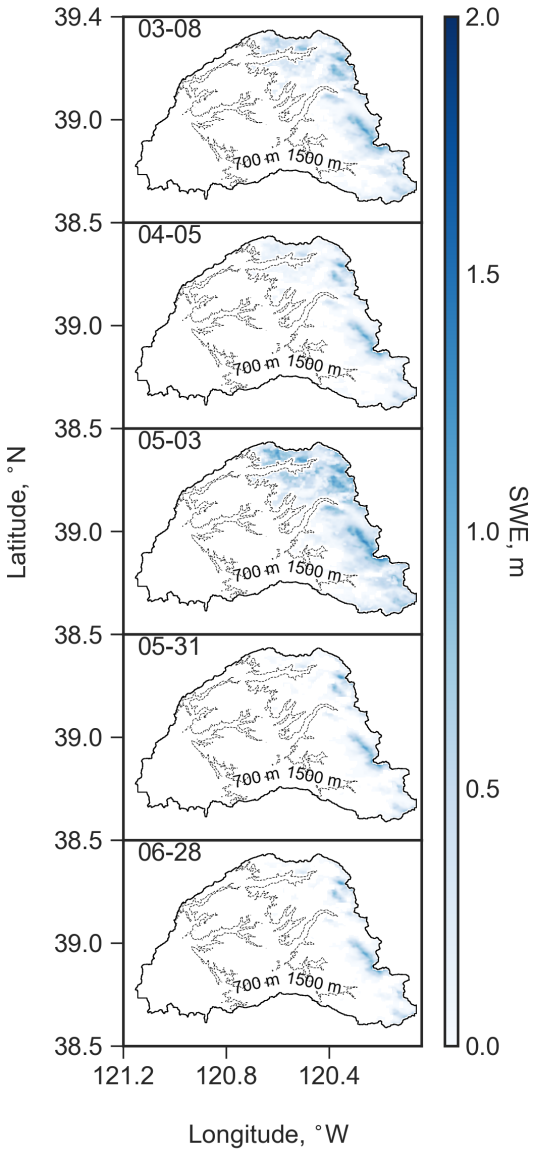

Figure A.5: Bi-weekly snow water equivalent maps in the American River basin created using ground measurements and historical reconstruction data through k-NN algorithm.

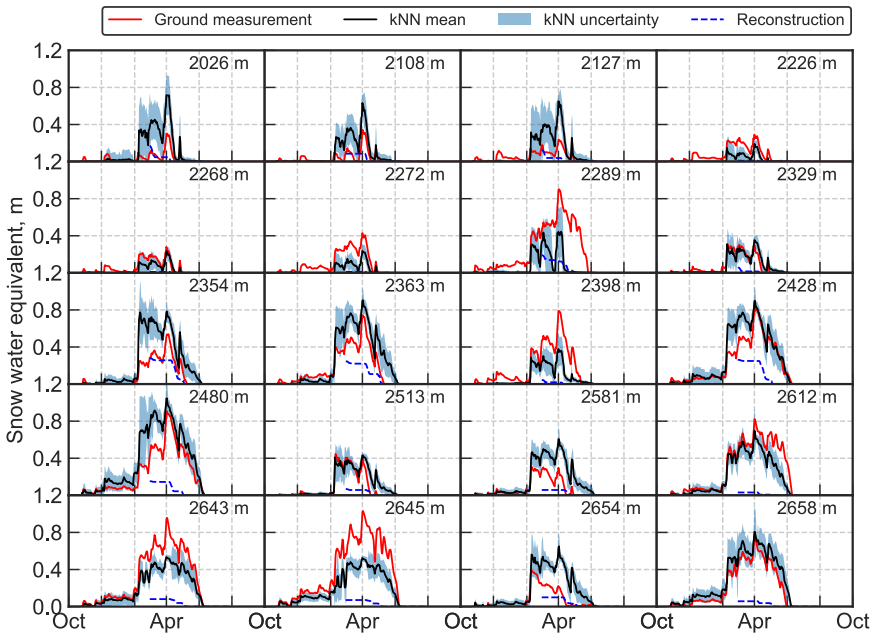

Figure A.6: Daily snow water equivalent time-series from the ground measurements, k-NN estimations, and reconstructions at 20 pixels, sorted by elevation, in the American River basin.

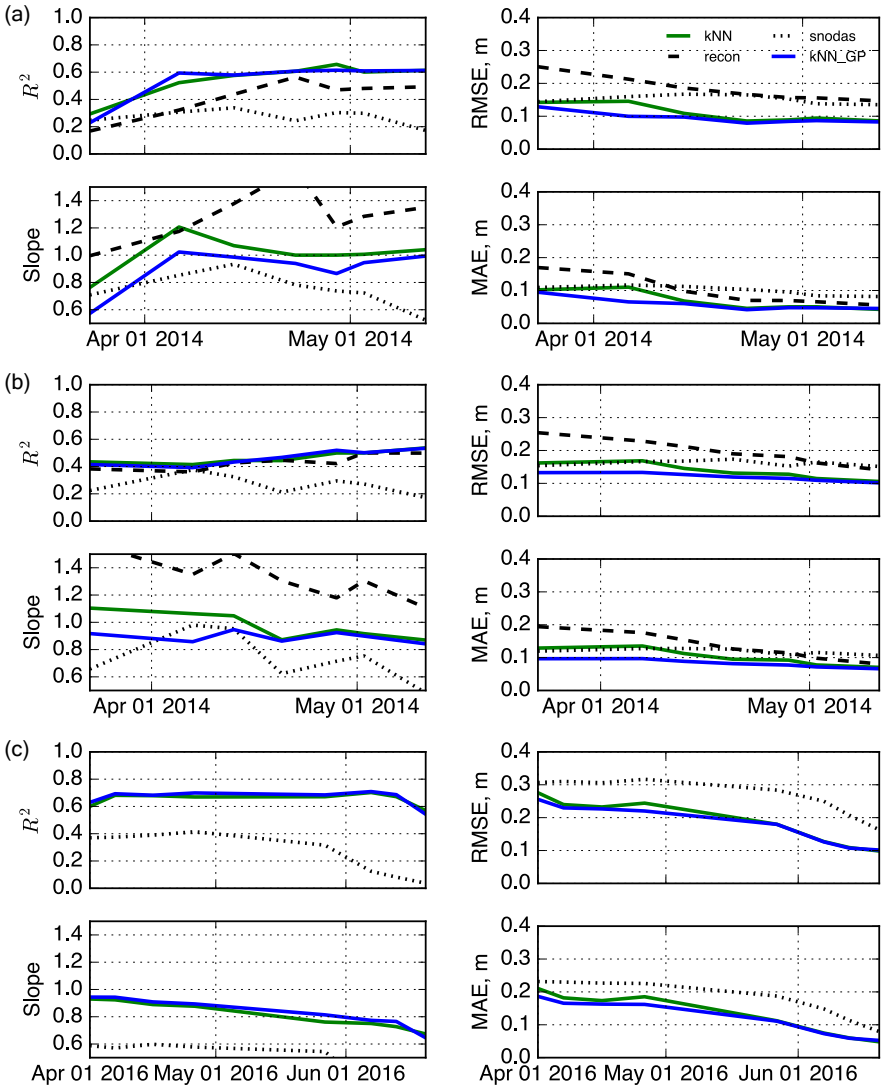

Figure A.7: Slopes and coefficients of determination estimated from linear regressions between SWE estimations vs. lidar, RMSE and MAE of SWE estimations and lidar at (a) Merced basin 2014 (b) Tuolumne basin in 2014 and (c) Tuolumne basin in 2016.

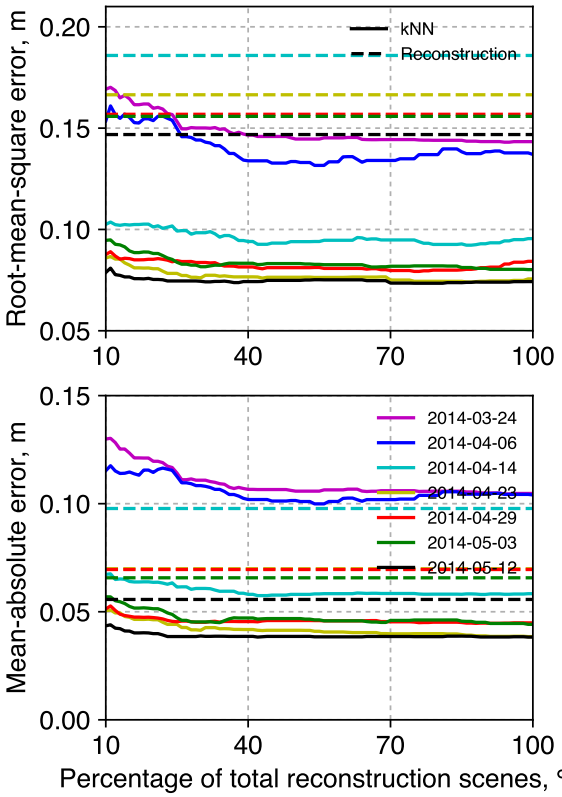

Figure A.8: Solid lines are (a) root-mean-square error and (b) mean-absolute error versus the percentage of total number of SWE reconstruction scenes that were included in the k-NN method. The errors are estimated from the results of the analysis for the 2014 Merced basin data. The dashed lines are the errors of SWE reconstructions at the same dates, which are used as baselines of prediction performance.

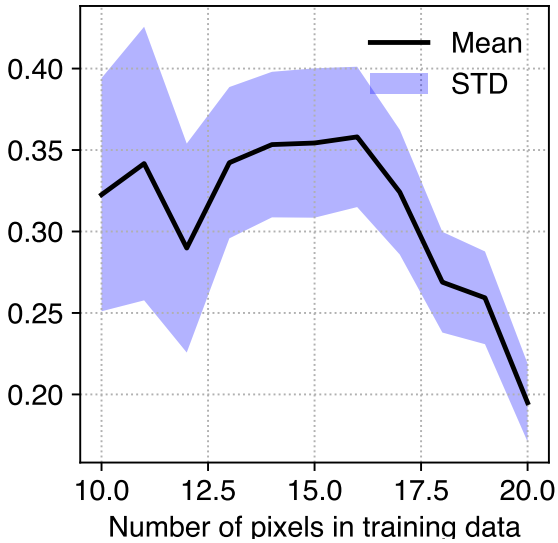

Figure A.9: Root-mean-square error versus number of sensors included in the training data of the k-NN algorithm.